Mechanical Modeling of Short Fiber Reinforced Composites Using the Extended Finite Element Method

By

Matthew G. Pike

Dissertation

Submitted to the Faculty of the

Graduate School of Vanderbilt University

in partial fulfillment of the requirements

for the degree of

DOCTOR OF PHILOSOPHY

in

Civil Engineering

December, 2015

Nashville, Tennessee

Approved:

Caglar Oskay, Ph.D.

Prodyot K. Basu, Ph.D.

Ravindra Duddu, Ph.D.

Michael Myers, Ph.D.

Florence Sanchez, Ph.D.

To my supportive family and friends

ACKNOWLEDGMENTS

I would like to express my deepest appreciation to my research advisor, Dr. Caglar Oskay, who inspired and motivated me with his wisdom, knowledge and commitment to the highest standards. Without his excellent guidance and support, this dissertation would not have been possible.

I would like to express my gratitude to Dr. Michael Myers, who has been a wonderful boss and mentor, while working at the Institute for Software and Integrated Systems at Vanderbilt. His encouragement has helped me progress during my work over the past few years.

I would like to thank the remaining members of my Ph.D. committee: Dr. Prodyot Basu, Dr. Ravindra Duddu, and Dr. Florence Sanchez. From the moment I began my work at Vanderbilt University, their knowledge and support in my classes and research has been greatly appreciated.

I am very grateful for the opportunity to be in a research group with such knowledgeable, helpful and hard working members of the MCML. The willingness of everyone to help each other when needed has been unmatched, in our different areas of research. Thank you to the current and former members of the MCML that I have worked with during my time at Vanderbilt.

Thank you to my beautiful fiancèe Kelsey. Your strength and love has encouraged me to always stay positive and accomplish my goals. I could not have succeeded without you.

My parents have always believed in me and made sure that I have succeeded in every stage of my life. Thank you for your love and support. I would also like to thank my grandmother who has been extremely supportive throughout the years, my brother who has always believed in me and my family in Nashville which have been immensely encouraging. I would not be where I am today without their generosity and support. To would also like to thank my friends, who have provided me with support and encouragement over the past

few years. Thank you to the Nashville Brewers, for providing me the opportunity to have an outlet during my years of research.

Finally, I acknowledge the financial support from Vanderbilt University Civil Engineering department, Vanderbilt University through the Discovery grant program, the National Science Foundation CMMI division, and the Institute for Software and Integrated Systems at Vanderbilt University.

TABLE OF CONTENTS

LIST OF TABLES

Page

LIST OF FIGURES

Page

CHAPTER 1

INTRODUCTION

1.1 Motivation

Short fiber composites are used in a variety of disciplines and can be utilized to enhance performance. The composites provide significant benefits, not only in the mechanical characteristics as compared to the base material, but also provide different function properties. To accurately understand the response from the short fibers in the composites, they need to addressed carefully. Short fibers tend to have small diameter (or thickness) compared to the length of the fiber, resulting a high aspect ratio. Modeling high aspect ratio fibers in a domain is a difficult task and needs to be approached with a computationally efficient methodology.

This dissertation presents the development and formulation of the behavior of short fiber composites without the computational cost of standard analysis methods, to capture the complex composite behavior. The framework to model short fiber composites will be beneficial in various applications, including those which directly rely on short reinforced composites simulations for their system analysis. An improvement on the understanding of the response of the composites can lead to greater enhancements of composite materials. The main focus of this dissertation is to apply the extended finite element method (XFEM) to model short fiber composites.

1.2 Literature Review

Micro- and nano-fiber short fiber reinforced composites have been shown to exhibit good mechanical performance under static and dynamic loading conditions for a wide range of matrix materials and are frequently used in practice for a variety of engineering applications. The fibers can significantly effect elastic modulus, load carrying capacity, flexural

strength and flexural toughness (see e.g., [113, 118] for examples for cementitious materials). A key advantage of these composites is that they can be tailored to perform optimally under a range of loading and environmental conditions. Besides the superior mechanical properties, short fiber reinforcement introduces functional properties ranging from crack control, electromagnetic field shielding and self sensing, making them attractive for multi-functional applications (e.g. [24, 25, 43, 64, 95]).

Short fiber reinforced composite material modeling to extract elastic and inelastic homogenized properties, are traditionally conducted based on micromechanical modeling or through computational studies of representative volume elements (RVEs). The micromechanical modeling approaches are usually based on the Eshelby's solution of ellipsoidal inclusions embedded in a matrix in conjunction with Mori-Tanaka scheme (e.g., [17, 54, 104]), Hashin-Strichman bounds [89] and others. The ellipsoidal inclusions are taken to have a high aspect ratio to mimic the effect of the fiber geometries when such approaches are applied to model random fibers. The computational RVE modeling of the response of random fiber composites has also been proposed by a number of investigators [15, 28, 65]. The numerical analysis of RVEs based on the direct discretization of the microstructure is useful for analysis of microstructures with dilute concentrations of inclusions [14, 26, 35, 67, 91, 112], but is computationally not feasible in the presence of many, high aspect ratio fibers. The challenge lies with the resolution of randomly generated high aspect ratio fibers using discretization with small elements as well as ensuring mesh compatibility between the embedded fibers and the matrix when large number of fibers are present. Modeling progressive failure along interfaces between the fiber and the matrix also provides additional challenges. Resolving some of these challenges can be achieved by using the XFEM.

XFEM provides an approach to eliminate the need to discretize the individual fibers and the compatibility requirements of the underlying discretization. The primary idea of the XFEM approach is to enrich the standard finite element basis with nodal enrichment functions capable of representing inhomogeneities and discontinuities within the problem domain

without explicitly representing them through meshing [9, 32, 69]. XFEM utilizes enrichment functions to model the presence of inclusions and discontinuities in an otherwise uniform domain. The foundation of XFEM is the partition of unity method (PUM), which incorporates the enrichment function into the finite element framework, formalized by Babuska and Melenk [4]. In PUM, the nodal level enrichment is a product of the enrichment function and the standard shape functions that satisfy the partition of unity property for the enrichment, in addition to the standard basis. The enrichment functions are known a-priori to represent the response well within the whole domain or a subdomain of the problem, around strong or weak discontinuities. XFEM has been widely employed to model strong (e.g., cracks) and weak discontinuities (e.g., inclusions) [19, 40, 60, 62, 101]. The XFEM approach has seen a rapid development in the past decade, which is summarized in Refs. [11, 72].

The XFEM approach has been widely used recently to approximate solutions of domains with discontinuities. Sukumar et al. [102] presented a methodology to model arbitrary holes and inclusions without remeshing the internal boundaries. The method couples the level set method with the XFEM method. Belytschko et al. [10] proposed a technique for modeling arbitrary (including potentially intersecting) discontinuities in finite elements. The approximation for discontinuous elements uses the XFEM form and the surfaces of the discontinuities by the signed distance function. Chen et al. [22] reviewed the treatment of tip, fully and partial enrichment of the finite elements and corresponding numerical integration techniques in the context of the XFEM approach. XFEM modeling work have addressed inclusions that can be represented as a sub-domain of the problem domain (e.g., spherical inclusions) or cracks, and are important contributions to the XFEM emergence. The high aspect ratio short fiber modeling provides a different challenge, in which the fiber occupies an insignificant volume in the domain, but is modeled as a weak discontinuity.

While the XFEM approach can be used to model the cracks and inclusions (e.g. [12, 31, 60, 101, 102]), it does not readily account for the progressive debonding along the inclusion interfaces. The performance of short fiber reinforced composites are significantly affected by

interface properties. Cohesive zone modeling has been the traditional approach to idealize progressive debonding along inclusion interfaces. Zero-thickness elements between solid elements that discretize the neighboring domains describe the separation between two surfaces and relate surface tractions to the displacement jumps through a softening constitutive equation (i.e., a cohesive law). Cohesive zone modeling applied to fiber reinforced composites are available for pure mode and mixed mode cohesive laws in [44, 63, 75, 77, 80, 110, 116], among many others.

Cohesive zone modeling has recently been incorporated into the XFEM framework. Moës and Belytschko [68] and Unger et al. [106] have proposed methods to model cohesive crack growth in concrete. Zi and Belytschko [120] presented a formulation of crack tip elements for cohesive cracks. Work on partly cracked XFEM elements with cohesive cracks was performed by Asferg et al. [3]. Bouhala et al. [18] focused on the interfacial debonding of cracks for long fiber reinforced composites. Other applications include the regularization of the discontinuity at cohesive interfaces for modeling delamination in composites [13] and in the context of a multiscale framework for composites combining XFEM with cohesive zone laws [52]. Radtke et al. [93] developed a method using a Heaviside enrichment function to account for the strong discontinuity present due to tangential debonding at the fiber-matrix interface. The weak discontinuity in the response field due to the presence of the fiber was not included in the response field approximation. A non-linear cohesive law was employed to describe tangential slip along the fiber-matrix interface and the normal fiber-matrix interface separation was suppressed.

Capturing the mechanical behavior of high density, high aspect ratio fiber reinforced composites in a computationally efficient way requires that the underlying XFEM formulation accommodates the presence of many fibers that are close to each other. A way to alleviate numerical problems that arise from the presence of multiple enrichment functions within the same finite element is local mesh refinement. Within the XFEM framework, the discretization around enrichments are made fine enough that multiple enrichments do not

occur within the same element [42]. Other XFEM approaches have been proposed to capture the effect of multiple cracks in the same element, including intersecting cracks and crack growth [20, 96]. The integration of elements with multiple cracks is achieved by splitting up the element domain into sections and using higher order integration [30, 121]. Hiriyur et al. [53], proposed a method to account for multiple inclusions in the same element domain by introducing additional degrees of freedom for each inclusion enrichment, removing the need to finely discretize the domain around neighboring inclusions. In contrast, literature on accounting for multiple debonding processes within the same element is scarce, to the best of the author's knowledge.

The enrichment idea to eliminate the need to discretize individual fibers has been recently proposed. Fiber composite modeling using the partition of unity method was proposed by Radtke et al. [92, 93], where high aspect ratio fibers were modeled as zero measure elastic inclusions for idealizing fiber reinforced composite behavior, eliminating the need to discretize the fibers. Embedment methods for fibers in reinforced composites have also been proposed to eliminate the need to discretize individual fibers. Two and three dimensional models have been developed for embedded fibers that include the modeling of fiber slip in the domain by adding additional degrees of freedom [6, 34, 51, 66]. Similar in principles to the XFEM modeling, other methods to embed discontinuities have been proposed (e.g., [50, 57, 99]). Fish and coworkers proposed a mathematical homogenization based approach to include weak discontinuities in a heterogeneous domain [38], and employed the s-version finite element method to embed strong discontinuities in a finite element mesh [36].

1.3 Dissertation Goal and Objectives

The primary goal of this dissertation is to accurately model the response of short fiber reinforced composites using the efficient computational methodology of the extended finite element method. The research objectives are as follows:

1. Develop an XFEM approach to model composites with rigid short fibers in two di-

mensions;

2. Model short deformable fiber composites using XFEM with material cohesive interfaces and a continuum damage model in two dimensions;

3. Use the XFEM approach to capture the interactions between short fibers in fiber reinforced composites;

4. Utilize the ideas and principles from the XFEM formulation in two dimensions to model short fiber composites in a three dimensional domain.

1.4 Dissertation Organization

The first research objective is addressed by formulation of XFEM for random short fiber reinforced composites in two dimensions in Chapter 2. The fibers are considered to be rigid and the numerical analysis of the short fiber composites is validated with the direct finite element method. In Chapter 3, the second objective is covered. Random short fiber composites are modeled using XFEM, in which the fibers are deformable and have material cohesive interfaces. Numerical examples are presented for various fiber configurations including the use of continuum damage mechanics in two dimensions. Chapter 4 presents a two dimensional XFEM approach to capture the interactions between short fibers in reinforced fiber composites. Numerical assessment is validated with the direct finite element method including the interaction response between the fibers. The final research objective for this dissertation is addressed in Chapter 5. A three dimensional XFEM formulation for random short fiber composites is developed for two dimensional high aspect ratio planar fibers. Fibers remain elastic and debonding occurs on the fiber-matrix interface. The methodology is assessed with reference to the direct finite element method with numerical examples. The work in this dissertation is summarized in Chapter 6.

CHAPTER 2

MODELING RIGID RANDOM SHORT FIBER REINFORCED COMPOSITES USING XFEM

2.1 Introduction

This chapter provides formulation and implementation of XFEM for random rigid short fiber reinforced composite materials (Fig 2.1). XFEM is utilized in this work to investigate the behavior of short fiber reinforced composite materials. The work in this chapter is reflected in Ref. [86], and presented with permission from ASCE.

In this chapter, XFEM for random short fiber reinforced composite materials is presented. An enrichment function is derived to incorporate the effect of random fiber inclusions within the XFEM framework to eliminate the need of using finite element meshes compliant with fiber inclusions. A key contribution is to extend the XFEM for modeling weak discontinuities for inclusions that does not occupy volume. To this effect, the fibers are approximated as line discontinuities in a multi-dimensional domain. The fibers are assumed to behave as a rigid body with no stretching or bending. The motion of the fiber inclusions are modeled by constraining the deformation field along the domain of the fiber inclusions. Coupling the XFEM method with the new enrichment function and constraint equations formulate the elastic response of short fiber reinforced composites. Numerical integration procedures are provided for accurate evaluation of the system response for fiber tips that lie on arbitrary positions within the problem domain. The performance of the XFEM model is verified against the direct finite element method.

The remainder of this chapter is organized as follows. In Section 2.2, the fundamental concepts of the XFEM method are introduced and discussed. In Section 2.3, the application of the XFEM method to short fiber reinforced composite materials. The fiber inclusion enrichment function and constraints to define fiber motion is described. Section 2.4 provides

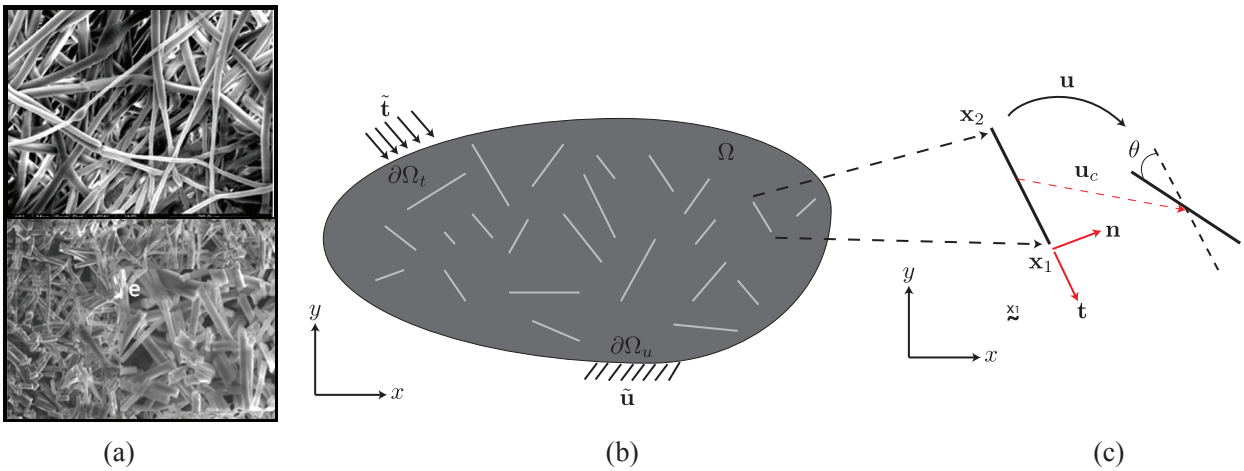

Figure 2.1: (a) Short fiber reinforced composite (from [94], © IOP Publishing. Reproduced by permission of IOP Publishing. All rights reserved); (b) domain of the short fiber reinforced composite; (c) short fiber kinematics.

the governing equations, the numerical formulation of the XFEM method for short fiber reinforced composites and the treatment of partially enriched elements. The assessment of the performance of the approach is presented in Section 2.5.

2.2 The Extended Finite Element Method

Modeling the fiber geometry of short fiber reinforced composites with very high aspect ratios can be infeasible within the finite element method (Fig. 2.2), particularly when a large number of fibers is present. In this work, the extended finite element method (XFEM) is employed to eliminate the need to conform the discretization to the individual fibers.

XFEM is based on the expression of the response field using the following approximation:

$$\mathbf{u}(\mathbf{x},t) = \sum_{a=1}^{n_n} N_a(\mathbf{x})\hat{\mathbf{u}}_a + \sum_{b=1}^{n_{\text{en}}} N_{\mathcal{I}_b}(\mathbf{x})\psi(\mathbf{x})\hat{\mathbf{c}}_b \tag{2.1}$$

in which, $\mathbf{u}$ denotes the displacement field; $\mathbf{x}$ and t are the space and time coordinates, respectively; n_n the total number of mesh nodes in the finite element discretization; n_{en}^{α} is the number of enriched nodes per fiber; N_a, the standard finite element shape function associated with node a; $\hat{\mathbf{u}}_a$ and $\hat{\mathbf{c}}_b$ the nodal coefficients of the standard and fiber enrichment,

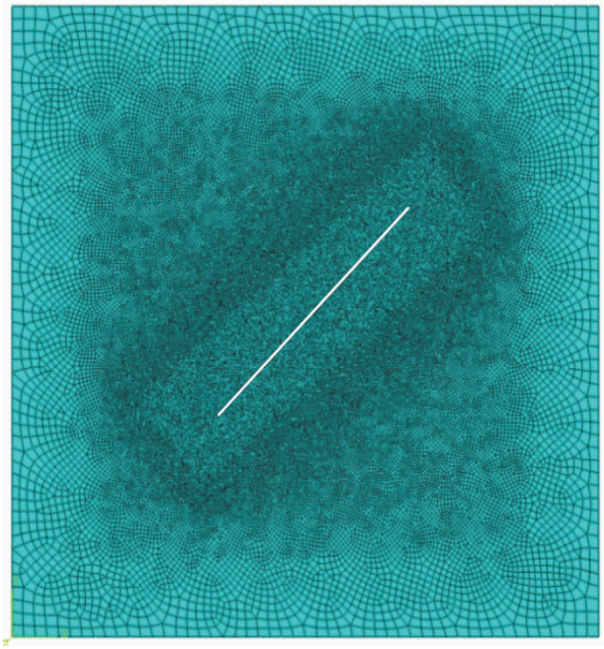

Figure 2.2: Standard finite element mesh for a short fiber inclusion composite.

respectively; $\mathcal{I}$ index set of enriched nodes; $\mathcal{I}_a \in \mathcal{I}$ the index of an enriched node, a; andψ the fiber enrichment function. The first right hand side term of Eq. 2.1 corresponds to the standard finite element approximation of the response field, whereas the second part is the enrichment to the approximation space based on a predefined enrichment function, ψ. The enrichment function is known a-priori to represent the response well within the whole domain or a subdomain of the problem, such as around strong or weak discontinuities. The index set, $\mathcal{I}$ reflects the extent to which the domain of the problem is enriched.

2.3 Modeling Embedded Short Fibers

This section presents the XFEM enrichment functions that will be employed in modeling the deformation response of short fibers embedded in a matrix. The short fibers are modeled as one-dimensional rods in view of their very high aspect ratios. The displacement of the fibers within the problem domain under loading is enforced through constraint equations described in Section 2.3.2.

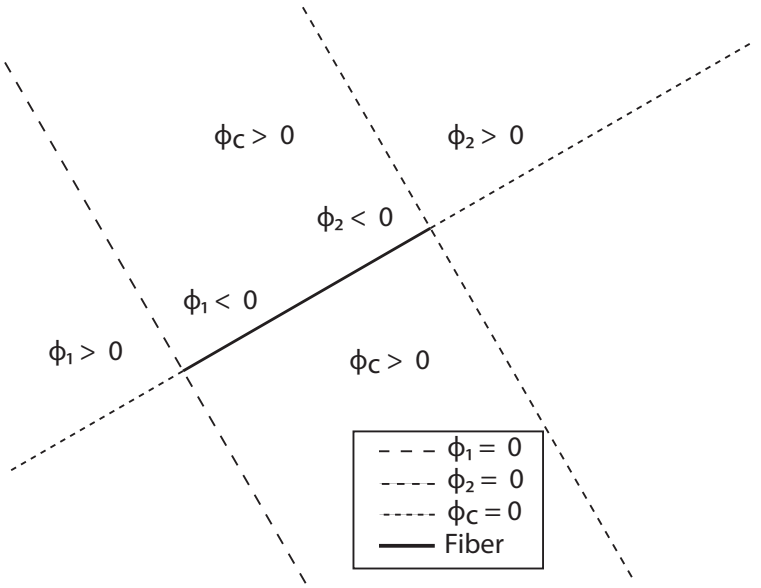

Figure 2.3: Level set functions of the enrichment.

2.3.1 Enrichment function

Development of an enrichment function for short fiber inclusions is achieved through defining level set functions for the fiber domain and the fiber tips separately. In a fiber reinforced composite, there exists a multitude of fibers each of which much be represented using a separate enrichment function. For the simplicity of the presentation, a single inclusion to derive the enrichment function is considered. The application of the enrichment function to address multiple fibers is straightforward provided that no overlapping occurs. The overlapping refers to the presence of multiple fibers within a single finite element as opposed to overlapping of the fiber domains, which is nonphysical and avoided.

Let $\Omega \subset \mathbb{R}^d$ be the open bounded domain of the composite body, where $d = 2, 3$ is the number of space dimensions. The reinforcing fibers are entirely embedded in Ω, and are taken to be straight with very high aspect ratio compared to the overall size of the composite body. The domain of a single fiber is therefore approximated by a line segment, parameterized by s, such that:

$$\mathbf{x} = \mathbf{x}_c + \frac{\mathbf{x}_2 - \mathbf{x}_1}{2} s; \quad -1 \leq s \leq 1; \quad \mathbf{x} \in \Gamma \tag{2.2}$$

where, $\mathbf{x}_1$ and $\mathbf{x}_2$ denote the positions of the fiber tips, and $\mathbf{x}_c$ the position of the center of the fiber (i.e., $\mathbf{x}_c = (\mathbf{x}_1 + \mathbf{x}_2)/2$). The level set functions associated with the fiber tips are expressed as:

$$\phi_\lambda(\mathbf{x}) = (\mathbf{x} - \mathbf{x}_\lambda) \cdot \mathbf{t}_\lambda; \quad \lambda = 1, 2 \tag{2.3}$$

in which, $\mathbf{t}_\lambda$ denotes the tangent at the corresponding fiber tip (i.e., $\mathbf{t}_1 = (\mathbf{x}_1 - \mathbf{x}_2)/l$ and $\mathbf{t}_2 = (\mathbf{x}_2 - \mathbf{x}_1)/l = -\mathbf{t}_1$). $l = \|\mathbf{x}_2 - \mathbf{x}_1\|$ denotes the length of the fiber. Figure 2.3 illustrates the level set functions associated with the fiber tips. ϕ_λ provides the zero level set along the plane normal to the fiber passing through the fiber tip. ϕ_λ is positive on one side of the domain cut by the zero level set, and negative elsewhere within the composite body as shown in Fig. 2.3.

The level set associated with the domain of the fiber, $\phi_c(\mathbf{x})$, divides the domain of the body along the plane of the fiber with positive values on each side and has zero value along the fiber:

$$\phi_c(\mathbf{x}) = \|\mathbf{x} - \mathcal{P}(\mathbf{x})\| \tag{2.4}$$

in which, $\mathcal{P}(\mathbf{x})$ is the projection of $\mathbf{x}$ onto the fiber:

$$\mathcal{P}(\mathbf{x}) = \mathbf{x}_1 + [(\mathbf{x} - \mathbf{x}_1) \cdot \mathbf{t}_2]\,\mathbf{t}_2 = \mathbf{x}_2 + [(\mathbf{x} - \mathbf{x}_2) \cdot \mathbf{t}_1]\,\mathbf{t}_1 \tag{2.5}$$

Employing Eqs. 2.3 and 2.4, the enrichment function for the fiber is written as:

$$\psi(\mathbf{x}) = \left[\prod_{\lambda=1}^{2} H(-\phi_\lambda)\right] \phi_c(\mathbf{x}) + \sum_{\lambda=1}^{2} H(\phi_\lambda) d_\lambda(\mathbf{x}) \tag{2.6}$$

where H denotes the Heaviside function,

$$H(f) = \begin{cases} 1 & f \geq 0 \\ 0 & f < 0 \end{cases} \tag{2.7}$$

and $d_\lambda(\mathbf{x}) = \|\mathbf{x} - \mathbf{x}_\lambda\|$ denotes the distance function to the fiber tip, λ. The enrichment

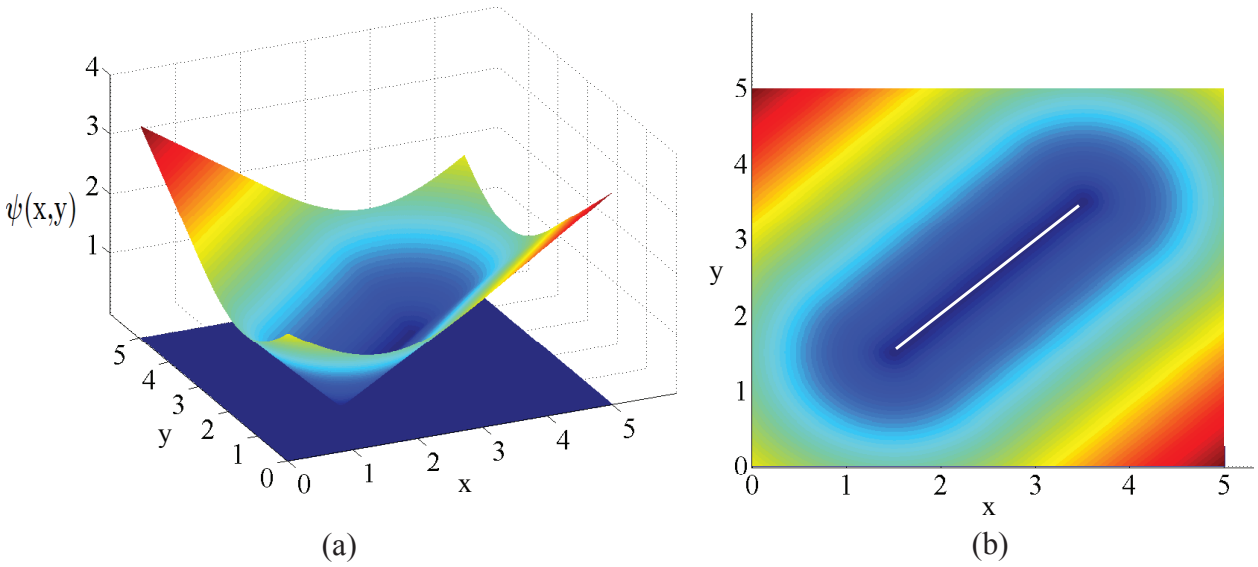

Figure 2.4: Short fiber inclusion enrichment function: (a) three dimensional view; (b) planar view (fiber is illustrated by the white line).

function expressed in Eq. 2.6 has the form of the V-shaped enrichment functions employed in inclusion problems [71], with caps defined at the tips of the fiber. Adding $\psi(\mathbf{x})$ to the approximation basis of the solution field introduces a strain discontinuity mode along the position of the fiber. The displacements around the fiber can therefore be accurately captured without explicitly discretizing the fiber domain. The particular form chosen for $\psi(\mathbf{x})$ (Eq. 2.6) ensures that approximation basis captures the strain discontinuity but stay smooth otherwise around the tip and sides of the fiber. Three dimensional and planar views of the enrichment function are illustrated in Fig. 2.4 a and b. The enrichment functions around a fiber tip multiplied by the finite element shape functions of a quadrilateral element are illustrated in Fig. 2.5.

The enrichment function in Eq. 2.6 is nonzero everywhere in the composite domain except on the fiber. The direct application of this enrichment function therefore leads to the enrichment of all nodes within the domain. This is undesirable since away from the fiber, the enrichment does not enlarge the trial space spanned by the standard finite element shape functions, yet increases the size of the linear system. This is circumvented by considering the enrichment of a small subdomain around the fiber, while employing standard finite element

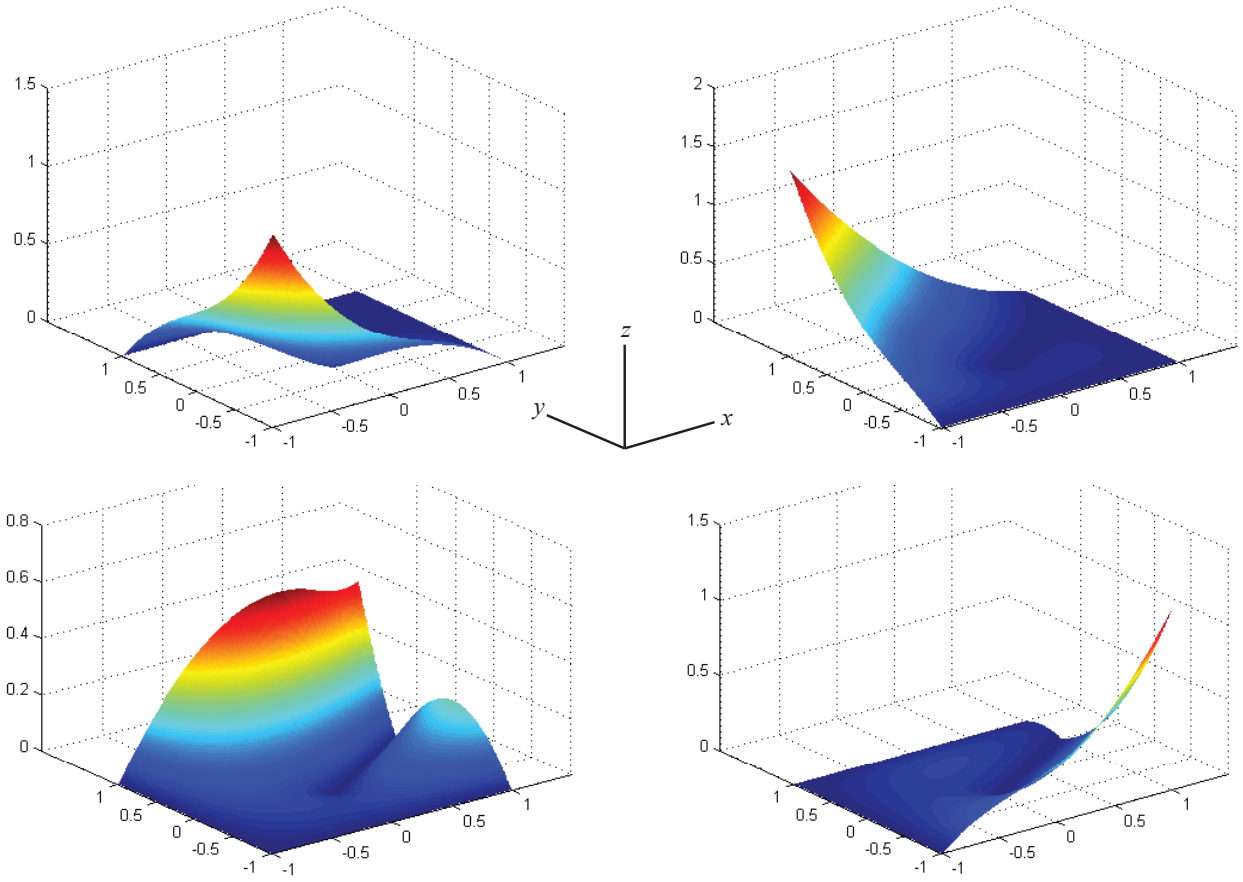

Figure 2.5: The nodal enrichments computed for a 2-D quadrilateral element. The fiber tip is within the element domain.

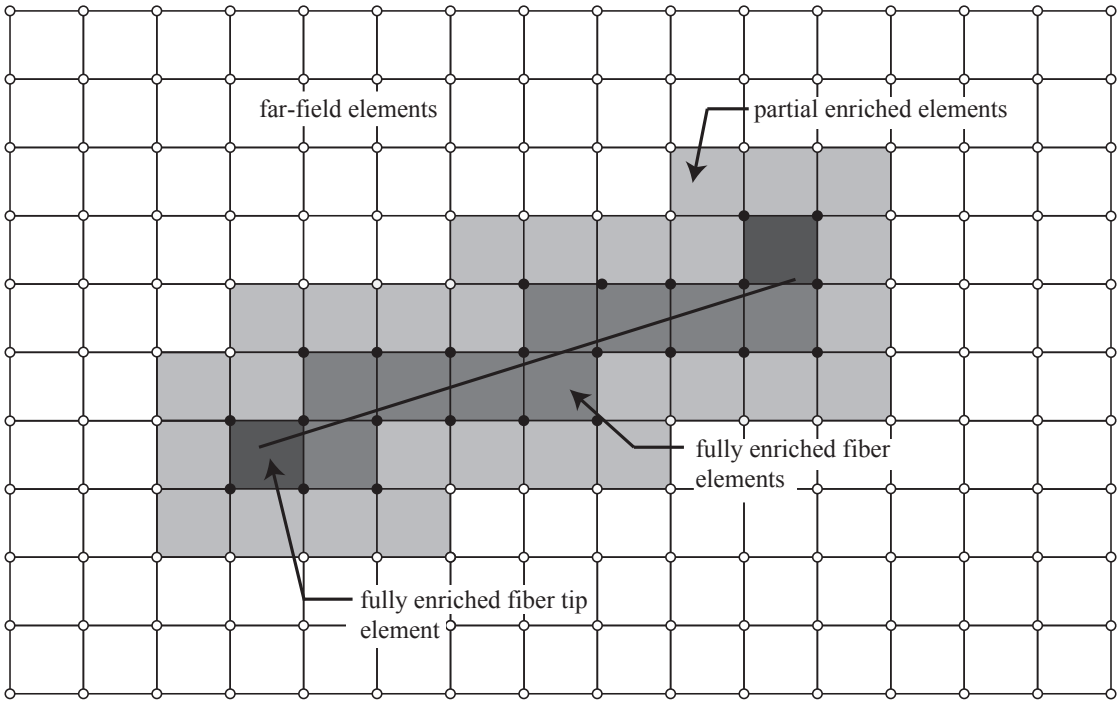

Figure 2.6: The decomposition of the problem domain into subdomains of far-field elements approximated by standard basis, partially and fully enriched elements.

shape functions in the remainder of the problem domain. By this approach, the domain of the composite is taken to consist of four regions as illustrated in Fig. 2.6: (1) Far field elements with no enrichment; (2) elements with partial enrichment; (3) fully enriched elements crossed by the fiber; and (4) fully enriched elements partially crossed by the fiber that contain the fiber tip. The support of the enrichment region is provided by the sides (or faces) of the partially enriched elements formed by their standard nodes. The numerical treatment of the regions are different from each other and described in Section 2.4.3. As illustrated in Fig. 2.6, the enrichment domain is chosen based on the discretization as opposed to the geometry of the problem domain that is typically used in crack modeling with XFEM (e.g., crack tip enrichment defined within a specified radius from the crack tip). Since the fiber tip enrichment functions employed in this study are not defined based on geometry and smoothly vary (similar to the Heaviside enrichments employed on the sides of the fibers or crack faces), geometry based enrichment domain selection is not critical to the method performance.

2.3.2 Rigid fiber constraints

The enrichment function provides the necessary weak (i.e., strain) discontinuity within a finite element to describe the effect of inclusion on the response of the matrix around it, but does not incorporate the kinematics of the fiber itself. The deformation of the fiber inclusion is typically a function of the stiffness contrast between the fiber and the matrix, flexural rigidity and the length of the fiber. For relatively short fibers embedded in matrix of significantly lower stiffness, the bending and stretching of the fiber are small. Early works indicate a relative insensitivity of the overall composite stiffness to constituent stiffness ratio, particularly at high values [97]. In this chapter, the fibers are idealized as rigid bodies going through only translation and rotation but no bending and stretching. This condition may be imposed by considering the following constraint:

$$\mathbf{g}(\mathbf{x}) := \mathbf{u}(\mathbf{x}) - \mathbf{u}_c - (\mathbf{R} - \boldsymbol{\delta}) \cdot (\mathbf{x} - \mathbf{x}_c) = \mathbf{0}; \quad \mathbf{x} \in \Gamma \tag{2.8}$$

in which, $\mathbf{u}_c$ is a constant vector of translation, $\mathbf{R}$ the orthogonal tensor of rigid body rotation about the center of the fiber; and $\boldsymbol{\delta}$ the Kronecker Delta. The orthogonal transformation imposed by the rigid body rotation constraint is valid for large rotations, but is a nonlinear constraint. Assuming the rotation of the rigid fiber supported by the matrix remains small, Eq. 2.8 is rewritten using a linear constraint equation as:

$$\mathbf{g}(\mathbf{x}) := \mathbf{u}(\mathbf{x}) - \mathbf{u}_c - \frac{l}{2} s\left(\mathbf{x}\right) \theta_R \mathbf{n} = \mathbf{0}; \quad \mathbf{x} \in \Gamma \tag{2.9}$$

where, θ_R is the angle of rotation, and $\mathbf{n}$ the normal to the fiber direction as illustrated in Fig. 2.1c. Equation 2.9 implies that the rotational component of the fiber deformation is normal to the original fiber orientation, which is valid for small θ_R.

2.4 Governing Equations and Formulation

The governing equations for the deformation response of the short fiber reinforced composite are:

$$\nabla \cdot \boldsymbol{\sigma}(\mathbf{x}, t) = 0; \quad \mathbf{x} \in \Omega \tag{2.10}$$

and;

$$\boldsymbol{\sigma} = \mathbf{L} : \boldsymbol{\epsilon}(\mathbf{x}, t) = \mathbf{L} : \nabla^s \mathbf{u}(\mathbf{x}); \quad \mathbf{x} \in \Omega \tag{2.11}$$

where, σ is the stress tensor; ϵ the strain tensor given as the symmetric gradient of the displacement field, $\mathbf{u}$; and $\mathbf{L}$ is the tensor of elastic moduli of the matrix material. $\mathbf{L}$ is taken to be symmetric and positive definite.

The exterior boundary conditions are expressed as:

$$\mathbf{u}(\mathbf{x}, t) = \tilde{\mathbf{u}}(\mathbf{x}, t); \quad \mathbf{x} \in \Gamma_u \tag{2.12}$$

$$\boldsymbol{\sigma} \cdot \boldsymbol{n} = \tilde{\mathbf{t}}(\mathbf{x}, t); \quad \mathbf{x} \in \Gamma_t \tag{2.13}$$

in which, $\tilde{\mathbf{u}}$ and $\tilde{\mathbf{t}}$ are the prescribed boundary displacements and tractions defined on boundaries Γ_u and Γ_t, respectively, such that $\Gamma_u \cap \Gamma_t = \emptyset$ and $\partial\Omega = \Gamma_u \cup \Gamma_t$.

The domain of the composite body includes n straight fibers with varying length and orientations. Neglecting the bending and stretching of the fibers and assuming small rotations of the fibers, the following constraint equations are imposed on the displacement response of the composite:

$$\mathbf{u}(\mathbf{x}) = \mathbf{u}_c^\alpha + \frac{l}{2} s^\alpha(\mathbf{x}) \theta_R^\alpha \mathbf{n}^\alpha; \quad \mathbf{x} \in \Gamma_\alpha; \quad \alpha = 1, 2, \ldots, n \tag{2.14}$$

Superscript α, indicates α^{th} fiber.

2.4.1 XFEM formulation

The extended finite element method is employed to discretize and evaluate the governing equations (Eqs. 2.10-2.14). Using the standard Ritz-Galerkin procedure and employing the penalty function formulation for imposing the constraints, given the boundary data and the matrix elastic moduli matrix, find $\mathbf{u} \in \mathcal{U}_{\tilde{\mathbf{u}}}$ such that for all $\delta\boldsymbol{u} \in \mathcal{U}_{\mathbf{0}}$, the problem can be posed in the weak form as:

$$\int_{\Omega} \delta\boldsymbol{\epsilon} : \mathbf{L} : \boldsymbol{\epsilon}\, d\Omega + \sum_{\alpha=1}^{n} \int_{\Gamma_\alpha} \gamma \delta\boldsymbol{u} \cdot \mathbf{g}^{\alpha}\, d\Gamma = \int_{\partial\Omega_t} \delta\boldsymbol{u} \cdot \tilde{\mathbf{t}}\, d\Gamma \tag{2.15}$$

where $\delta\boldsymbol{u}$ denotes the test function; $\delta\boldsymbol{\epsilon}$ the gradient of the test function; $\mathbf{g}^{\alpha}$ is the displacement constraint for fiber, α; γ the penalty parameter chosen sufficiently large to ensure enforcement of the constraint equations. The appropriate spaces for the trial and test functions are:

$$\mathcal{U}_{\delta\boldsymbol{u}} := \left\{ \mathbf{u} \in \left[H^1(\Omega)\right]^d \;\middle|\; \mathbf{u} = \delta\boldsymbol{u} \text{ on } \mathbf{x} \in \partial\Omega_u \right\} \tag{2.16}$$

where, $H^1(\Omega)$ is the Sobolev space of functions with square integrable values and derivatives defined on the problem domain. The subscript $\delta\boldsymbol{u}$ is equal to $\tilde{\mathbf{u}}$ (i.e., the prescribed boundary data) in the case of the trial function and equal to zero in the case of the test function.

The discretization of the displacement field follows Eq. 2.1, and using the Bubnov-Galerkin approach, the discretization of the test function is similar to that of the trial function. In contrast to the standard finite element approach, the mesh does not necessarily conform to the fiber domains, i.e., the position of the fibers are independent of the mesh. The first term in Eq. 2.15 is then expressed as:

$$\int_{\Omega} \nabla\delta\boldsymbol{\epsilon} : \mathbf{L} : \boldsymbol{\epsilon}\, d\Omega = \sum_{e=1}^{n_e} \int_{\Omega_e} \delta\boldsymbol{\epsilon} : \mathbf{L} : \boldsymbol{\epsilon}\, d\Omega \tag{2.17}$$

in which, n_e is the total number of elements; and Ω_e the domain of the element, e. Substituting Eq. 2.1 into Eq. 2.17 and switching to the Voigt notation with contracted indices for

simplicity, the element level integral is expressed as:

$$\int_{\Omega_e} \delta\boldsymbol{\epsilon} : \mathbf{L} : \boldsymbol{\epsilon}\, d\Omega = (\mathbf{V}^e)^T \int_{\Omega_e} (\mathbf{B}^e)^T \mathbf{L}\, \mathbf{B}^e\, d\Omega\, \mathbf{U}^e = (\mathbf{V}^e)^T \mathbf{K}^e \mathbf{U}^e \tag{2.18}$$

in which, superscript T denotes the transpose operator; and $\mathbf{U}^e$ and $\mathbf{V}^e$ denote the vectors of nodal coefficients of the trial and test functions in element, e:

$$\mathbf{U}^e = \{\hat{\mathbf{u}}^e;\, \hat{\mathbf{c}}^e\}\,; \quad \mathbf{V}^e = \{\delta\hat{\mathbf{u}}^e;\, \delta\hat{\mathbf{c}}^e\} \tag{2.19}$$

in which, a semicolon implies that the construction forms a column vector. The components in the nodal coefficient vectors correspond to the standard and fiber enrichment degrees of freedom respectively:

$$\hat{\mathbf{u}}^e = \left\{\hat{\mathbf{u}}^e_1;\, \hat{\mathbf{u}}^e_2;\, \ldots;\, \hat{\mathbf{u}}^e_{n^e_n}\right\} \quad \hat{\mathbf{c}}^e = \left\{\hat{\mathbf{c}}^e_1;\, \hat{\mathbf{c}}^e_2;\, \ldots;\, \hat{\mathbf{c}}^e_{n^e_{\text{en}}}\right\} \tag{2.20}$$

where, $\hat{\mathbf{u}}^e_a$ and $\hat{\mathbf{c}}^e_a$ are the vectors of unknown coefficients for standard and extended degrees of freedom at element, e and node a; and n^e_n and n^e_{en} the number of standard and enriched nodes within element, e, respectively. The components of $\mathbf{V}^e$ are similarly defined. $\mathbf{B}^e$ corresponds to the gradient operation expressed as:

$$\mathbf{B}^e = \left\{\hat{\mathbf{B}}^e_1\ \hat{\mathbf{B}}^e_2 \ldots \hat{\mathbf{B}}^e_{n^e_n}\ \bar{\mathbf{B}}^e_1,\ \bar{\mathbf{B}}^e_2,\ \ldots,\ \bar{\mathbf{B}}^e_{n^e_{\text{en}}}\right\} \tag{2.21}$$

in which, the gradient terms are expressed as:

$$\hat{\mathbf{B}}^e_a = \begin{bmatrix} N^e_{a,x} & 0 \\ 0 & N^e_{a,y} \\ N^e_{a,y} & N^e_{a,x} \end{bmatrix}; \; \bar{\mathbf{B}}^e_a = \begin{bmatrix} (N^e_a\,\psi)_{,x} & 0 \\ 0 & (N^e_a\,\psi)_{,y} \\ (N^e_a\,\psi)_{,y} & (N^e_a\,\psi)_{,x} \end{bmatrix} \tag{2.22}$$

where, a subscript followed by a comma indicates differentiation. For the enrichment degrees

of freedom, the gradient operation takes the form:

$$\bar{\mathbf{B}}_a^e(\mathbf{x}) = \hat{\mathbf{B}}_a^e(\mathbf{x})\,\psi(\mathbf{x}) + \tilde{\mathbf{B}}_a^e(\mathbf{x}) \tag{2.23}$$

The formulation of the third term in Eq. 2.15 proceeds similarly. Decomposing the boundary integral into its elemental components yields:

$$\int_{\Gamma_t} \delta\boldsymbol{u}\cdot\tilde{\mathbf{t}}\,d\Gamma = \sum_{e\in I_t}\int_{\Gamma_t}\delta\boldsymbol{u}\cdot\tilde{\mathbf{t}}\,d\Gamma \tag{2.24}$$

in which, I_t denotes the index set of elements at the boundary Γ_t. Substituting Eq. 2.1 into Eq. 2.24, the element level boundary integral is expressed as:

$$\int_{\Gamma_t}\delta\boldsymbol{u}\cdot\tilde{\mathbf{t}}\,d\Gamma = (\mathbf{V}^e)^T\int_{\Gamma_t}\mathbf{f}^e(\mathbf{x})\,d\Gamma = (\mathbf{V}^e)^T\mathbf{F}^e \tag{2.25}$$

where,

$$\mathbf{f}^e = \left\{\hat{\mathbf{f}}_1^e;\,\hat{\mathbf{f}}_2^e;\,\ldots;\,\hat{\mathbf{f}}_{n_n^e}^e;\,\bar{\mathbf{f}}_1^e;\,\bar{\mathbf{f}}_2^e;\,\ldots;\,\bar{\mathbf{f}}_{n_{\text{en}}^e}^e\right\} \tag{2.26}$$

The components of the element force vector are:

$$\hat{\mathbf{f}}_a^e(\mathbf{x}) = N_a^e(\mathbf{x})\,\tilde{\mathbf{t}}(\mathbf{x})\,;\quad \bar{\mathbf{f}}_a^e(\mathbf{x}) = \hat{\mathbf{f}}_a^e(\mathbf{x})\,\psi(\mathbf{x}) \tag{2.27}$$

Defining the global vector of unknown nodal coefficients as:

$$\mathbf{U} = \{\hat{\mathbf{u}}_1;\hat{\mathbf{u}}_2;\ldots\hat{\mathbf{u}}_{n_n};\hat{\mathbf{c}}_1;\hat{\mathbf{c}}_2;\ldots\hat{\mathbf{c}}_{n_{en}}\} \tag{2.28}$$

The global stiffness matrix, $\hat{\mathbf{K}}$ and the force vectors are obtained by assembling the corresponding element matrices (i.e., $\mathbf{K}^e$ and $\mathbf{F}^e$):

$$\hat{\mathbf{K}} = \mathop{\mathbf{A}}_{e=1}^{n_e}\mathbf{K}^e;\quad \mathbf{F} = \mathop{\mathbf{A}}_{e=1}^{n_e}\mathbf{F}^e; \tag{2.29}$$

2.4.2 Constraint equations

The constraint equation for the α^{th} fiber ($\mathbf{g}^\alpha$) indicates that the motion of the fiber is fully defined by a translation vector and a rotation angle. These unknowns are interpreted as the translation of the fiber midpoint (i.e., $\mathbf{u}_c^\alpha$) and the rotation angle of the fiber about the fiber midpoint (i.e., θ_R^α). The translation vector is obtained as a function of the displacement field by integrating the constraint equation over the domain of the fiber and normalizing with the fiber length:

$$\frac{1}{l^\alpha}\int_{\Gamma_\alpha}\mathbf{g}^\alpha(\mathbf{x})\,d\Gamma = \frac{1}{l^\alpha}\int_{\Gamma_\alpha}\mathbf{u}(\mathbf{x})\,d\Gamma - \mathbf{u}_c^\alpha - \frac{\theta_R^\alpha}{2}\int_{\Gamma_\alpha}s(\mathbf{x})\,d\Gamma\mathbf{n}^\alpha = \mathbf{0} \tag{2.30}$$

Observing that the rotation term vanishes, the translation vector reads:

$$\mathbf{u}_c^\alpha = \frac{1}{l^\alpha}\int_{\Gamma_\alpha}\mathbf{u}(\mathbf{x})\,d\Gamma \tag{2.31}$$

The rotation angle is obtained by taking the inner product of the constraint equation with the fiber normal, $\mathbf{n}^\alpha$ and averaging over the domain of the fiber:

$$\theta_R^\alpha = \frac{2}{(l^\alpha)^2}\int_{\Gamma_\alpha}\frac{\mathbf{u}(\mathbf{x})\cdot\mathbf{n}^\alpha}{s(\mathbf{x})}d\Gamma \tag{2.32}$$

The constraint equation for fiber, α becomes:

$$\mathbf{g}^\alpha(\mathbf{x}) = \mathbf{u}(\mathbf{x}) - \frac{1}{l^\alpha}\int_{\Gamma_\alpha}\mathbf{u}(\mathbf{x})\,d\Gamma - \frac{1}{l^\alpha}s(\mathbf{x})\int_{\Gamma_\alpha}\frac{\mathbf{u}(\mathbf{x})\cdot\mathbf{n}^\alpha}{s(\mathbf{x})}d\Gamma\,\mathbf{n}^\alpha \tag{2.33}$$

The enrichment function ψ vanishes within the fiber domain due to the zero level set functions as illustrated in Fig. 2.4. Therefore only the the standard shape functions are employed in the discretization of the displacement field along the fiber domain and the enrichment function does not affect the imposition of the constraint. Substituting Eq. 2.33 into Eq. 2.15 and decomposing the integral into element contributions, the first term of the constraint

equation is written as:

$$\int_{\Gamma^\alpha} \gamma \delta \boldsymbol{u}\left(\mathbf{x}\right) \cdot \mathbf{u}\left(\mathbf{x}\right)\, d\Gamma = \sum_{e \in I^\alpha} \int_{\Gamma_\alpha^e} \gamma \delta \boldsymbol{u}\left(\mathbf{x}\right) \cdot \mathbf{u}\left(\mathbf{x}\right)\, d\Gamma \tag{2.34}$$

where, I^α is the index set of all fully enriched elements crossed by the fiber, α. The element level integration is expressed in the vector form as follows:

$$\int_{\Gamma_\alpha^e} \gamma \delta \boldsymbol{u}\left(\mathbf{x}\right) \cdot \mathbf{u}\left(\mathbf{x}\right)\, d\Gamma = (\mathbf{V}^e)^T \int_{\Gamma_\alpha^e} \gamma (\hat{\mathbf{N}}^e)^T \hat{\mathbf{N}}^e d\Gamma\, \mathbf{U}^e = (\mathbf{V}^e)^T \mathbf{K}_{c1}^{e\alpha} \mathbf{U}^e \tag{2.35}$$

where,

$$\hat{\mathbf{N}}^e\left(\mathbf{x}\right) = \left\{ N_1^e \boldsymbol{\delta}\ N_2^e \boldsymbol{\delta} \ldots N_{n_n^e}^e \boldsymbol{\delta} \right\}^T \tag{2.36}$$

$\boldsymbol{\delta}$ is the Kronecker delta. The contribution of the first term of the penalty function to the global system of equations can be computed using the standard assembly operation:

$$\hat{\mathbf{K}}_{c1}^{\alpha} = \mathop{\mathbf{A}}_{e=1}^{n_e} \mathbf{K}_{c1}^{e\alpha} \tag{2.37}$$

The second and the third terms of the constraint equation take the following form when expressed in terms of the element components, respectively:

$$\frac{\gamma}{l^\alpha} \int_{\Gamma_\alpha} \delta \boldsymbol{u}\left(\mathbf{x}\right) d\Gamma \cdot \int_{\Gamma_\alpha} \mathbf{u}\left(\mathbf{x}\right) d\Gamma = \frac{\gamma}{l^\alpha} \sum_{e \in I^\alpha} \int_{\Gamma_\alpha^e} \delta \boldsymbol{u}\left(\mathbf{x}\right) d\Gamma \cdot \sum_{e \in I^\alpha} \int_{\Gamma_\alpha^e} \mathbf{u}\left(\mathbf{x}\right) d\Gamma \tag{2.38}$$

$$\frac{\gamma}{l^\alpha} \int_{\Gamma_\alpha} s\left(\mathbf{x}\right) \delta \boldsymbol{u} \cdot \mathbf{n}^\alpha d\Gamma \int_{\Gamma_\alpha} \frac{\mathbf{u} \cdot \mathbf{n}^\alpha}{s\left(\mathbf{x}\right)} d\Gamma = \frac{\gamma}{l^\alpha} \sum_{e \in I^\alpha} \int_{\Gamma_\alpha^e} s\left(\mathbf{x}\right) \delta \boldsymbol{u} \cdot \mathbf{n}^\alpha d\Gamma \sum_{e \in I^\alpha} \int_{\Gamma_\alpha^e} \frac{\mathbf{u} \cdot \mathbf{n}^\alpha}{s\left(\mathbf{x}\right)} d\Gamma \tag{2.39}$$

The elemental components of the above equations are expressed in the vector form as:

$$\int_{\Gamma_\alpha^e} \delta \boldsymbol{u} d\Gamma = (\mathbf{V}^e)^T \int_{\Gamma_\alpha^e} (\hat{\mathbf{N}}^e)^T d\Gamma = (\mathbf{V}^e)^T (\tilde{\mathbf{N}}^e)^T; \quad \int_{\Gamma_\alpha^e} \mathbf{u} d\Gamma = \tilde{\mathbf{N}}^e \mathbf{U}^e \tag{2.40}$$

$$\int_{\Gamma_\alpha^e} s \delta \boldsymbol{u} \cdot \mathbf{n}^\alpha d\Gamma = (\mathbf{V}^e)^T (\tilde{\mathbf{M}}_1^e)^T; \quad \int_{\Gamma_\alpha^e} \frac{\mathbf{u} \cdot \mathbf{n}^\alpha}{s\left(\mathbf{x}\right)} d\Gamma = \tilde{\mathbf{M}}_2^e \mathbf{U}^e \tag{2.41}$$

where,

$$\tilde{\mathbf{M}}_1^e = \int_{\Gamma_\alpha^e} s\left(\mathbf{x}\right) \hat{\mathbf{N}}^e\left(\mathbf{x}\right) \mathbf{n}^\alpha d\Gamma; \quad \tilde{\mathbf{M}}_2^e = \int_{\Gamma_\alpha^e} \frac{\hat{\mathbf{N}}^e\left(\mathbf{x}\right) \mathbf{n}^\alpha}{s\left(\mathbf{x}\right)} d\Gamma \tag{2.42}$$

The contributions of the second and third terms of the constraint equation to the global equation system is computed by assembling $\tilde{\mathbf{N}}^e$, $\tilde{\mathbf{M}}_1^e$ and $\tilde{\mathbf{M}}_2^e$. The contribution to the stiffness matrix is:

$$\hat{\mathbf{K}}_{c2}^\alpha = \frac{\gamma}{l^\alpha} \left[(\tilde{\mathbf{N}})^T \tilde{\mathbf{N}} + (\tilde{\mathbf{M}}_1)^T \tilde{\mathbf{M}}_2 \right] \tag{2.43}$$

in which, $\tilde{\mathbf{N}}$, $\tilde{\mathbf{M}}_1$ and $\tilde{\mathbf{M}}_2$ are assembled from the element counterparts through the standard assembly operations. The final system of equations to be evaluated for unknown nodal coefficients is:

$$\mathbf{K}\mathbf{U} = \mathbf{F}; \quad \mathbf{K} = \hat{\mathbf{K}} + \sum_{\alpha=1}^{n} \left[\hat{\mathbf{K}}_{c1}^\alpha - \hat{\mathbf{K}}_{c2}^\alpha \right] \tag{2.44}$$

2.4.3 Numerical integration

To be able to compute the linear system of Eq. 2.44, it is necessary to numerically compute the element level integrals for $\mathbf{K}^e$, $\mathbf{F}^e$, $\mathbf{K}_{c1}^{e\alpha}$, $\mathbf{K}_{c2}^{ei}$, $\tilde{\mathbf{N}}^{e\alpha}$, $\tilde{\mathbf{M}}_1^{e\alpha}$ and $\tilde{\mathbf{M}}_2^{e\alpha}$ as defined in the previous section. The integration rules employed in the standard finite element method is not sufficient since the higher order functions (i.e., enrichment functions) need to be integrated.

The domain is discretized using four different element types as illustrated in Fig 2.7: (1) Far field elements with no enrichment; (2) elements with partial enrichment; (3) fully enriched elements crossed by the fiber; and (4) fully enriched elements partially crossed by the fiber that contain the fiber tip. The treatment of the enrichment and the numerical integration differ for different element types. The enrichment domain in XFEM is typically chosen either based on the geometry or the discretization. The geometry-based approach considers full enrichment in all elements within a specified radius of the interface. The geometry based approach is particularly suitable for modeling of cracks, in which the stress fields around the crack tip, varies as a function of the distance from the tip. In this study, the enrichment domain is chosen based on the discretization since the enrichments functions

remain local.

1. Far field elements with no enrichment: Standard integration orders apply since no additional functions are employed in these elements.

2. Partially enriched elements: Integration rules with elevated order are employed since some of the nodes include enrichment functions.

3. Fully enriched elements entirely crossed by the fiber: The elements are split by the fiber. Each part is further decomposed into triangular sub-elements using Delaunay triangulation and higher order integration rules are used to capture high order enrichment fields within each sub-element.

4. Fully enriched elements that contain fiber tips: The elements are split along the normal direction at the fiber tip, as well as along the fiber direction. Each part formed by the split is further decomposed into triangular sub-elements using Delaunay triangulation and higher order integration rules are used to capture high order enrichment fields within each sub-element. The splitting based on the fiber normal ensures that the components of the enrichment function that pertain to the fiber tip and fiber level sets are integrated separately.

Typical integration schemes employed in fully enriched elements are shown in Fig. 2.7. In full enrichment cases, triangular sub-elements aligned with the fiber faces are used in the integration of a 2-D quadrilateral. The triangular sub-elements contain three integration points and use the standard Gauss quadrature rules. In the partially enriched elements and the far-field elements, Gauss quadrature rule with four integration points is performed [22]. The partially enriched elements do not have sub elements since the fiber does not cross through the element.

The line integration of the α^{th} constraint equation is performed on the domain of the α^{th} fiber based on the Gauss quadrature. The rule employed in the integration of the constraint

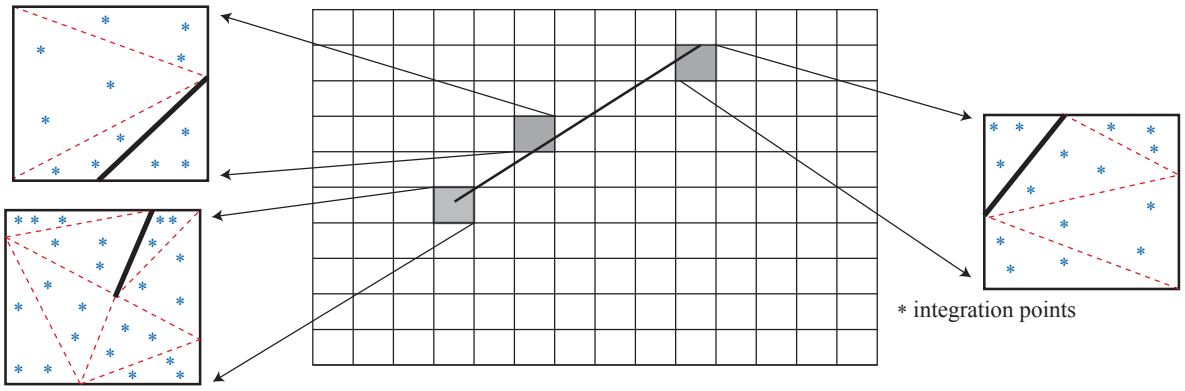

Figure 2.7: The schematic illustration of Delaunay triangulation and integration of fully enriched elements based on fiber tip positioning.

equation has a significant influence on the accuracy characteristics of the model, similar to the sensitivity of accuracy with respect to the integration of the enrichment functions, reported previously (e.g., [16]). The number of integration points along the fiber (n_g^α) is determined using a heuristic formula, as a function of the fiber length (l^α) and the mesh density (h) given as:

$$n_g^\alpha = \lfloor\lfloor \frac{1.3 l^\alpha}{h} \rceil\rceil_{\mathrm{e}} \tag{2.45}$$

where, $\lfloor\lfloor \cdot \rceil\rceil_{\mathrm{e}}$ indicates approximation to the nearest even integer. Only even number of integration points are used to ensure that the no gauss point lies on the fiber center, since this causes the rotation constraint (i.e., Eq. 2.39) to tend to infinity. When more than 12 integration points are needed in the constraint equation, the domain of integration is split and the integration is performed separately for each split part such that the quadrature formulas per split fiber part does not exceed 12 integration points. If a fiber crosses an element for a very small fraction of the fiber length, it is possible to have no integration points within the element despite the presence of the fiber within the element.

2.4.4 Treatment of partially enriched elements

It has been previously shown that the treatment of the partially enriched elements has an effect on the accuracy and convergence of XFEM models [41]. This is because within

partially enriched elements (a) the partition of unity property no longer holds and (b) the affine transformations (e.g. constant strain modes) cannot be represented exactly. A number of solution strategies exist to alleviate these problems (e.g. [23, 59]). One method involves the modification of the enrichment using a ramp function that has a local support within the partially enriched element and enriching all nodes of the partially enriched element using the modified enrichment function [41]. In the current study a similar modification of the enrichment function is considered. Let $\hat{\psi}(\mathbf{x})$ denote the modified enrichment function within a partially enriched finite element:

$$\hat{\psi}(\mathbf{x}) = \sum_{b \in \mathcal{I}_e} N_b(\mathbf{x}) \psi(\mathbf{x}); \quad \mathbf{x} \in \Omega_e \tag{2.46}$$

where, $\mathcal{I}_e$ are the nodes in the partially enriched element, Ω_e, that are connected to fully enriched elements. The modified enrichment function is active at all nodes of the partially enriched element:

$$\mathbf{u}^e(\mathbf{x}) = \sum_{a=1}^{n_n^e} N_a^e(\mathbf{x}) \hat{\mathbf{u}}_a^e + \sum_{b=1}^{n_n^e} N_b^e(\mathbf{x}) \hat{\psi}(\mathbf{x}) \hat{\mathbf{c}}_b^e \tag{2.47}$$

in which, superscript e indicates that all pertinent variables are defined in the partially enriched element, e. The modifications needed in the finite element implementation discussed above is to use the modified enrichment functions (instead of the enrichment functions) and considering enrichment of all nodes within the partially enriched elements.

2.5 Numerical Examples

In this section, two numerical examples demonstrate the performance of the XFEM model in evaluating the response of short fiber reinforced composites in a two-dimensional setting. The first example illustrates the accuracy characteristics of the method using a single fiber inclusion embedded in a matrix, whereas the second example considers multiple random short fibers embedded in a matrix.

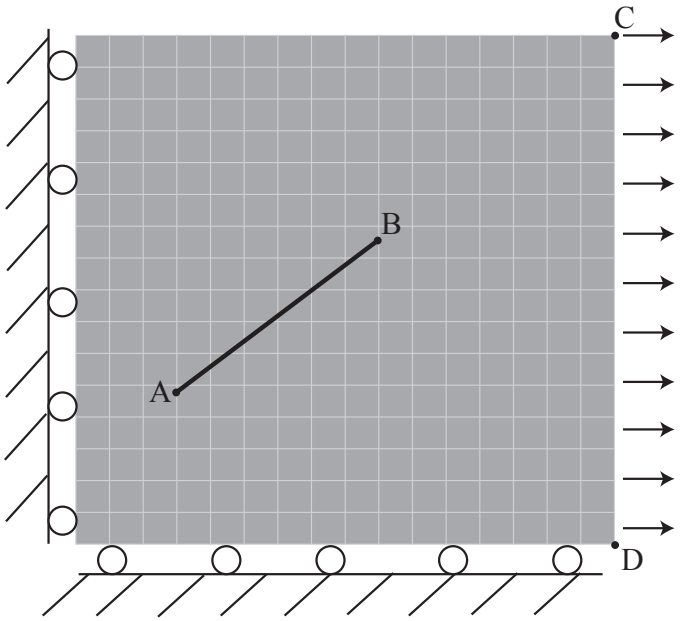

Figure 2.8: The geometry and boundary conditions of the single inclusion problem.

2.5.1 Single fiber inclusion

The XFEM formulation is verified against the standard finite element method using a composite enriched with a single fiber. The schematic representation of the model problem is shown in Fig. 2.8. The size of the domain is 5 mm by 5 mm and the fiber size is approximately 1mm. The domain is subjected to uniform uniaxial tensile loading applied at the right edge. The fiber is placed such that a non-uniform deformation and stress distribution is achieved within the matrix. The Young's Modulus and Poisson's ratio of the matrix material are 14 GPa and 0.3, respectively. The reference model consists of a very densely meshed finite element model in which the fiber is enforced to undergo rigid body motion. The rigid fiber motion in the reference model is prescribed by constraining nodal degrees of freedom that lay along the fiber domain using the multi point constraint method. Similar to the XFEM approach, the fiber is idealized as a line segment. Reference simulation discretizations ranging from 400 elements up to approximately 62,500 elements have been studied to ensure mesh convergence. The simulations confirmed that the response is very accurately captured at such high levels of discretization. All reported reference simulation results are

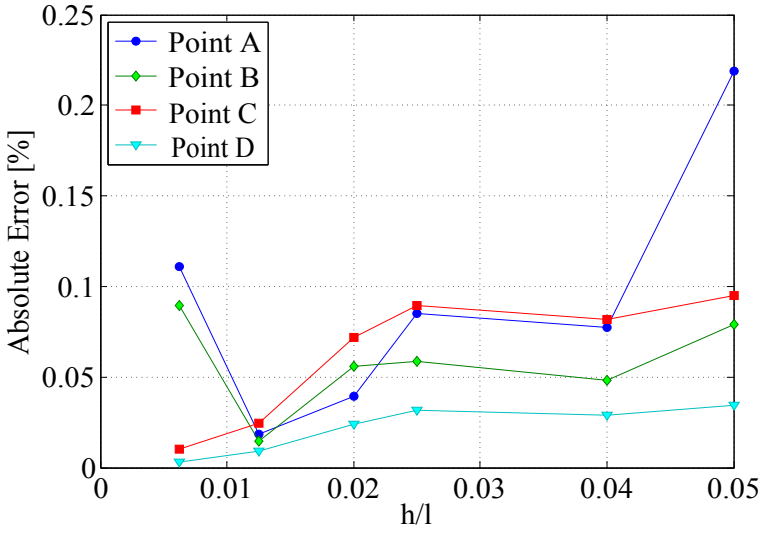

Figure 2.9: Error as a function of normalized mesh density when fiber tips are at mesh nodes.

based on approximately 625,000 element discretizations.

Figure 2.9 shows the accuracy of the XFEM model compared to the reference simulation. The accuracy is assessed at four different locations as illustrated in Fig. 2.8. Points A, B, C, D refer to the left fiber tip, right fiber tip, top right corner and bottom right corner within the problem domain, respectively. In Fig. 2.9, the point-wise errors are computed using the L2 norm and plotted against the normalized mesh density (h/l). The reference simulation considers a very fine and nonuniform grid (to conform to the fiber domain). The discretization of the XFEM model is a square and uniform grid. In these simulations, the fiber tip locations for all element sizes always coincide with a node. The error for the corner nodes reduces monotonically with increasing mesh density. Errors at the fiber tips displayed slight variations in accuracy as a function of mesh density. While the trend is not monotonic for fiber tips, the error for all four points probed remained within very reasonable accuracy (i.e., 0.25%). The numerical studies indicated that the sensitivity to the numerical integration of the constraint equation is the main factor leading to non-monotonic convergence. The integration rule selection formula introduced in Section 2.4.3 leads to highly accurate results,

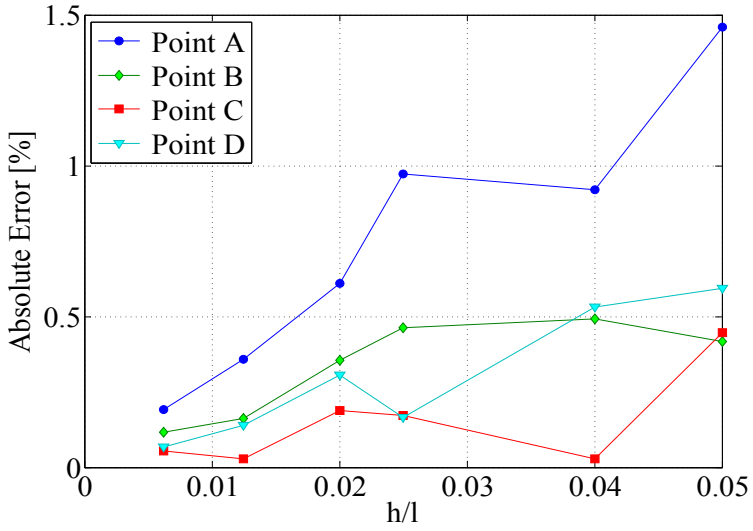

Figure 2.10: Error as a function of normalized mesh density when fiber tips in elements.

yet with some variation from monotonic convergence in some cases. The demonstrated errors are point-wise in contrast to the more traditional error characterization where the errors over the entire problem domain is averaged. It should be noted that the highest errors within the model typically occurs at the fiber tips, which are directly reported in Fig. 2.9.

The effect of fiber tip location on the local accuracy characteristics of the XFEM method was also investigated. Figures 2.10 and 2.11 illustrate the accuracy characteristics of the XFEM model for cases in which the fiber tips lay within the elements or on element edges, respectively. In both cases it is observed that the XFEM models display reasonable accuracy and follows the same trend as when fiber tips are on the nodes with a slightly higher errors. The accuracy of the model is higher when the fiber tip resides on the edges rather than within the element. The slight deviation from monotonic mesh convergence is attributed to the fact that the relative positions of the fiber tip for each mesh density is different leading to slightly different accuracy of the numerical integrations. For instance, if the fiber tip is too close to a node location, the sub elements formed in the Delaunay triangulation for numerical integration of the fully and partially enriched elements have very high aspect ratios. In

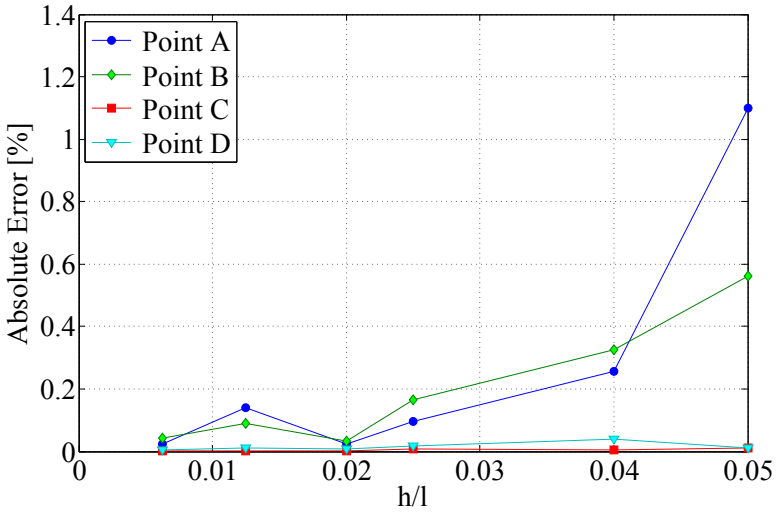

Figure 2.11: Error as a function of normalized mesh density when fiber tips are on element edges.

all cases the accuracy of the XFEM model is in reasonable agreement with the reference finite element model. The point-wise comparison of the performance of XFEM models as a function of fiber tip location is summarized in Table 2.1 for three normalized mesh densities.

The XFEM method is known to exhibit sensitivity to the position of the enrichment functions with respect to the finite element mesh. The position sensitivity in the context of the present problem is investigated by considering the response of a fiber with fixed orientation and length that is swept across the problem domain. The accuracy of the model

Table 2.1: Point wise absolute error comparison.

Location	Point A			Point B		
h/l	0.05	0.025	0.0125	0.05	0.025	0.0125
Tips at nodes	0.219%	0.085%	0.018%	0.079%	0.058%	0.015%
Tips at edges	1.099%	0.096%	0.140%	0.563%	0.165%	0.089%
Tips in element	1.459%	0.972%	0.358%	0.417%	0.463%	0.162%
Location	Point C			Point D		
h/l	0.05	0.025	0.0125	0.05	0.025	0.0125
Tips at nodes	0.095%	0.090%	0.025%	0.034%	0.032%	0.009%
Tips at edges	0.011%	0.006%	0.002%	0.010%	0.018%	0.012%
Tips in element	0.447%	0.172%	0.029%	0.592%	0.164%	0.140%

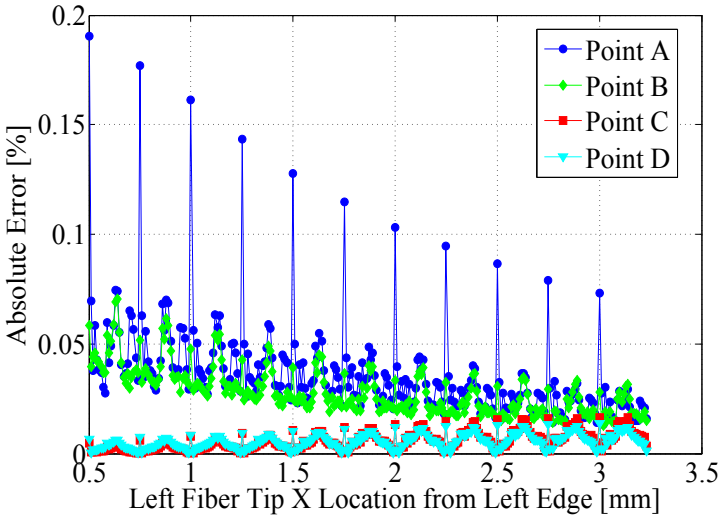

Figure 2.12: Error as a function of tip location across domain.

predictions is quantified as a function of the fiber relative position within the mesh. The angle and length of the fiber is 61° to the horizontal and 1 mm, respectively. The sweep starts with the left fiber tip starting at 0.5 mm from the left edge and ends at 3.25 mm from the left edge of the domain. Simulations were conducted for each fiber position with a resolution of 0.1 mm. The errors at points C and D corresponding the bottom left and right corners of the domain remain consistently below 0.02%. The errors at the fiber tips tended to decrease slightly as it moved across the domain but clearly demonstrate the position sensitivity of the accuracy as illustrated in Fig. 2.12. The errors oscillate since the relative position of the fiber with respect the elements in the regular grid repeats as the fiber is moved an amount equal to the element size. The largest errors occur when the tips of the fibers are positioned at the center of an element. Figure 2.12 shows the absolute errors at the four points studied across the domain.

2.5.2 Random short fiber composite

In this section, the response of two-dimensional random short fiber composites is investigated. The matrix is taken to be portland cement with the elastic modulus of 14 GPa, Poisson's

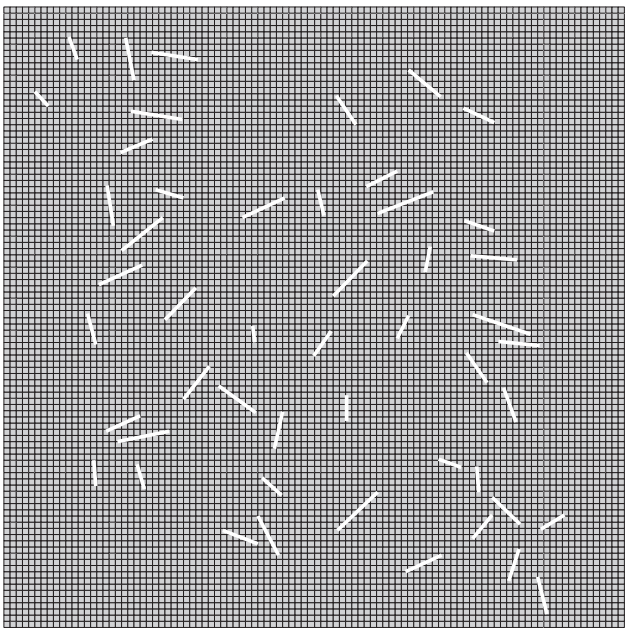

Figure 2.13: Random short fiber domain.

ratio of 0.3 and a domain of 100 mm by 100 mm. The cement matrix is reinforced in a planar fashion using carbon microfibers. The elastic moduli, length and diameter of the microfibers are 207 GPa, 7 mm ($\pm$ 1 mm) and 7 μm, respectively.

A set of volume elements with specified weight fractions of up to 0.15% are generated and subjected to uniform uniaxial stress to determine the effective properties of the composite material as a function of fiber weight fraction. The microstructures are generated to ensure that no element within the mesh is crossed by more than a single fiber. Figure 2.13 shows an example of the random short fibers in a domain. At each of the 6 different weight fractions studied, 20 microstructures are generated to characterize the variability of the effective modulus as a function of the fiber distribution properties. The variability of the effective modulus is due to two distinct factors: (a) the natural variability due to the random positioning of the fibers within the matrix in each realization; and (b) the effect of overall volume element size (i.e., statistical representativeness of the volume element). The effect of the second factor is minimized by choosing large enough representative volumes.

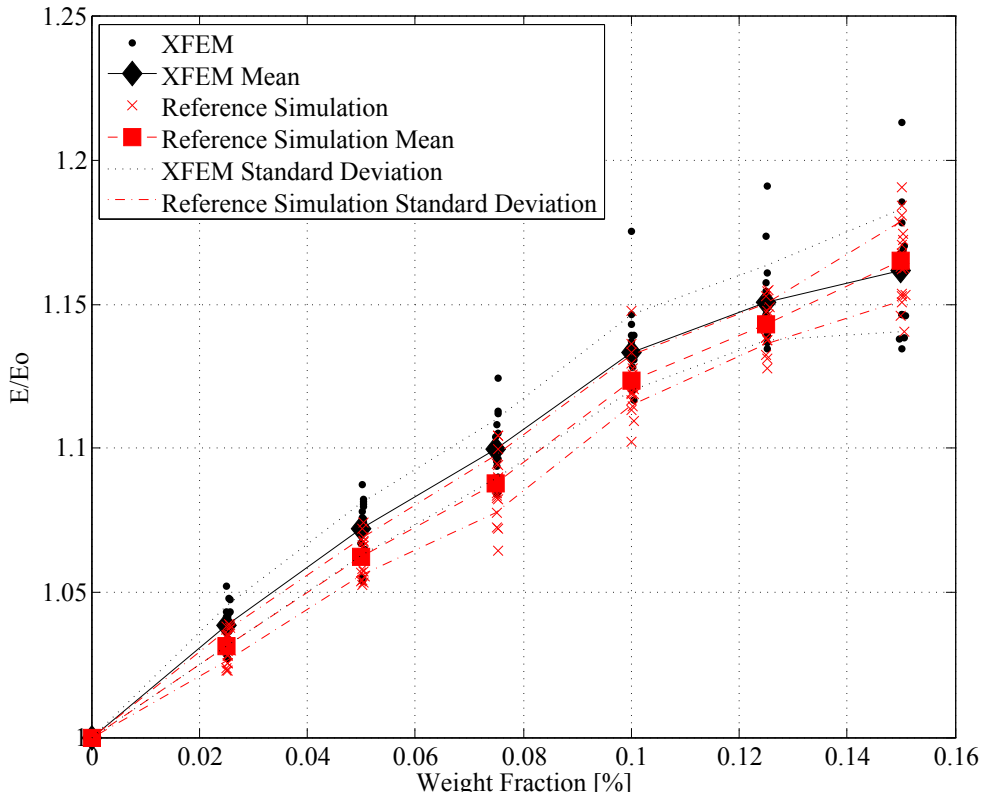

Figure 2.14: Elastic modulus ratio of random short fibers.

This size of the volumes are determined as the smallest matrix volume beyond which the modulus variability does not significantly change. For a given weight fraction, preliminary simulations using different volume sizes were conducted. The modulus variability was found to be higher when the volume size is smaller. Beyond a threshold size, the variability of the modulus stabilizes. Similar simulations conducted at varying weight fractions showed that the threshold size for large weight fractions is bigger compared to small weight fractions. The representative volume size is therefore larger at higher fiber weight fractions.

Figure 2.14 illustrates the XFEM response of the random short fiber composite compared to the direct finite element method simulations performed with the commercial software package, Abaqus. The Young's modulus of the random short fiber composite is plotted as a ratio with the initial Young's modulus. At each weight fraction, 20 randomly generated microstructures are simulated using both the XFEM and the reference models. The results of the XFEM and the reference simulations are plotted including the mean value and standard

deviation for each method. The elastic modulus tended to initially increase almost linearly and then started to level out with the increase of weight fraction. The XFEM results had variation due to the randomness of the fibers in the domain but were within 2% of the mean reference simulation results, which was slightly below the mean of the XFEM results for each weight fraction.

CHAPTER 3

XFEM MODELING OF SHORT FIBER REINFORCED COMPOSITES WITH COHESIVE INTERFACES

3.1 Introduction

The previous chapter discussed random rigid short fiber reinforced composites with the use of XFEM. Those ideas can be built upon to incorporate realistic ideas for XFEM with short fibers. More realistic assumptions can be made for the analysis of the composites, such as deformable fibers, damage in the domain of the matrix and fiber-matrix debonding characteristics. The work in this chapter is reflected in Ref. [87], and presented with the permission of Elsevier.

This chapter introduces a failure model for random short fiber reinforced composite materials based on the XFEM in a 2-D setting. Elastic and deformable microfiber inclusions modeled as objects with zero measure are incorporated into the XFEM framework. A debonding enrichment function is developed to idealize the progressive debonding between the fiber-matrix interfaces. The fiber deformation is approximated as axial and directly incorporated into the Lagrangian. With extension to 3-D in mind, the progressive failure within the matrix material is idealized using an integral-type nonlocal damage model [85]. The performance of the XFEM model is assessed by comparing model predictions to the direct finite element method for various fiber configurations. The numerical verification studies point to high accuracy characteristics of the approach. The computational efficiency of the approach provides the capability to evaluate the failure response of microstructures that include a large number of short fiber inclusions.

The remainder of this chapter is organized as follows. In Section 3.2, the enrichment functions employed to model the presence of the inclusions and the debonding process are introduced. Section 3.3 provides the governing equations and the model formulation. The

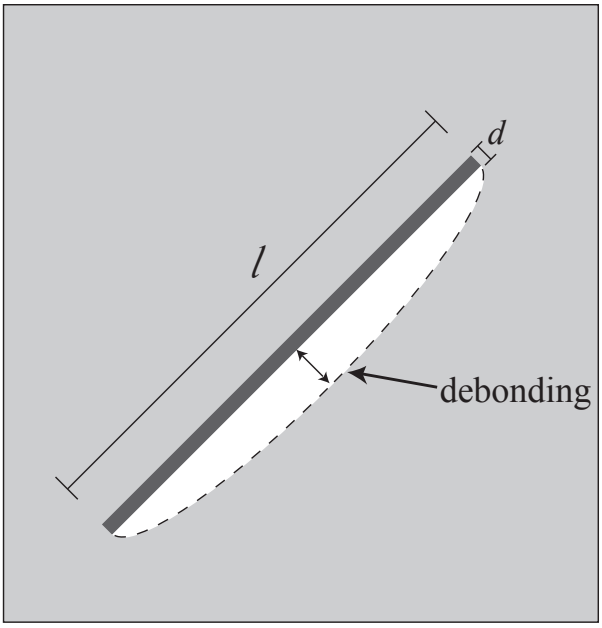

Figure 3.1: Fiber representation in the domain with the white area representing the debonding between the fiber and the matrix.

computational formulation is discussed in Section 3.4, including the formulation of fiber deformation, formulation of cohesive tractions, numerical integration and the treatment of partially enriched elements. Numerical verification studies to assess the performance of the proposed approach are presented in Section 3.5.

3.2 XFEM for Short Fiber Reinforced Composites with Cohesive Interfaces

To model short fiber reinforced composites for fibers with very high aspect ratios ($d/l << 1$) that are able to debond from the matrix, as illustrated in Fig. 3.1 is investigated. The XFEM approach (Section 2.2) is employed not only to describe the presence of the fiber inclusions, but also to idealize the fiber-matrix debonding process.

The following discretization (based on Eq. 2.1) of the displacement field for a domain reinforced by short fiber inclusions which includes fiber inclusions and progressive debonding between the fiber and the matrix is considered:

$$\mathbf{u}(\mathbf{x},t) = \sum_{a=1}^{n_n} N_a(\mathbf{x})\hat{\mathbf{u}}_a + \sum_{b=1}^{n_{\text{en}}} N_{\mathcal{I}_b}(\mathbf{x})\psi(\mathbf{x})\hat{\mathbf{c}}_b + \sum_{c=1}^{n_{\text{en}}} N_{\mathcal{I}_c}(\mathbf{x})\Upsilon(\mathbf{x})\hat{\mathbf{d}}_c \tag{3.1}$$

where, $\mathbf{u}$ denotes the displacement field; $\mathbf{x}$ and t are the space and time coordinates, respectively, N_a, the standard finite element shape function associated with node a; $\hat{\mathbf{u}}_a$, $\hat{\mathbf{c}}_b$ and $\hat{\mathbf{d}}_c$ the nodal coefficients of the standard, fiber enrichment and debonding enrichments, respectively; n_n the total number of mesh nodes in the finite element discretization; n_{en} the number of enriched nodes; $\mathcal{I}$ index set of enriched nodes; $\mathcal{I}_a \in \mathcal{I}$ the index of an enriched node, a; ψ the fiber enrichment function; and Υ denotes the debonding enrichment function.

In Eq. 3.1, the first right hand side term corresponds to the standard finite element approximation of the response field. The enrichment, ψ, that accounts for the presence of the fiber within the domain, represents the strain discontinuity in the approximation space. The fiber enrichment function, ψ, is the same as outlined in Section 2.3.1. The third term on the right hand side is the enrichment to approximate the displacement jump due to the progressive loss of the cohesive bond between the fiber and the matrix, and is a function of the debonding enrichment function, Υ.

3.2.1 Debonding enrichment function

Similar to the fiber enrichment function, the debonding enrichment function Υ, is defined using the fiber domain and tip level set functions as shown in Fig. 3.2. In contrast to the fiber enrichment, the debonding enrichment function introduces a discontinuity in the displacement field.

The shape of the debonding enrichment function is governed by the discontinuity function, ϕ_p, which mimics the shape of the fiber-matrix debonding. ϕ_p is taken to be a fourth order polynomial:

$$\phi_p(\mathbf{x}) = \sum_{k=0}^{4} a_k s(\mathbf{x})^k \tag{3.2}$$

The following constraints are considered in the determination of the constants of the polynomial expression: (1) The ends of the fiber are taken to remain fully attached to the matrix (i.e., $\phi_p\,(s = \pm 1) = 0$); (2) Maximum debonding occurs at the center of the fiber (i.e., $d\phi_p/ds\,(s = 0) = 0$); and (3) The function is normalized such that the maximum value is

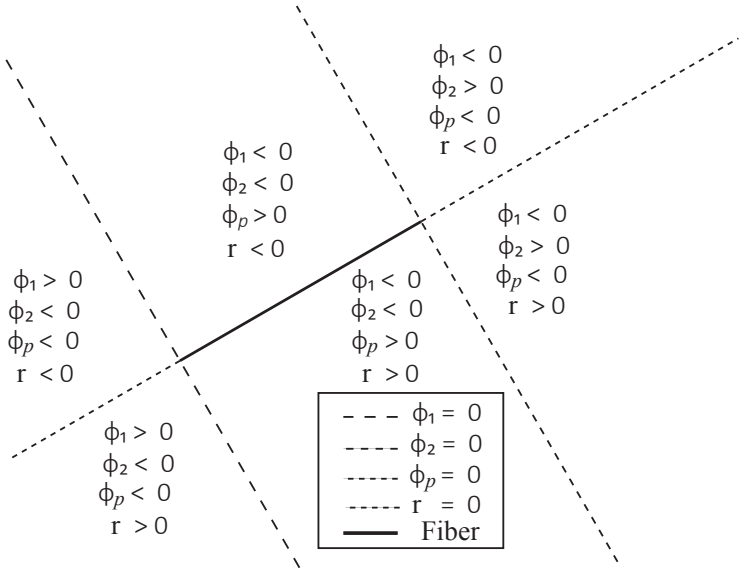

Figure 3.2: Functions of the fiber enrichment and debonding enrichment.

unity at the center of the fiber (i.e., $\phi_p\,(s=0)=1$). Considering the constraints above, the discontinuity function is expressed as a function of a single shape parameter, θ_d as:

$$\phi_p(\mathbf{x}) = 1 + \frac{\tan\theta_d}{2} s(\mathbf{x})^2\left(1 - s(\mathbf{x})^2\right) - s(\mathbf{x})^2\left(2 - s(\mathbf{x})^2\right) \tag{3.3}$$

where, θ_d is the slope of the discontinuity at the tips of the fiber, controlling the shape of the discontinuity function:

$$\theta_d = \tan^{-1}\left(\left.\frac{d\phi_p}{ds}\right|_{s=-1}\right) \tag{3.4}$$

Figure 3.3a illustrates the effect of θ_d on the shape of the discontinuity function ϕ_p. When θ_d is less than a threshold value (i.e., $\theta_{d\text{th}}$) the discontinuity curve displays inflection points, which occur along the length of the fiber at positions that depend on the value of θ_d. Above the threshold value, the discontinuity curve is convex. The threshold value for the chosen function form (Eq. 3.3) is $\theta_{d\text{th}} = 58°$. In the numerical verification studies provided in this manuscript, the shape parameter is set to $\theta_d = 81°$. The shape parameter is chosen based on observations from numerous evaluations of direct finite element simulations of a short fiber inclusion subjected to remote tensile stress. This enrichment is employed to capture

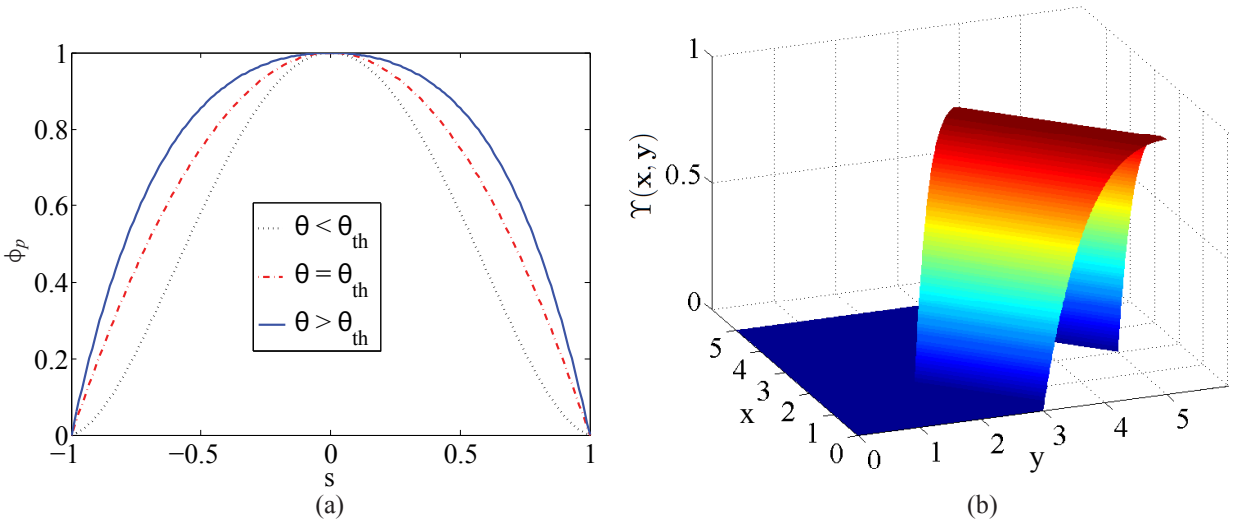

Figure 3.3: (a) ϕ_p as a function of s, for θ_d above, at and below the θ_{dth} value; and (b) short fiber inclusion debonding enrichment function.

debonding along both normal and tangential directions. Interfacial damage in directions normal and tangential to fibers has been observed experimentally in fiber reinforced concrete composites [80]. In the presence of multiple nearby fibers, which may lead to complex traction patterns along the fiber-matrix interface. In case of a single fiber, the deviation from symmetry is typically slight. The parabolic and symmetric enrichment function used in the context of XFEM have the ability to capture asymmetric and complex debonding patterns as demonstrated later on in this work. This is because of multiple enriched degrees of freedom used in approximating the debonding of a single fiber (Eq. 3.1, third term on right hand side).

The debonding enrichment function for the fiber is then expressed in terms of the discontinuity functions, $\phi_\lambda(\mathbf{x})$ and $\phi_c(\mathbf{x})$ as:

$$\Upsilon(\mathbf{x}) = \phi_p \, H(r(\phi_c)) \left(\prod_{\lambda=1}^{2} H(-\phi_\lambda) \right) \tag{3.5}$$

where $r = \pm\phi_c$ is the signed distance function as schematically illustrated in Fig. 3.2. A three dimensional visualization of the debonding enrichment function is shown in Fig. 3.3b.

3.3 Governing Equations and Model Formulation

The mechanical equilibrium within the domain is expressed in Section 2.4 in Eq. 2.10 and Eq. 2.11. The exterior boundary conditions are stated in Eq. 2.12 and Eq. 2.13. Since all fibers are embedded in the matrix, the displacement and traction boundaries of the problem domain, Ω, coincide with those of Ω_m.

The traction continuity across the fiber-matrix interface is given as:

$$[\![\boldsymbol{T}]\!] = [\![\boldsymbol{\sigma} \cdot \boldsymbol{n}]\!] = 0 \quad \mathbf{x} \in \Gamma_\alpha \equiv \partial\Omega_m \cap \partial\Omega_\alpha \quad \forall\alpha \tag{3.6}$$

in which, the traction $\boldsymbol{T}$, is a function of the normal and tangential tractions ($\boldsymbol{T} = \boldsymbol{T}(T_n, T_t)$; $\boldsymbol{n}$ the outward unit vector to a boundary; and $[\![\cdot]\!]$ the jump operator. The domains of fiber α and the matrix are denoted as Ω_α and Ω_m, respectively. All fibers are taken to be fully embedded in the matrix with no intersection with exterior boundaries or with each other (i.e., $\Omega = \Omega_m \cup \bigcup_{\alpha=1}^{n} \Omega_\alpha$). The interface of the fiber α with the matrix is denoted as Γ_α. Tensor notation is employed in the formulation of the governing equations.

The matrix is taken to progressively damage under applied mechanical loading, which is idealized using the continuum damage mechanics approach:

$$\boldsymbol{\sigma} = (1 - w(\mathbf{x}, t))\mathbf{L} : \boldsymbol{\epsilon}\,(\mathbf{x}, t) \tag{3.7}$$

in which, $\boldsymbol{\epsilon}$ denotes the strain tensor; and $w \in [0, 1)$ a scalar damage variable. $\omega = 0$ and $\omega = 1$ respectively denote the fully undamaged state and the complete loss of load carrying capacity at the material point. The focus is on the quasi-brittle behavior and therefore small strain theory is employed. The strain is taken to be the symmetric gradient of the displacement field ($\boldsymbol{\epsilon} = \nabla^s \mathbf{u}$). All fibers are assumed to remain elastic under the applied loading.

In a two dimensional domain, consider a matrix reinforced by n straight fibers, with

length and the thickness of a fiber, α, denoted as l_α and t_α, respectively, at an angle, θ_α from the horizontal ($\alpha = 1, 2, \ldots, n$), where the fibers are randomly distributed within the domain. The fiber aspect ratios are vanishingly small (i.e., $t_\alpha / l_\alpha \ll 1$). Under this condition, the fiber domain is represented as sets of zero measure (i.e., line segments) and XFEM is employed to evaluate the governing equations. Using the standard procedure, the weak form of Eqs. 2.10-2.13 and Eq. 3.6 is expressed as follows:

$$\int_{\Omega_m} \boldsymbol{\sigma} : \delta\boldsymbol{\epsilon}\, d\Omega + \sum_{\alpha=1}^{n} \int_{\Omega_\alpha} \boldsymbol{\sigma} : \delta\boldsymbol{\epsilon}\, d\Omega + \sum_{\alpha=1}^{n} \int_{\Gamma_\alpha} \boldsymbol{T} \cdot \delta[\![\mathbf{u}]\!]\, d\Gamma - \int_{\Gamma_t} \tilde{\mathbf{t}} \cdot \delta\mathbf{u}\, d\Gamma = 0 \tag{3.8}$$

The stress that develops in the fiber is axial, due to the assumption that high aspect ratio fibers that are embedded in the domain are assumed to have uniform tractions along the fiber. This assumption is verified using direct finite element simulations where the fiber is resolved with highly resolved meshes. No significant shear stress or bending moment develops within the domain of the fiber.

The axial stress that develops in the fiber is expressed as:

$$\boldsymbol{\sigma} = \sigma_f^\alpha(s) \boldsymbol{t}_\alpha \otimes \boldsymbol{t}_\alpha \tag{3.9}$$

The second term in Eq. 3.8 then becomes:

$$\int_{\Omega_\alpha} \boldsymbol{\sigma} : \delta\boldsymbol{\epsilon}\, d\Omega \;\simeq\; t_\alpha \int_{\Omega_\alpha} \sigma_f^\alpha \delta\epsilon_f^\alpha\, d\Omega \tag{3.10}$$

in which, $\delta\epsilon_f^\alpha = \delta\boldsymbol{\epsilon} : \boldsymbol{t}_\alpha \otimes \boldsymbol{t}_\alpha$. The axial stress in fiber α, is taken to be proportional to the axial strain (i.e., $\sigma_f^\alpha = E_f \epsilon_f^\alpha$), where E_f is the elastic modulus of the fiber. Upon complete debonding between the fiber and the matrix, bending of the fiber may also develop. This deformation mode is not accounted for in the current chapter.

The traction continuity (i.e., Eq. 3.6) is weakly enforced, but the displacement field can develop discontinuity allowing the incorporation of progressive debonding between the fiber

and the matrix.

Consider the local parameterization of the fiber domain, Ω_α, using the fiber normal and tangent vectors, $\boldsymbol{n}_\alpha$ and $\boldsymbol{t}_\alpha$, respectively. Since fibers are straight, the normal and tangent vectors are constant for each fiber. Under the condition that aspect ratios of the fibers are very high, assume that tractions along the two opposing faces in the thickness direction are uniform:

$$\boldsymbol{T}^+(s)\cdot\boldsymbol{n}^+\Big|_{\Gamma_\alpha^+} - \boldsymbol{T}^-(s)\cdot\boldsymbol{n}^-\Big|_{\Gamma_\alpha^-} = 0; \quad \boldsymbol{T}^+(s)\cdot\boldsymbol{t}^+\Big|_{\Gamma_\alpha^+} - \boldsymbol{T}^-(s)\cdot\boldsymbol{t}^-\Big|_{\Gamma_\alpha^-} = 0 \tag{3.11}$$

The progressive debonding process between the fiber and the matrix is modeled through the third term in Eq. 3.8. A simplification of the debonding process from the fiber to facilitate expression of progressive debonding using the enrichment function given in Eq. 3.5 is employed. For a short fiber embedded in a matrix under the traction conditions considered in Eq. 3.11, the debonding along the two faces of the fiber would occur simultaneously. In reality, the debonding is likely to initiate at a weak spot on one side of the fiber. Upon complete debonding at the weak side, the tractions along the opposing (unbonded) side relax. Further assumptions include that the tips of the fiber remain attached to the matrix. The internal boundary term then reduces to:

$$\int_{\Gamma_\alpha} \boldsymbol{T}\cdot\delta[\![\mathbf{u}]\!]\,d\Gamma = \int_{\Gamma_\alpha^+} \boldsymbol{T}\cdot\delta[\![\mathbf{u}]\!]\,d\Gamma \tag{3.12}$$

In the limit, where fiber aspect ratios tend to infinity, the weak form of the governing equations is expressed as:

$$\int_\Omega \boldsymbol{\sigma} : \delta\boldsymbol{\epsilon}\,d\Omega + \sum_{\alpha=1}^{n} t_\alpha E_f \int_{\Omega_\alpha} \epsilon_f^\alpha \delta\epsilon_f^\alpha\,d\Omega + \sum_{\alpha=1}^{n}\int_{\Gamma_\alpha} \boldsymbol{T}\cdot\delta[\![\mathbf{u}]\!]\,d\Gamma - \int_{\Gamma_t} \tilde{\mathbf{t}}\cdot\delta\mathbf{u}\,d\Gamma = 0 \tag{3.13}$$

Since the domains of the fibers tend to a zero measure set, the domain of the matrix is taken to occupy the entire domain and the limits of the integral of the first term in Eq. 3.8 is set

to Ω.

3.3.1 Nonlocal damage model

The progressive damage and cracking within the matrix is modeled using continuum damage mechanics. It is also possible to model crack propagation using XFEM, particularly in the presence of pre-cracks. Other approaches that adaptively enrich the problem domain with cracks based on prescribed failure criteria have also been proposed (e.g. [96, 102, 103, 107]). One motivation in employing the continuum damage mechanics approach is that it can be extended to 3-D in a straightforward manner.

The basis of the continuum damage mechanics model is the idea of progressively degrading material until fracture, where the material no longer can carry load. The damage parameter w, characterizes the evolution of the secant moduli tensor of the material during the degradation process. The continuum damage mechanics model employed in this chapter is regularized to eliminate the well known issues of spurious strain localization and mesh dependency. A number of approaches exist to eliminate the mesh dependency problem including nonlocal modeling of gradient and integral type, viscous regularization, crack band method, variational multiscale method and others (e.g. [7, 27, 29, 37, 45, 46, 56, 58, 105]). In this study, the nonlocal regularization of integral type is employed.

At an arbitrary material point $\hat{\mathbf{x}}$, the state of damage follows a smooth function, g:

$$w(\hat{\mathbf{x}}, t) = g(k(\hat{\mathbf{x}}, t)) \tag{3.14}$$

in which, $g(k)$ is taken to follow an arctangent law [39] as a function of a history dependent parameter, k as:

$$g(k) = \frac{\arctan(a\ k(\hat{\mathbf{x}}, t) - b) + \arctan(b)}{\frac{\pi}{2} + \arctan(b)} \tag{3.15}$$

where, a and b are parameters that characterize the evolution of damage and control ductility and strength. k indicates the maximum past value of the nonlocal damage equivalent strain,

$\hat{v}$:

$$k(\hat{\mathbf{x}}, t) = \max_{\tau \in [0,t]} \left(\langle \hat{v}(\hat{\mathbf{x}}, \tau) - v_{\text{ini}} \rangle \right) \tag{3.16}$$

in which, v_{ini} is the threshold value of $\hat{v}$, below which damage does not progress; and $\langle \cdot \rangle = ((\cdot) + |\cdot|)/2$ the Macaulay brackets. The nonlocal damage equivalent strain is expressed as a function of the local damage equivalent strain, v, using the following equation:

$$\hat{v}(\hat{\mathbf{x}}) = \frac{\int_{\Omega} \lambda_w(\mathbf{x}, \hat{\mathbf{x}}) v(\mathbf{x}, t) d\mathbf{x}}{\int_{\Omega} \lambda_w(\mathbf{x}, \hat{\mathbf{x}}) d\mathbf{x}} \tag{3.17}$$

The local equivalent strain is taken as a function of the principle strains as proposed by Prisco and Mazars [90]:

$$v(\hat{\mathbf{x}}, t) = \sqrt{\sum_{I=1}^{2} \langle \epsilon_I(\hat{\mathbf{x}}, t) \rangle^2} \tag{3.18}$$

where ϵ_I are the principle strains. The Macaulay brackets incorporate the tension-compression anisotropy. Under compressive strain, the damage is not allowed to grow. In this chapter, the verification studies focus only on the tension failure. The nonlocal weighting of the damage equivalent strain, λ_w is expressed using the Wendland Radial Basis Function [111]:

$$\lambda(\mathbf{x}, \hat{\mathbf{x}}) = \begin{cases} \left(1 - \frac{\|\mathbf{x} - \hat{\mathbf{x}}\|}{l_c}\right)^4 \left(4 \frac{\|\mathbf{x} - \hat{\mathbf{x}}\|}{l_c} + 1\right) & \|\mathbf{x} - \hat{\mathbf{x}}\| \leq l_c \\ 0 & \|\mathbf{x} - \hat{\mathbf{x}}\| > l_c \end{cases} \tag{3.19}$$

in which, l_c denotes the characteristic length defining the span of the radial basis.

In the context of fibrous composites, the domains of the fiber, whether modeled as zero measure or not, potentially constitute a boundary in the application of the nonlocal weighting. In the present study, the nonlocal averaging is applied without considering the fiber domains as boundaries. In all verification studies considered below, similar strategy is employed in the reference simulations as well.

3.3.2 Cohesive law

The progressive debonding between the fiber and the matrix is modeled by prescribing cohesive zone laws. In the numerical verification and studies included in this chapter, exponential and bilinear cohesive laws are considered. The cohesive law at the interface describes the relationship between the surface traction and material separation between the surfaces, representing the physical deterioration occurring at the interface. The proposed computational approach differs considerably from traditional cohesive zone modeling, which entails incorporation of cohesive elements between standard finite elements. Since the positions of the fibers do not necessarily comply with the underlying domain discretization, the proposed approach does not include cohesive elements.

The debonding enrichment function is taken to have a parabolic shape along the fiber as described in Eq. 3.3. The actual debonding may deviate from the parabolic shape since multiple degrees of freedom are employed to discretize the fiber-matrix debonding (i.e., Eq. 3.1).

The exponential cohesive law employed in this chapter is derived from an interface potential as proposed by Xu and Needleman [115]. The interface tractions are expressed as:

$$\boldsymbol{T} = \frac{\partial \Phi\left(\llbracket \mathbf{u} \rrbracket\right)}{\partial \llbracket \mathbf{u} \rrbracket} \tag{3.20}$$

in which, the interface potential, Φ is a function of displacement jumps normal and tangential to the fiber directions [114]:

$$\Phi(\llbracket \mathbf{u} \rrbracket) = \Phi_n + \Phi_n \exp(-\frac{\llbracket \mathrm{u}_n \rrbracket}{d_n}) \left\{ \left[1 - y + \frac{\llbracket \mathrm{u}_n \rrbracket}{d_n} \right] \frac{1-q}{y-1} - \left[q + \frac{y-q}{y-1} \frac{\llbracket \mathrm{u}_n \rrbracket}{d_n} \right] \exp\left(-\frac{\llbracket \mathrm{u}_t \rrbracket^2}{d_t^2} \right) \right\} \tag{3.21}$$

in which, $\llbracket \mathrm{u}_n \rrbracket$ and $\llbracket \mathrm{u}_t \rrbracket$ are the components of the displacement jump vector along the normal and tangential directions, respectively; d_n and d_t the normal and tangential cohesive characteristic separation lengths, respectively; $y = \llbracket \mathrm{u}_n \rrbracket' / d_n$; $\llbracket \mathrm{u}_n \rrbracket'$ the magnitude of normal

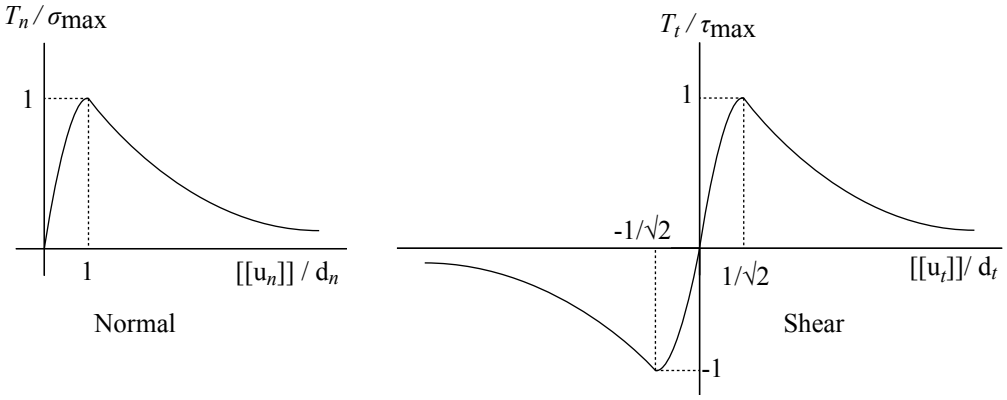

Figure 3.4: The exponential traction-separation laws by Xu and Needleman [114].

displacement jump when complete shear failure has taken place; $q = \Phi_t/\Phi_n$; Φ_n the normal surface potential energy; and Φ_t is the tangential surface potential energy. Φ_n and Φ_t represent the areas under the normal and tangential traction-separation curves, respectively. The normalized exponential normal and tangential traction-separation behavior is illustrated in Fig. 3.4. This dissertation focuses on cases, where the composite is subjected to tensile loading. In cases of compression or shear loading, it is necessary to explicitly impose the impenetrability condition (i.e., $[\![u_n]\!] \geq 0$) in the cohesive law as well.

Differentiating Eq. 3.21 with respect to the components of the displacement jump normal and tangential to the fiber direction, the components of the traction vector are obtained:

$$T_n = \frac{\Phi_n}{d_n}\exp\left(-\frac{[\![u_n]\!]}{d_n}\right)\left\{\frac{[\![u_n]\!]}{d_n}\exp\left(-\frac{[\![u_t]\!]^2}{d_t^2}\right) + \frac{1-q}{y-1}\left[1-\exp\left(-\frac{[\![u_t]\!]^2}{d_t^2}\right)\right]\left[y-\frac{[\![u_n]\!]}{d_n}\right]\right\} \tag{3.22}$$

$$T_t = 2\left(\frac{\Phi_n[\![u_t]\!]}{d_t^2}\right)\left\{q+\frac{1-q}{y-1}\frac{[\![u_n]\!]}{d_n}\right\}\exp\left(-\frac{[\![u_n]\!]}{d_n}\right)\exp\left(-\frac{[\![u_t]\!]^2}{d_t^2}\right) \tag{3.23}$$

In some of the numerical verification studies below, a simpler bilinear cohesive law is

considered. In this model, the uncoupled tangential and normal tractions are expressed as:

$$T_n(\llbracket \mathrm{u}_n \rrbracket) = \begin{cases} \dfrac{\llbracket \mathrm{u}_n \rrbracket}{d_n}\sigma_{\max} & d_n \geq \llbracket \mathrm{u}_n \rrbracket \geq 0 \\ \dfrac{\sigma_{\max}}{d_n^{\mathrm{crit}} - d_n}\left(d_n^{\mathrm{crit}} - \llbracket \mathrm{u}_n \rrbracket\right) & d_n^{\mathrm{crit}} \geq \llbracket \mathrm{u}_n \rrbracket \geq d_n \\ 0 & \llbracket \mathrm{u}_n \rrbracket \geq d_n^{\mathrm{crit}} \end{cases} \tag{3.24}$$

$$T_t(\llbracket \mathrm{u}_t \rrbracket) = \begin{cases} \dfrac{\llbracket \mathrm{u}_t \rrbracket}{d_t}\tau_{\max} & d_t \geq \llbracket \mathrm{u}_t \rrbracket \geq 0 \\ \dfrac{\tau_{\max}}{d_t^{\mathrm{crit}} - d_t}\left(d_t^{\mathrm{crit}} - \llbracket \mathrm{u}_t \rrbracket\right) & d_t^{\mathrm{crit}} \geq \llbracket \mathrm{u}_t \rrbracket \geq d_t \\ 0 & \llbracket \mathrm{u}_t \rrbracket \geq d_t^{\mathrm{crit}} \end{cases} \tag{3.25}$$

where; d_n and d_t are described identical to the exponential law; $\sigma_{\max}$ and $\tau_{\max}$ denote the ultimate normal and tangential tractions, respectively; d_n^{crit} and d_t^{crit} are the maximum normal and tangential displacement jumps, respectively.

The two cohesive zone laws considered above are intrinsic, i.e., contains a linear "hardening" portion. For certain problems, the intrinsic laws were found to lead to spurious softening [2] and numerical instability [21], compared to the extrinsic cohesive laws. Despite numerical difficulties, the intrinsic laws have been much more popular due to the simplicity of their implementation into standard finite element codes using cohesive zone elements. In the current approach, since the cohesive behavior is introduced through enrichment functions, the implementation of extrinsic laws do not significantly differ from intrinsic laws. The intrinsic laws are considered here, due to the availability of commercial software that serves as reference models in numerical verifications discussed below.

3.4 Computational Formulation and Implementation

The governing equations in Eqs. 2.10-2.13, Eq. 3.6 and Eqs. 3.8-3.13 are discretized and evaluated based on the extended finite element method following the standard Ritz-Galerkin procedure. Matrix notation is employed in the formulations for convenience. The weak form

of the governing equation (Eq. 3.13) is re-written in the matrix form as:

$$\int_{\Omega} \delta\boldsymbol{\epsilon}^T \boldsymbol{\sigma}\, d\Omega - \int_{\Gamma_t} \delta\mathbf{u}^T \tilde{\mathbf{t}}\, d\Gamma + \sum_{\alpha=1}^{n} t_\alpha E_f \int_{\Omega_\alpha} \epsilon_f^\alpha \delta\epsilon_f^\alpha\, d\Omega + \sum_{\alpha=1}^{n} \int_{\Gamma_\alpha} \delta[\![\mathbf{u}]\!]^T \boldsymbol{T}\, d\Gamma = 0 \tag{3.26}$$

where, the superscript T indicates transpose.

The discretization of the displacement field follows Eq. 3.1, and using the Bubnov-Galerkin approach, the discretization of the test function is similar to that of the trial function. In contrast to the standard finite element approach, the mesh does not necessarily conform to the fiber domains, i.e., the position of the fibers are independent of the mesh. The first term in Eq. 3.26 becomes:

$$\int_{\Omega} \delta\boldsymbol{\epsilon}^T \boldsymbol{\sigma}\, d\Omega = \sum_{e=1}^{n_e} \int_{\Omega_e} \delta\boldsymbol{\epsilon}^T \boldsymbol{\sigma}\, d\Omega \tag{3.27}$$

in which, n_e is the total number of elements discretizing the domain; and Ω_e the domain of the element, e. Substituting the test and trial function discretizations into Eq. 3.27, the element level integral is expressed as:

$$\int_{\Omega_e} \delta\boldsymbol{\epsilon}^T \boldsymbol{\sigma}\, d\Omega = (\mathbf{V}^e)^T \int_{\Omega_e} (\mathbf{B}^e)^T \boldsymbol{\sigma}\,(\mathbf{U}^e)\; d\Omega \tag{3.28}$$

where, $\mathbf{U}^e$ and $\mathbf{V}^e$ are the nodal coefficient vectors of the trial and test functions in element, e, respectively:

$$\mathbf{U}^e = \left\{\hat{\mathbf{u}}^e;\, \hat{\mathbf{c}}^e;\, \hat{\mathbf{d}}^e\right\};\quad \mathbf{V}^e = \left\{\delta\hat{\mathbf{u}}^e;\, \delta\hat{\mathbf{c}}^e;\, \delta\hat{\mathbf{d}}^e\right\} \tag{3.29}$$

in which, a semicolon implies that the construction forms a column vector. The three components in the nodal coefficient vectors correspond to the standard, fiber enrichment and the jump enrichment degrees of freedom respectively:

$$\hat{\mathbf{u}}^e = \left\{\hat{\mathbf{u}}_1^e;\, \hat{\mathbf{u}}_2^e;\, \ldots;\, \hat{\mathbf{u}}_{n_n^e}^e\right\}\quad \hat{\mathbf{c}}^e = \left\{\hat{\mathbf{c}}_1^e;\, \hat{\mathbf{c}}_2^e;\, \ldots;\, \hat{\mathbf{c}}_{n_{\text{en}}^e}^e\right\}\quad \hat{\mathbf{d}}^e = \left\{\hat{\mathbf{d}}_1^e;\, \hat{\mathbf{d}}_2^e;\, \ldots;\, \hat{\mathbf{d}}_{n_{\text{en}}^e}^e\right\} \tag{3.30}$$

where, $\hat{\mathbf{u}}_a^e$, $\hat{\mathbf{c}}_a^e$ and $\hat{\mathbf{d}}_a^e$ are the vectors of unknown coefficients for standard and extended degrees of freedom at element, e and node a; and n_n^e and n_{en}^e the number of standard and enriched nodes within element, e, respectively.

$$\mathbf{B}^e = \left\{ \hat{\mathbf{B}}_1^e,\ \hat{\mathbf{B}}_2^e,\ \ldots,\ \hat{\mathbf{B}}_{n_n^e}^e,\ \bar{\mathbf{B}}_1^e,\ \bar{\mathbf{B}}_2^e,\ \ldots,\ \bar{\mathbf{B}}_{n_{\text{en}}^e}^e,\ \tilde{\mathbf{B}}_1^e,\ \tilde{\mathbf{B}}_2^e,\ \ldots,\ \tilde{\mathbf{B}}_{n_{\text{en}}^e}^e \right\} \tag{3.31}$$

in which, the gradient terms are expressed as:

$$\hat{\mathbf{B}}_a^e = \begin{bmatrix} N_{a,x}^e & 0 \\ 0 & N_{a,y}^e \\ N_{a,y}^e & N_{a,x}^e \end{bmatrix};\ \bar{\mathbf{B}}_a^e = \begin{bmatrix} (N_a^e\,\psi)_{,x} & 0 \\ 0 & (N_a^e\,\psi)_{,y} \\ (N_a^e\,\psi)_{,y} & (N_a^e\,\psi)_{,x} \end{bmatrix};\ \tilde{\mathbf{B}}_a^e = \begin{bmatrix} (N_a^e\,\Upsilon)_{,x} & 0 \\ 0 & (N_a^e\,\Upsilon)_{,y} \\ (N_a^e\,\Upsilon)_{,y} & (N_a^e\,\Upsilon)_{,x} \end{bmatrix} \tag{3.32}$$

where, a subscript followed by a comma indicates differentiation. The first term in Eq. 3.26 is then written in the matrix form as:

$$\mathbf{V}^T \mathbf{f}_{\text{int},1}(\mathbf{U}) \tag{3.33}$$

in which, the internal force component is obtained by assembling the corresponding element matrices:

$$\mathbf{f}_{\text{int},1}(\mathbf{U}) = \mathop{\mathbf{A}}_{e=1}^{n_e} \int_{\Omega_e} (\mathbf{B}^e)^T \boldsymbol{\sigma}\,(\mathbf{U}^e)\ d\Omega \tag{3.34}$$

$\mathbf{U}$ and $\mathbf{V}$ are obtained by assembling the corresponding element vectors. Where $\boldsymbol{\sigma}$ at an arbitrary position $\hat{\mathbf{x}}$ is defined in the discretized form as:

$$\boldsymbol{\sigma} = (1-w)\,\mathbf{L}\,\mathbf{B}^e\mathbf{U}^e \tag{3.35}$$

Decomposing the boundary integral into its elemental components, the external force

contribution in Eq. 3.26 is expressed as:

$$\int_{\Gamma_t} \delta \mathbf{u}^T \tilde{\mathbf{t}} \, d\Gamma = \mathbf{V}^T \mathbf{f}_{\text{ext}} \tag{3.36}$$

in which, the external force vector is obtained through the assembly of the elemental contributions:

$$\mathbf{f}^e_{\text{ext}} = \int_{\Gamma^e_t} \mathbf{f}^e(\mathbf{x}) \, d\Gamma; \quad e \in \mathcal{I}^t \tag{3.37}$$

where, $\mathcal{I}^t$ denotes the index set of elements along the traction boundary, Γ_t; Γ^e_t the part of the traction boundary approximated by element e; and:

$$\mathbf{f}^e = \left\{ \hat{\mathbf{f}}^e_1; \hat{\mathbf{f}}^e_2; \ldots; \hat{\mathbf{f}}^e_{n^e_n}; \bar{\mathbf{f}}^e_1; \bar{\mathbf{f}}^e_2; \ldots; \bar{\mathbf{f}}^e_{n^e_{\text{en}}}; \tilde{\mathbf{f}}^e_1; \tilde{\mathbf{f}}^e_2; \ldots; \tilde{\mathbf{f}}^e_{n^e_{\text{en}}} \right\} \tag{3.38}$$

$$\hat{\mathbf{f}}^e_a(\mathbf{x}) = N^e_a(\mathbf{x}) \tilde{\mathbf{t}}(\mathbf{x}); \quad \bar{\mathbf{f}}^e_a(\mathbf{x}) = \hat{\mathbf{f}}^e_a(\mathbf{x}) \psi(\mathbf{x}); \quad \tilde{\mathbf{f}}^e_a(\mathbf{x}) = \hat{\mathbf{f}}^e_a(\mathbf{x}) \Upsilon(\mathbf{x}) \tag{3.39}$$

3.4.1 Fiber deformation

The third term in Eq. 3.26 accounts for the deformation of the fibers. The integral term is expressed in terms of its components that lie in each enriched element as:

$$\int_{\Omega_\alpha} \epsilon^\alpha_f \delta \epsilon^\alpha_f \, d\Omega = \sum_{e=1}^{n^\alpha_e} \int_{\Omega^e_\alpha} \epsilon^\alpha_f \delta \epsilon^\alpha_f \, d\Omega \tag{3.40}$$

in which, n^α_e denotes the number of fully enriched elements that contains a part of the fiber, α. The assumption that the fiber will deform uniformly within each element is made. Therefore, the axial strain of fiber, α, can be defined as:

$$\epsilon^\alpha_f = \frac{[\mathbf{u}(\mathbf{x}^{\alpha e}_2) - \mathbf{u}(\mathbf{x}^{\alpha e}_1)] \cdot \boldsymbol{t}_\alpha}{l_{\alpha e}}; \quad \mathbf{x} \in \Omega^e_\alpha \tag{3.41}$$

where $\mathbf{x}^{\alpha e}_1$ and $\mathbf{x}^{\alpha e}_2$ are the entry and exit positions of the fiber on the enriched element; the length of the fiber segment that lies within the element is denoted as $l_{\alpha e} = ||\mathbf{x}^{\alpha e}_2 - \mathbf{x}^{\alpha e}_1||$;

and $\boldsymbol{t}_\alpha$ is the tangent vector on the fiber domain. When the fiber crosses the domain of the element, the fiber entry and exit positions are on the element edges. If the domain of the fiber ends within the element, the end position of the fiber segment coincides with the fiber tip.

Substituting Eq. 3.41 in the third term in Eq. 3.26 leads to:

$$t_\alpha E_f \int_{\Omega_\alpha^e} \epsilon_f^\alpha \delta\epsilon_f^\alpha \, d\Omega = \frac{t_\alpha E_f}{l_{\alpha e}} \left[(\mathbf{u}(\mathbf{x}_2^{\alpha e}) - \mathbf{u}(\mathbf{x}_1^{\alpha e})) \cdot \boldsymbol{t}_\alpha\right] \left[(\delta\mathbf{u}(\mathbf{x}_2^{\alpha e}) - \delta\mathbf{u}(\mathbf{x}_1^{\alpha e})) \cdot \boldsymbol{t}_\alpha\right]$$
$$= \left(\delta\hat{\mathbf{u}}^e\right)^T \breve{\mathbf{K}}_e^{\alpha s} \hat{\mathbf{u}}^e \quad (3.42)$$

where,

$$\breve{\mathbf{K}}_e^{\alpha s} = \frac{t_\alpha E_f}{l_{\alpha e}} \begin{bmatrix} \breve{\mathbf{K}}_{e,11}^{\alpha s} & \breve{\mathbf{K}}_{e,12}^{\alpha s} & \dots & \breve{\mathbf{K}}_{e,1n_n^e}^{\alpha s} \\ \breve{\mathbf{K}}_{e,21}^{\alpha s} & \breve{\mathbf{K}}_{e,22}^{\alpha s} & & \vdots \\ \vdots & & \ddots & \vdots \\ \breve{\mathbf{K}}_{e,n_n^e 1}^{\alpha s} & \dots & \dots & \breve{\mathbf{K}}_{e,n_n^e n_n^e}^{\alpha s} \end{bmatrix} \quad (3.43)$$

An individual component of the stiffness matrix is written as:

$$\breve{\mathbf{K}}_{e,ab}^{\alpha s} = \left[N_b^e(\mathbf{x}_2^{\alpha e}) - N_b^e(\mathbf{x}_1^{\alpha e})\right] \left[N_a^e(\mathbf{x}_2^{\alpha e}) - N_a^e(\mathbf{x}_1^{\alpha e})\right] (\boldsymbol{t}_\alpha \otimes \boldsymbol{t}_\alpha) \quad (3.44)$$

The internal contribution from the second term in Eq. 3.26 then becomes:

$$\mathbf{f}_{\text{int},2}^\alpha (\mathbf{U}) = \breve{\mathbf{K}}^\alpha \mathbf{U} \quad (3.45)$$

where, the contribution can be computed using the standard assembly operation:

$$\breve{\mathbf{K}}^\alpha = \mathop{\mathbf{A}}_{e=1}^{n_e^\alpha} \breve{\mathbf{K}}_e^\alpha \quad (3.46)$$

The stiffness matrix is nonzero only for the standard degrees of freedom, since the enrichment

functions vanish on the domain of the fiber:

$$\breve{\mathbf{K}}_e^{\alpha} = \begin{bmatrix} \breve{\mathbf{K}}_e^{\alpha s} & \mathbf{0} \\ \mathbf{0} & \mathbf{0} \end{bmatrix} \tag{3.47}$$

3.4.2 Cohesive interfaces

The fourth component of Eq. 3.26 that accounts for the progressive debonding between the fibers and the matrix is expressed in terms of the jump enrichment degrees of freedom. For an arbitrary fiber, α:

$$\int_{\Gamma_\alpha} (\delta[\![\mathbf{u}]\!])^T \, \boldsymbol{T}([\![\mathbf{u}]\!]) \, d\Gamma = (\delta\hat{\mathbf{d}})^T \int_{\Gamma_\alpha} (\mathbf{P}^\alpha)^T \boldsymbol{T}(\hat{\mathbf{d}}) \, d\Gamma = (\delta\hat{\mathbf{d}})^T \mathbf{f}_{\text{int},3}^{d\alpha}(\hat{\mathbf{d}}) \tag{3.48}$$

in which, $\mathbf{P}^\alpha$ includes the shape functions for the jump enrichments:

$$\mathbf{P}^\alpha = \left\{ \mathbf{P}_1^\alpha, \, \mathbf{P}_2^\alpha, \, \ldots, \mathbf{P}_{n_{\text{en}}^\alpha}^\alpha \right\}; \quad \mathbf{P}_a^\alpha = N_{\mathcal{I}_a^\alpha}(\mathbf{x}) \, \Upsilon(\mathbf{x}) \begin{bmatrix} 1 & 0 \\ 0 & 1 \end{bmatrix} \tag{3.49}$$

where, n_{en}^α denotes the number of nodes enriched for fiber, α and $\mathcal{I}^\alpha$ the corresponding nodal index set. The debonding enrichment term is then assembled into a force vector contribution (i.e., $\mathbf{V}^T \mathbf{f}_{\text{int},3}^\alpha(\mathbf{U})$):

$$\mathbf{f}_{\text{int},3}^\alpha = \left\{ \mathbf{0}; \, \mathbf{0}; \, \mathbf{f}_{\text{int},3}^{d\alpha} \right\} \tag{3.50}$$

The null vectors indicate that the internal force contribution is only due to the jump degrees of freedom. Including the three internal force contributions as well as the external force, the resulting equilibrium is expressed in terms of a system of nonlinear equations of the form:

$$\phi(\mathbf{U}) = \mathbf{f}_{\text{int}}(\mathbf{U}) - \mathbf{f}_{\text{ext}} = 0 \tag{3.51}$$

where,

$$\mathbf{f}_{\text{int}}\left(\mathbf{U}\right) = \mathbf{f}_{\text{int},1} + \sum_{\alpha=1}^{n} \left(\mathbf{f}_{\text{int},2}^{\alpha} + \mathbf{f}_{\text{int},3}^{\alpha}\right) \tag{3.52}$$

Equation 3.52 is evaluated incrementally using the Newton-Raphson method (e.g. [76]).

3.4.3 Numerical integration

The domain is discretized using four different element types (far field, partially enriched, fiber cross enriched, fiber tip enriched) as illustrated in Fig. 2.7 and follow the same numerical integration rules for each element as outlined in Section 2.4.3.

The integration of the cohesive interface (Eq. 3.48) is performed using Gauss quadrature, but independent of the domain discretization. The fiber-matrix interface Γ_α is decomposed into a small number of segments depending on the length of the fiber, l_α. Within each fiber segment, a 12-point quadrature rule is employed.

3.4.4 Treatment of partially enriched elements

The treatment of the partially enriched elements utilizes the same methodology from Section 2.4.4 but is modified slightly for the debonding enrichment. Let $\hat{\psi}(\mathbf{x})$ and $\hat{\Upsilon}(\mathbf{x})$ denote the modified enrichment functions within a partially enriched finite element:

$$\hat{\psi}(\mathbf{x}) = \sum_{b\in\mathcal{I}_e} N_b(\mathbf{x})\psi(\mathbf{x}); \quad \mathbf{x}\in\Omega_e \tag{3.53}$$

$$\hat{\Upsilon}(\mathbf{x}) = \sum_{c\in\mathcal{I}_e} N_c(\mathbf{x})\Upsilon(\mathbf{x}); \quad \mathbf{x}\in\Omega_e \tag{3.54}$$

where, $\mathcal{I}_e$ are the nodes in the partially enriched element, Ω_e, that are connected to fully enriched elements. The modified enrichment function is active at all nodes of the partially enriched element:

$$\mathbf{u}^e(\mathbf{x}) = \sum_{a=1}^{n_n^e} N_a^e(\mathbf{x})\hat{\mathbf{u}}_a^e + \sum_{b=1}^{n_n^e} N_b^e(\mathbf{x})\hat{\psi}(\mathbf{x})\hat{\mathbf{c}}_b^e + \sum_{c=1}^{n_n^e} N_c^e(\mathbf{x})\hat{\Upsilon}(\mathbf{x})\hat{\mathbf{d}}_c^e \tag{3.55}$$

in which, all pertinent variables are defined in the partially enriched element are indicated by the superscript, e.

3.5 Numerical Examples

In this section, numerical examples are presented to demonstrate the performance of the XFEM model in evaluating the response of short fiber reinforced composites in a two-dimensional setting. The first example assesses the behavior of multiple random short deformable fibers embedded in an elastic matrix with perfect interfacial cohesion. The second example illustrates the accuracy characteristics of the method using a single fiber inclusion embedded in a matrix with progressive fiber-matrix debonding. The third example reviews a domain with two fiber inclusions to demonstrate its capabilities in the presence of matrix cracking modeled using nonlocal continuum damage mechanics. The fourth example evaluates the performance of random short fiber composites with varying interface properties.

3.5.1 Elastic response of fibrous composite

This section investigates the response of two-dimensional random short fiber composites in which the fibers are fully bonded to the matrix. No fiber-matrix debonding occurs and the constituents are taken to deform elastically. The problem domain is taken to be 100 mm by 100 mm. The Young's modulus and Poisson's ratio of the matrix material are 14 GPa and 0.3, respectively. The Young's modulus, Poisson's ratio and the thickness of the fibers are 207 GPa, 0.3 and 7 μm, respectively. Fibers are assigned lengths randomly with a mean of 5 mm ($\pm$ 1 mm). The domain was subjected to displacement controlled tensile loading at the right edge. Symmetry boundary conditions are imposed on the left and bottom edges.

Volume element sets with specified weight fractions of between 0.025% and 0.15% were generated and subjected to uniform uniaxial displacement. The overall composite stiffness was computed as a function of fiber weight fraction. The fibers were positioned such that no element within the domain is enriched by more than a single fiber. Six different weight fractions were considered.

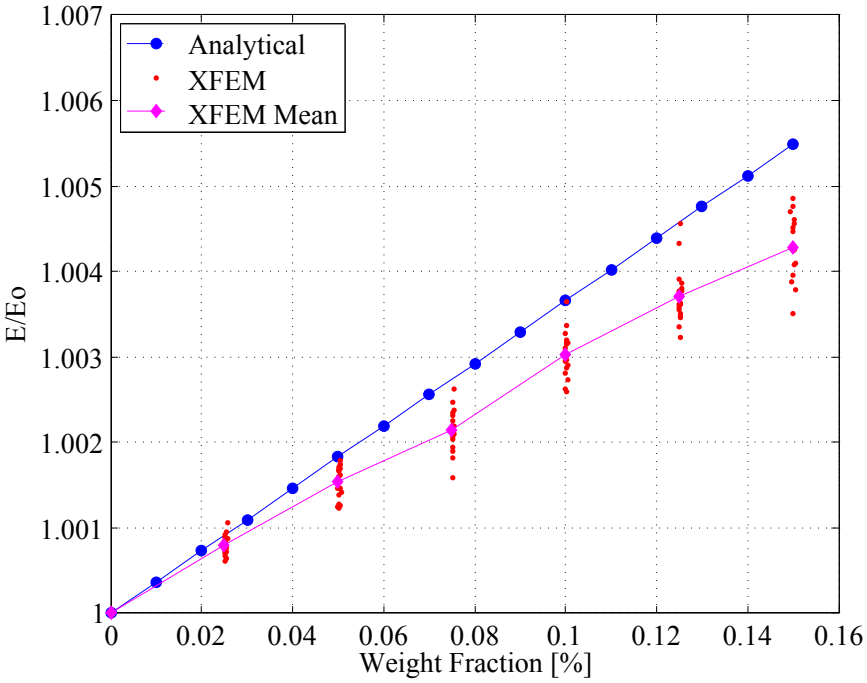

Figure 3.5: Elastic modulus ratio of fibrous composite.

Table 3.1: Condition number ratio of the elastic stiffness matrix as a function of number of fibers in the domain.

Fiber(s) in Domain	1	2	4	8	16	50	300
Condition Number Ratio	1.000	1.002	1.010	1.011	1.015	1.231	3.737

Figure 3.5 illustrates the normalized composite modulus as a function of weight fraction computed by the proposed approach and with the analytical model for a two dimensional randomly oriented fiber composite provided by Pan [81]. At each weight fraction, 20 randomly generated microstructures are simulated with the XFEM model on a uniform grid of 10,000 elements. The results of the XFEM formulation are plotted along with the mean value at each weight fraction. The results of the proposed model display a variation from configuration to configuration at a fixed weight fraction but the discrepancy between the mean and the analytical model is within 0.1% (computed as the error of absolute moduli rather than the normalized moduli). It is also noted that modeling the response of the elastic composite with elastic deformable fibers results in a non prominent increase in strength with an increase in weight fraction (for the weight fraction studied).

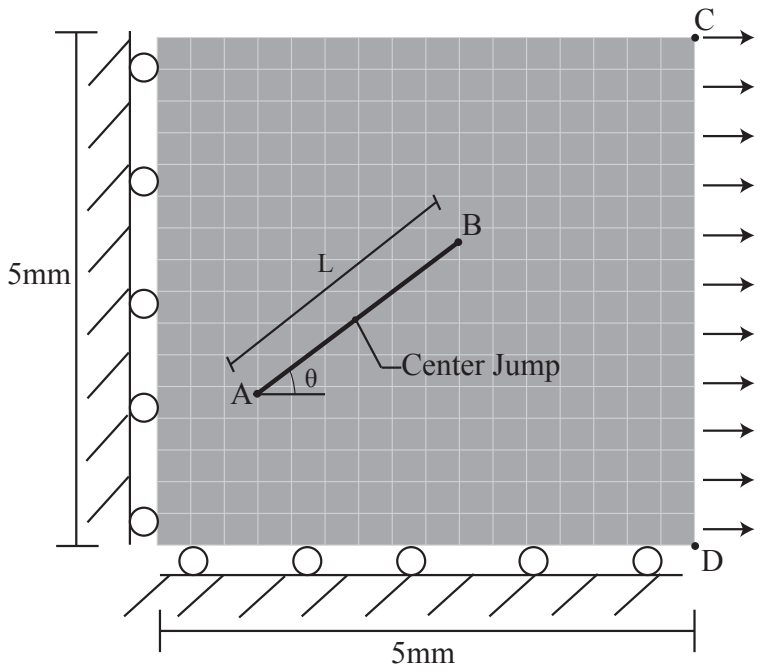

Figure 3.6: Geometry and boundary conditions of the single fiber inclusion examples.

Table 3.1 compares the relative condition numbers of the elastic stiffness matrices of the proposed model as a function of the number of fiber enrichments. The enrichment functions slightly degrade the conditioning of the linear system but the degradation is mild, which points to the stability of the model for high weight fraction composites.

3.5.2 Single fiber inclusion example

The XFEM formulation is verified against the finite element method using a series of simulations of a matrix enriched with a single fiber. The schematic representation of the model problem is shown in Fig. 3.6. The size of the domain is 5 mm by 5 mm and the fiber length, varies between 1-2.5 mm. The domain is subjected to uniform uniaxial tensile loading applied at the right edge. The fiber is placed such that it results in a non-uniform deformation and stress distribution within the matrix. The Young's modulus and Poisson's ratio of the matrix material are 14 GPa and 0.3, respectively. The Young's modulus, Poisson's ratio and thickness of the fiber material are 207 GPa, 0.3 and 7 μm, respectively.

A bi-linear cohesive zone law (defined in Eq. 3.24 and Eq. 3.25) is employed for both the XFEM and the reference simulations. The peak normal traction and normal cohesive characteristic separation length are set to 8 MPa and 0.01591 mm, respectively. The peak shear traction and shear cohesive characteristic separation length are 1.8 MPa and 0.01141 mm, respectively. The maximum cohesive separation length is taken as 0.08 mm under pure normal and pure shear loading [109, 115].

In the XFEM approach, the fiber is idealized as a 1-D line segment with cross sectional area and length properties. The discretization of the domain uses uniform grids ranging from 1,600 elements up to approximately 62,500 elements with corresponding element sizes of h=0.0625 mm and 0.02 mm, respectively. The reference model consists of a very fine and nonuniform (to conform to the fiber domain) discretization, in which the fiber is explicitly modeled as a two dimensional solid. The fiber domain is modeled using a very fine grid with approximately element size of 1 μm. The reference model utilizes 1 μm wide cohesive zone elements that lay along the interface between the fiber and the matrix. The reference model discretization results in approximately 200,000 - 630,000 elements. The simulations confirmed that the response is very accurately captured at such high levels of discretization.

Figure 3.7 shows the point-wise displacement errors of the XFEM model with respect to the reference simulations at peak cohesive tractions (Figs. 3.7a, 3.7c, 3.7e) and at the point of full separation (Figs. 3.7b, 3.7d, 3.7f), respectively. At the point of full separation, the fiber and the matrix are completely debonded from each other at one side of the fiber and the interfacial tractions vanish. The accuracy is assessed at five different locations as illustrated in Fig. 3.6. Points A, B, C, D refer to the left fiber tip, right fiber tip, top right corner and bottom right corner of the problem domain, respectively. The center jump is the displacement jump across the surfaces of the fiber and the matrix, at the center of the fiber. The point-wise errors are computed using the L2 norm and plotted as a function of the mesh size (h). In Figs. 3.7a and 3.7b, the fiber tip locations for all element sizes always coincide with a node. The length of the fiber is 1.44 mm, the angle of fiber is set at 68 degrees,

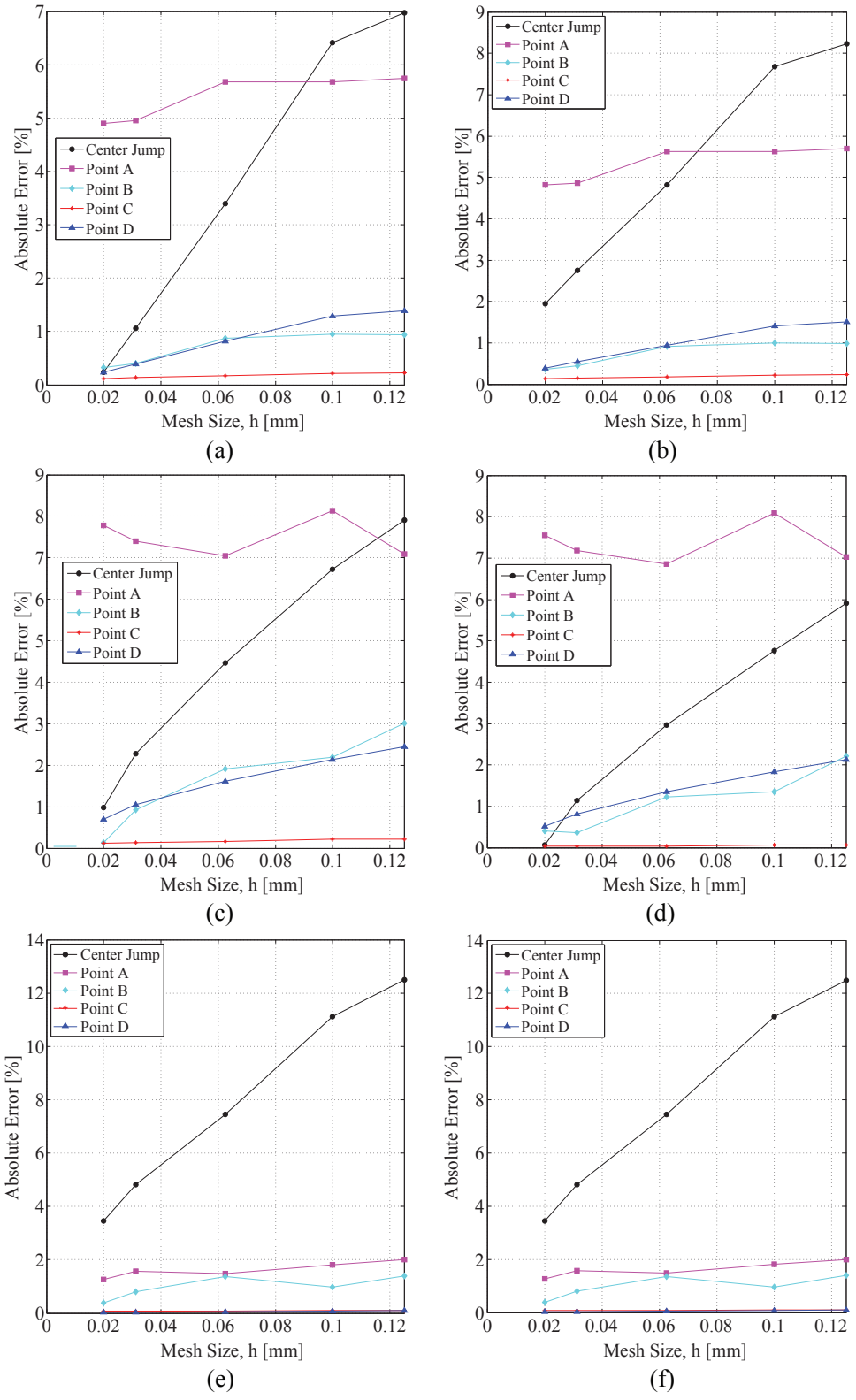

Figure 3.7: Point-wise error as function of mesh density. Fiber tips on element nodes (θ=68 degrees): (a) peak traction and (b) post separation; fiber tips in the elements (θ=45 degrees): (c) peak traction and (d) post separation; fiber tips on edges of elements (θ=17 degrees): (e) peak traction and (f) post separation.

and the left fiber tip location is at (2,1) mm from the origin (bottom left corner of mesh). The error for the corner nodes, right fiber tip and center jump reduces monotonically with increasing mesh density. Errors at the left fiber tips did not show convergence as a function of mesh density. The lack of improvement in the accuracy at point A, is attributed to much smaller absolute magnitude of deformation at point A compared to the other mesh points (i.e., B, C, D) and truncation. The error for the corner nodes, right fiber tip and center jump remained within very reasonable accuracy (i.e., less than 0.5% at the densest mesh).

The effect of fiber tip location on the accuracy characteristics of the XFEM model is further investigated. Figures 3.7c and 3.7d illustrate the accuracy characteristics of the XFEM model when the fiber tips lay within the elements, at peak cohesive tractions and at the point of full separation, respectively. In these simulations, the length of the fiber is set to 2.5 mm, the angle of fiber as 45 degrees, and the left fiber tip location is positioned at (1.61, 1.62) mm from the origin. Figures 3.7e and 3.7f illustrate the accuracy characteristics of the XFEM model when the fiber tips lay on element edges. In these cases, the length of the fiber is 1.08 mm, the angle of fiber is set at 17 degrees, and the left fiber tip location is at (1.5, 3.1) mm from the origin. The XFEM model displays reasonable accuracy and follows the same monotonic trends at the corner nodes, right fiber tip and center jump irrespective of the positioning of the fibers within the matrix.

Figure 3.8 displays the displacement jump along the length of the fiber. At peak cohesive tractions (Figs. 3.8a, 3.8c, 3.8e) and at the point of full separation (Figs. 3.8b, 3.8d, 3.8f), respectively. Figures 3.8a and 3.8b, correspond to the case when the fiber tip locations for all element sizes always coincide with a node. The XFEM model displays monotonic convergence to the reference simulations in terms of magnitude and shape of the displacement jump. Figures 3.8c and 3.8d show the variation of the displacement jump along the length of the fiber when fiber tips are positioned within elements, whereas Figs. 3.8e and 3.8f correspond to the case when the fiber tips lay on element edges, respectively. A clear convergence is observed as a function of the mesh density regardless of fiber positioning within the domain.

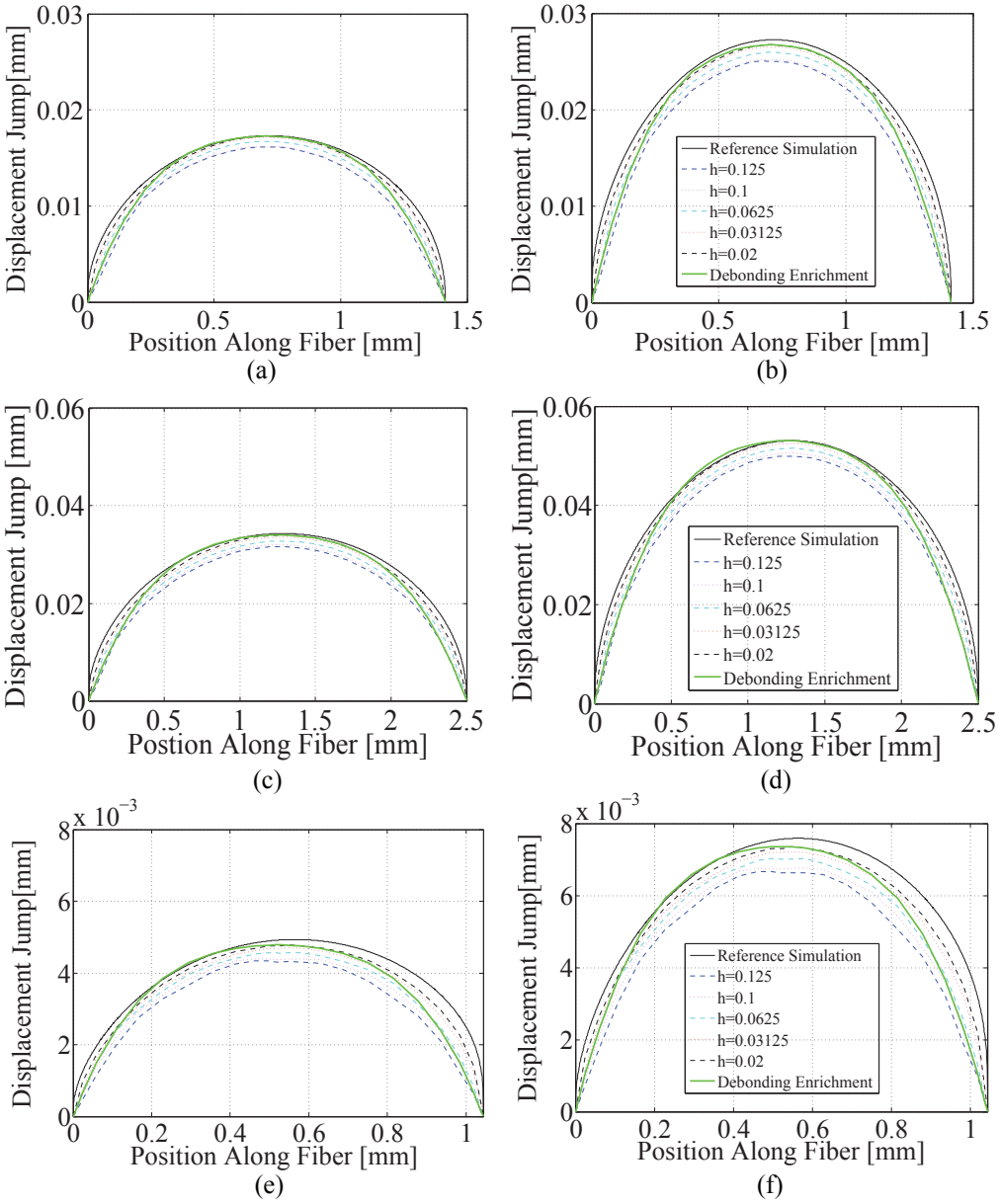

Figure 3.8: Displacement jump across the interface along the fiber length (h is the mesh size). Fiber tips on element nodes: (a) peak traction and (b) post separation; fiber tips in the elements: (c) peak traction and (d) post separation; fiber tips on edges of elements: (e) peak traction and (f) post separation.

The parabolic debonding enrichment function is plotted for the smallest mesh size (h=0.02 mm) for comparison in Fig. 3.8. The simulation results summarized in Fig. 3.8 shows a slight asymmetry in the variation of the displacement jump along the length of the fiber. The deviation from symmetry as measured from the center of the fiber is less than 5% in all cases. The slight deviation is attributed to the non-uniform stress along the length of the fiber, formed due the random positioning of the fiber. The slight variation in errors observed in Figs. 3.7 and 3.8, as a function of fiber positioning, is attributed to the accuracy of the numerical integration. In cases where the fiber tip is too close to a node, the sub elements formed in the Delaunay triangulation for numerical integration of the fully and partially enriched elements have very high aspect ratios. Nevertheless the accuracy of the XFEM model is in reasonable agreement with the reference finite element model in all cases considered.

3.5.3 Two fiber case

In this section, the XFEM model is verified by considering the response of a two fiber composite in the presence of matrix cracking and interface debonding at fiber-matrix interfaces. The model domain is taken as a 5 mm by 5 mm, reinforced with two fibers approximately 1 mm and 1.5 mm in length. The domain is subjected to a uniform uniaxial displacement controlled tensile loading applied at the right edge.

The matrix and fiber properties are the same as in Section 3.5.2. A bi-linear cohesive zone law defined by Eq. 3.24 and Eq. 3.25 is used in both the XFEM model and the reference simulation. The cohesive zone law parameters for this example are based on work from Nicholas et al. [74]. The peak normal traction and normal cohesive characteristic separation length are set as 10 MPa and 1 nm respectively. The peak shear traction and shear cohesive characteristic separation lengths are set to the same as their normal counterparts. The maximum cohesive separation length is taken as 8 nm both for normal and shear directions. The nonlocal damage model described by Eqs. 3.14-3.19 is used for both the XFEM and the reference

simulations. The characteristic length of 0.07 mm and parameters a and b of 49,000 and 19.5, respectively, were employed. A mesh localization analysis is performed using three different mesh sizes identified as coarse, intermediate and fine. The coarse, intermediate and fine reference models include approximately 31,500, 120,000, and 220,000 elements, respectively. The corresponding XFEM models consist of 6,400, 25,600, and 62,500 elements, respectively. In the XFEM models, 266, 504, and 749 elements within the meshes are either enriched or partially enriched for the coarse, intermediate and fine cases, respectively.

Figure 3.9 shows the damage paths computed using the XFEM and reference simulations for the three discretizations with increasing resolution. In this example, the fiber-matrix interfaces have progressive debonding, but complete debonding does not occur. The darker (red) areas indicate that the element is fully damaged and the thin white line displays the initial fiber positions. Damage progressively extends from the left fiber tips to the top and bottom edges of the domain for the top and bottom fibers, respectively. Damage also progressively propagates between the right tips of the top and bottom fibers to create a continuous damage path between the two fibers. Both the reference and XFEM simulations display very similar thickness and location of the damage paths consistent with their specified characteristic length. The damage paths are slightly refined as the mesh density increases in both simulations, but are convergent.

The nonlocal damage paths generated using the reference finite element simulation employ a significantly larger time step size (reference simulations time step size is an order of magnitude larger than XFEM) since the computational cost of the reference simulations is very high. This leads to a slight deviation of uniformity suggested by the nonlocal integral in Eq. 3.19. In contrast, the damage paths generated using the XFEM approach has a uniform thickness.

The load displacement curves for the two fiber simulations computed using the XFEM and reference simulations are displayed in Figure 3.10. For both the reference and XFEM simulations, the peak load and the stress-strain relationship are convergent as a function

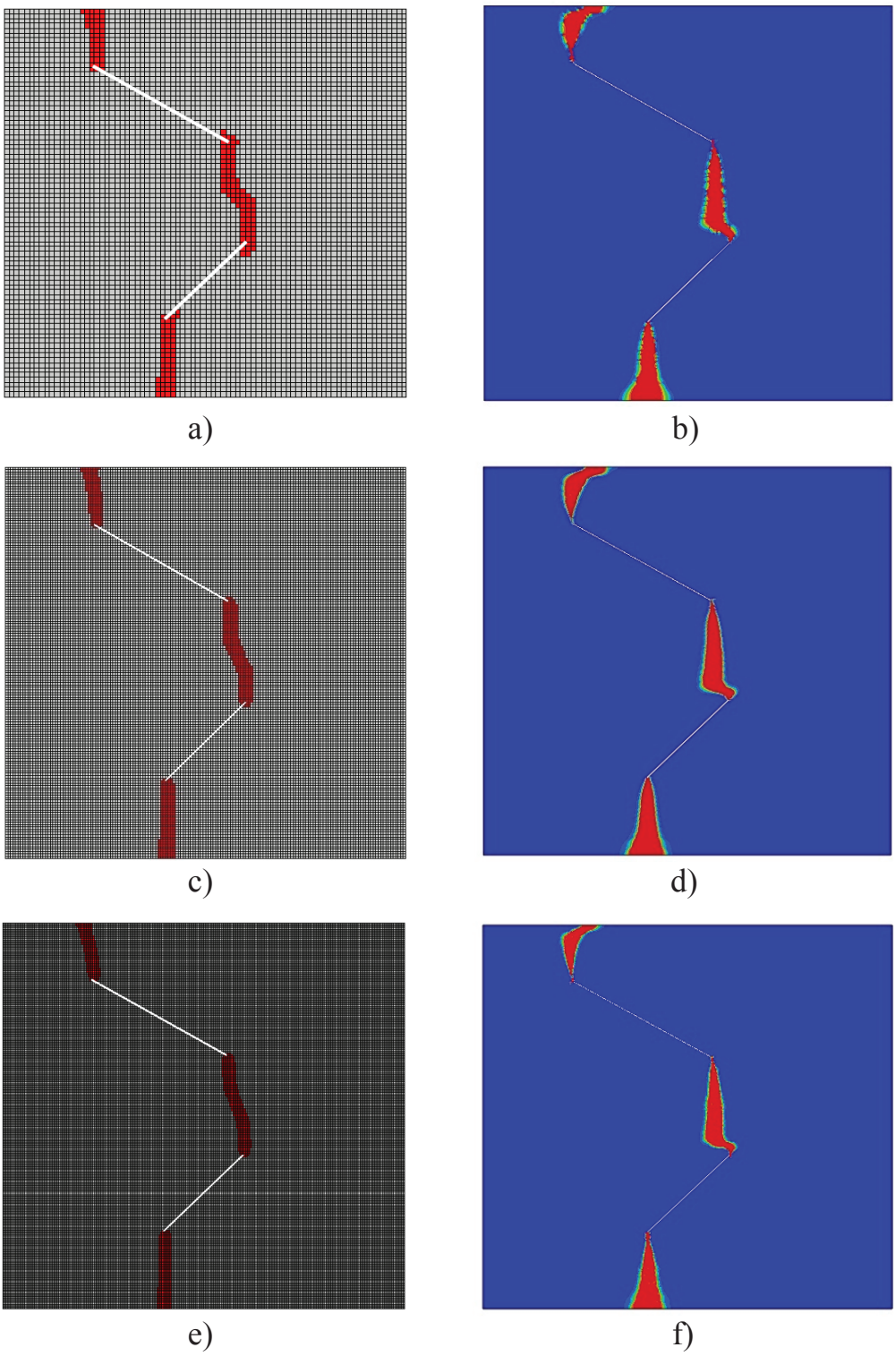

Figure 3.9: Damage paths of two fiber case with a nonlocal damage model. a) XFEM coarse mesh; b) reference simulation coarse mesh; c) XFEM intermediate mesh; d) reference simulation intermediate mesh; e) XFEM fine mesh; f) reference simulation fine mesh.

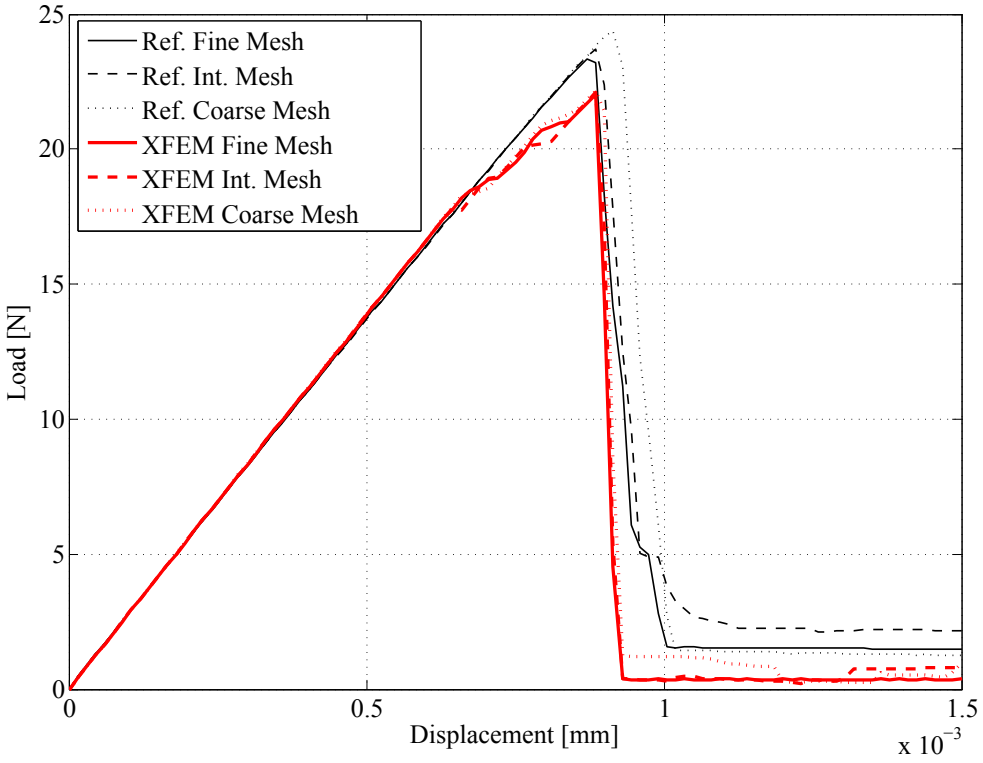

Figure 3.10: Load-displacement curves for XFEM and reference simulations of a two fiber case with different mesh sizes.

of mesh density. The XFEM model displayed a slightly more progressive failure pattern that indicates at approximately 17 N. The absolute error between the respective load peaks of the XFEM and reference simulations is less than 5%. The discrepancy between the converged XFEM and reference simulation results stem from the approximations made in the kinematics of the fiber deformation as well as the fiber-matrix debonding process. The finite element analysis that is considered to be the reference solution resolves the fibers with 2-D finite elements, whereas zero measure inclusions approximate their response in the XFEM approach. The difference between the converged peak loads as well as the post peak response is primarily due to model approximations made in the current approach.

3.5.4 Random short fiber composites

The effect of interfacial properties on the performance of random short fiber reinforced composites is numerically investigated with the proposed XFEM model. A 100 mm by 100 mm domain with randomly oriented short fibers at 0.025% weight fraction is considered. The length of the fibers is also random with the mean length and standard deviation of 5 mm and 2 mm, respectively. The fibers are positioned such that no element within the domain is enriched by more than a single fiber. The domain was subjected to displacement controlled tensile loading at the right edge. Symmetry boundary conditions are imposed on the left and bottom edges. The elastic parameters of the fiber and matrix are taken to be identical to those discussed in Section 3.5.2. The nonlocal damage parameters of a=49,000, b=19.5 and l_c=1 mm are employed to describe the failure progression within the matrix phrase.

The effect of interface properties on the failure response is investigated based on four cases. The first case is when the fibers are considered to be perfectly bonded to the matrix. In this case, the failure initiates and propagates within the matrix phase without interface interactions. The second case consists of the state of complete separation between the fibers and the matrix. All fibers are considered to be fully debonded from the matrix prior to loading at one side of the fiber as described in Section 3.3. The next two cases consider pro-

gressive debonding, idealized using the exponential traction-separation relationships detailed in Eq. 3.22 and Eq. 3.23. The peak traction, characteristic separation length and maximum separation length for the third case are 10 MPa, 1.2 nm, and 6 nm, respectively. The corresponding parameters for the fourth case are 8 MPa, 0.01591 mm, and 0.08 mm for the normal components and 1.8 MPa, 0.01141 mm, and 0.08 mm in the tangential components, respectively.

Figure 3.11 shows the damage contours within the composite domain as a function of interface properties. The contours show the damage state at the end of the loading, where all cases resulted in complete loss of strength of the composite. The path of the final crack is clearly significantly affected by the properties of the interfaces and is different for each of the four simulated cases. In the case of full debonding at the outset, the crack path follows the region of the highest fiber densities since the fiber locations act as pre-cracks in the absence of interface cohesion. Figure 3.12 shows the load-displacement curves of the composite for the four cases investigated. The strength is significantly affected by the interface characteristics. The composite strengths are 4.36 MPa, 1.95 MPa, 3.41 MPa, and 4.08 MPa for cases 1 through 4, respectively. While the strength of the composite is expected in the case of the perfect bonding, the two cases for progressive debonding show significant reduction in strength (22% and 6% for cases 3 and 4, respectively). These results point to the possible gain in composite strength if near optimal interface strength, could be achieved within the constituents. Figure 3.12 also demonstrates a slight reduction in composite ductility as a function of interface strength. This behavior was also experimentally observed by Yoo et al. [118].

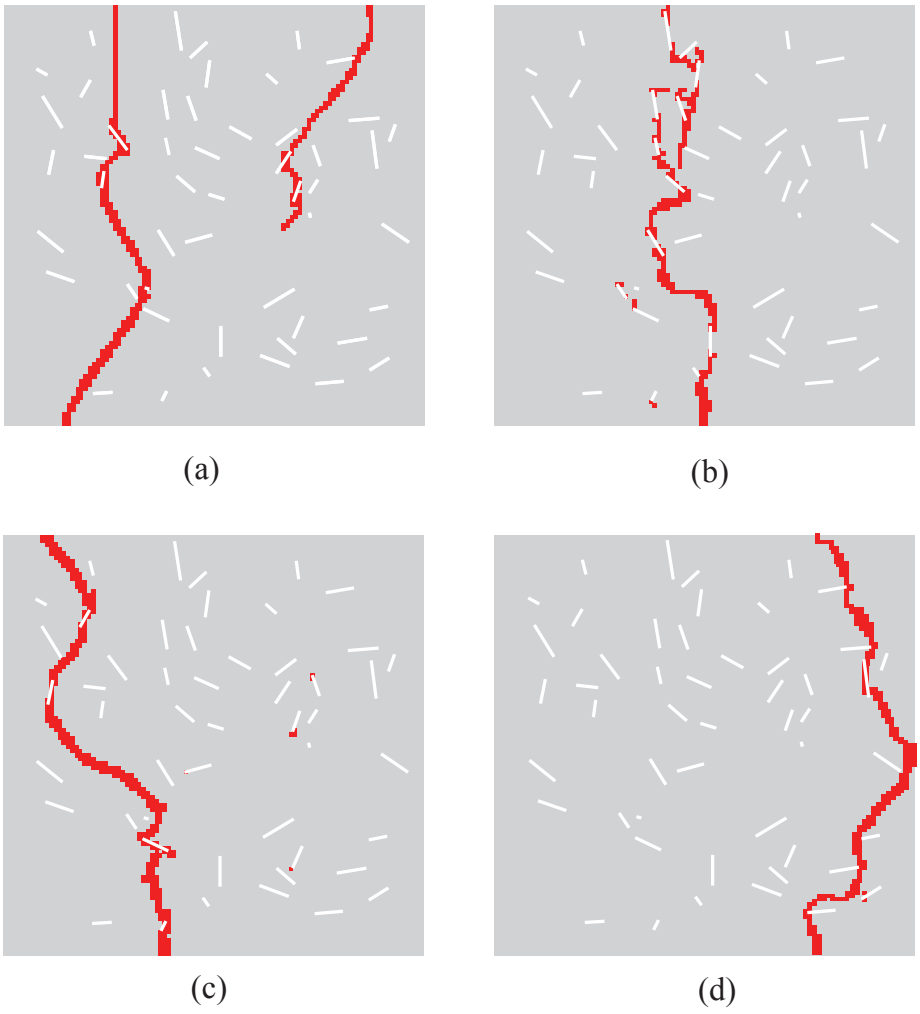

Figure 3.11: Damage prediction for random short fiber composites: (a) case 1: no debonding; (b) case 2: full debonding at the outset; (c) case 3: weak cohesive interface; and (d) case 4: strong cohesive interface.

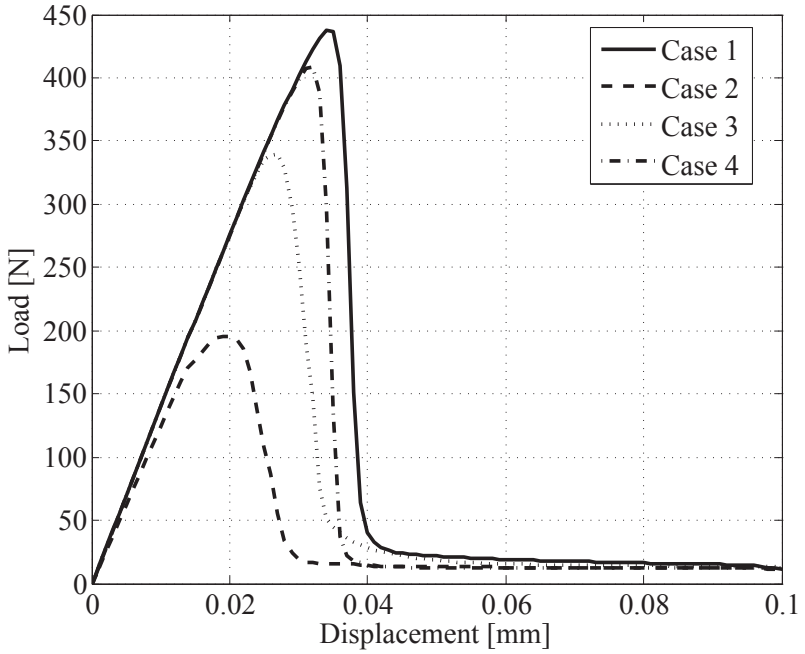

Figure 3.12: Load-displacement curves for the 4 cases of interface properties considered.

CHAPTER 4

INTERACTIONS BETWEEN MULTIPLE ENRICHMENTS IN XFEM OF SHORT FIBER REINFORCED COMPOSITES

4.1 Introduction

This chapter presents an XFEM approach to capture the interactions between fibers in short fiber reinforced composites. The interactions due to fiber inclusion and fiber-matrix debonding enrichments of multiple fibers are investigated. This approach enables problems with significant concentration of fiber enrichment by placing multiple fibers within the same element. This approach improves the computational tractability of the XFEM framework compared to implementations in which an element is restricted to contain enrichments from a single fiber. The work in this chapter is reflected in Ref. [88], and is presented with the permission of Begell House Inc.

In this chapter, an XFEM based enrichment coupling model to capture the interactions between short fibers in composites is presented. In a 2-D setting, elements in the domain are permitted to contain multiple fiber inclusions, where the inclusions are modeled as elastic objects of zero measure. Inclusion and debonding enrichment functions are introduced to model the elastic fiber inclusions and the progressive normal and tangential debonding of the fiber in the matrix. Using this process, the debonding relationship is modeled using cohesive laws. Numerical integration procedures are provided for accurate evaluation of the system response for randomly positioned fibers, including multiple fibers that occupy the same element. Fiber configurations where multiple fibers occupy the same element are numerically investigated using the proposed XFEM model and are assessed against the direct finite element method. With the ability to account for multiple zero measure inclusions within the same element in the domain, the fiber volume fraction percentage in a RVE can be increased without a proportional increase in number of elements in the XFEM domain.

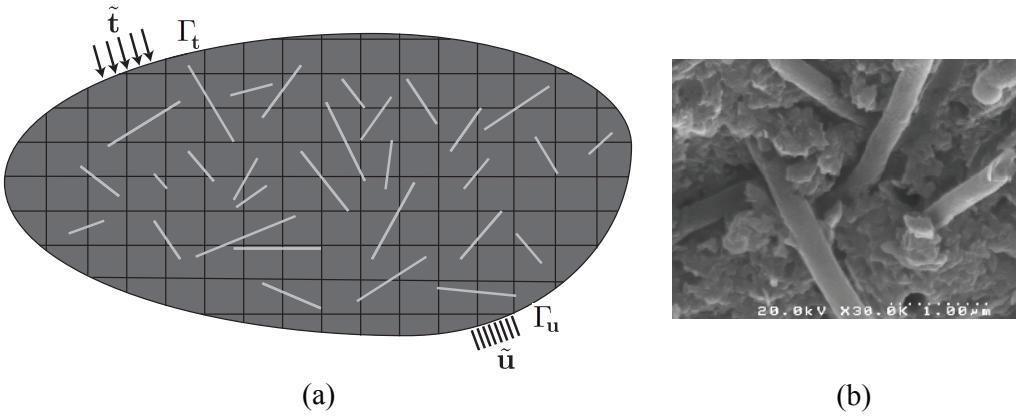

Figure 4.1: (a) Domain and XFEM discretization of the short fiber reinforced composite medium; and (b) short fiber reinforced cement composite (reproduced from [98] with the permission of Elsevier).

The remainder of this chapter is organized as follows. In Section 4.2, the XFEM method is discussed for multiple fibers that lie in the same element. Section 4.3 provides the governing equations and computational formulation, including the model formulation, numerical integration and the treatment of partially enriched elements. Numerical verification studies to assess the performance of this approach and enrichment interactions are presented in Section 4.4.

4.2 XFEM for Multiple Fibers in an Element

In an XFEM domain with random short fibers (Fig. 4.1a), the fibers often lie in the same elements in a uniform grid domain. The random dispersion of numerous fibers is typical for a short fiber reinforced composite (Fig. 4.1b). A domain with multiple fibers in elements can be eliminated by sufficiently refining the mesh to ensure no two fibers are in the same element. To avoid remeshing of the domain, development to account the interaction behavior of multiple fibers in the same element in XFEM is presented.

Eq. 3.1 is modified for the discretization of the displacement field for a domain reinforced

by one or multiple short fiber inclusions:

$$\mathbf{u}(\mathbf{x},t) = \sum_{a=1}^{n_n} N_a(\mathbf{x})\hat{\mathbf{u}}_a + \sum_{\alpha=1}^{n}\left[\sum_{b=1}^{n_{\text{en}}^{\alpha}} N_{\mathcal{I}_b^{\alpha}}(\mathbf{x})\psi_{\alpha}(\mathbf{x})\hat{\mathbf{c}}_{b\alpha}\right] + \sum_{\alpha=1}^{n}\left[\sum_{c=1}^{n_{\text{en}}^{\alpha}} N_{\mathcal{I}_c^{\alpha}}(\mathbf{x})\Upsilon_{\alpha}(\mathbf{x})\hat{\mathbf{d}}_{c\alpha}\right] \tag{4.1}$$

where, $\mathbf{u}$ denotes the displacement field; $\mathbf{x}$ and t are the space and time coordinates, respectively; n_n the total number of mesh nodes in the finite element discretization; n is the number of fibers, n_{en}^{α} is the number of enriched nodes for fiber α; N_a, the standard finite element shape function associated with node a; $\hat{\mathbf{u}}_a$, $\hat{\mathbf{c}}_{b\alpha}$ and $\hat{\mathbf{d}}_{c\alpha}$ the nodal coefficients of the standard, fiber enrichment and debonding enrichments for each fiber α, respectively; $\mathcal{I}^{\alpha}$ is the index set of enriched nodes for fiber α; $\mathcal{I}_a^{\alpha} \in \mathcal{I}^{\alpha}$ the index of an enriched node, a; the fiber enrichment function and the debonding enrichment function are different for each fiber, α, denoted as ψ_{α} and Υ_{α}, respectively.

The standard finite element approximation of the response field corresponds to the first right hand side term in Eq. 4.1. The second term represents the presence of the fiber within the domain, accounting for the strain discontinuity in the approximation space and is a function of the fiber enrichment, ψ_{α}, which is outlined in Section 2.3.1 for each fiber α. The displacement jump due to the progressive loss of the cohesive bond between the fiber and the matrix is represented in the third term and is a function of the debonding enrichment function, Υ_{α} and is outlined in Section 3.2.1 for each fiber α. In elements with multiple fibers, approximation of both the fiber strain and debonding discontinuities are captured for each fiber individually. Therefore, there is a separate set of nodal coefficients for each fiber enrichment.

4.3 Governing Equations and Computational Formulation

The governing equations and model formulation follow the mechanical equilibrium, exterior boundary conditions and weak formulation outlined in the previous chapter (Section 3.3) in Eqs. 2.10-2.13 and Eqs. 3.6-3.13. In this chapter, the matrix is not taken to progressively damage under applied loading, therefore continuum damage mechanics are not utilized.

The physical deterioration occurring at the interface is represented by the bilinear cohesive zone law expressed in Eq. 3.24 and Eq. 3.25. The bilinear cohesive law is applied in order to verify the numerical analysis later in this chapter.

XFEM is employed to discretize and evaluate the governing equations. The weak form of the governing equation (Eq. 3.13), is outlined in Eq. 3.26. The computational formulation follows the same approach as in Section 3.4, but it reviewed and presented again for with slight modifications for elements with multiple fibers in them.

The Bubnov-Galerkin approach is utilized following Eq. 4.1. The first term in Eq. 3.26 is has the same form as in Section 3.4 and is expressed in Eq. 3.33.

The nodal coefficient vectors of the trial and test functions in element e with multiple fiber inclusions, are $\mathbf{U}^e$ and $\mathbf{V}^e$, respectively, are the same as in Section 3.4. They are expressed below for convenience:

$$\mathbf{U}^e = \left\{ \hat{\mathbf{u}}^e;\, \hat{\mathbf{c}}^e;\, \hat{\mathbf{d}}^e \right\}; \quad \mathbf{V}^e = \left\{ \delta\hat{\mathbf{u}}^e;\, \delta\hat{\mathbf{c}}^e;\, \delta\hat{\mathbf{d}}^e \right\} \tag{4.2}$$

The size of the fiber enrichment $\hat{\mathbf{c}}^e$, and jump enrichment $\hat{\mathbf{d}}^e$, degrees of freedom vectors may differ for each element, and depends on the number of fiber enrichments included in the element as well as whether the enrichment for each fiber is full or partial as described below.

The gradient vector $\mathbf{B}^e$, remains the same as in Eq. 3.31. Since the gradient terms are based on the standard elements and each individual fiber α, they are slightly modified to reflect multiple fibers that lie in the same element. They are expressed as:

$$\hat{\mathbf{B}}_a^e = \begin{bmatrix} N_{a,x}^e & 0 \\ 0 & N_{a,y}^e \\ N_{a,y}^e & N_{a,x}^e \end{bmatrix}; \; \bar{\mathbf{B}}_a^e = \begin{bmatrix} (N_a^e\,\psi_\alpha)_{,x} & 0 \\ 0 & (N_a^e\,\psi_\alpha)_{,y} \\ (N_a^e\,\psi_\alpha)_{,y} & (N_a^e\,\psi_\alpha)_{,x} \end{bmatrix}; \; \tilde{\mathbf{B}}_a^e = \begin{bmatrix} (N_a^e\,\Upsilon_\alpha)_{,x} & 0 \\ 0 & (N_a^e\,\Upsilon_\alpha)_{,y} \\ (N_a^e\,\Upsilon_\alpha)_{,y} & (N_a^e\,\Upsilon_\alpha)_{,x} \end{bmatrix} \tag{4.3}$$

The external force contribution from Eq. 3.26 is outlined in Section 3.4 and is presented in Eqs. 3.36-3.39.

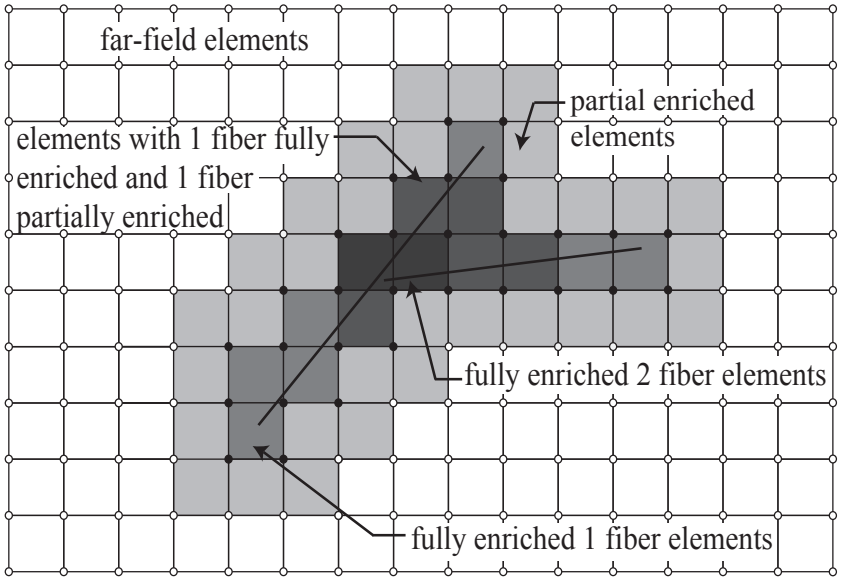

Figure 4.2: Decomposition of the problem domain into subdomains of far-field elements approximated by standard basis, partially and fully enriched elements for two fibers occupying the same elements in a domain.

The deformation of the fibers are accounted for independently and are directly incorporated into the Lagrangian are accounted for in the third term in Eq. 3.26. Section 3.4.1 outlines this process in Eqs. 3.40-3.47.

The progressive debonding between the fiber and the matrix is accounted for in the fourth component of Eq. 3.26 and each interface is applied independently to capture the behavior. Eqs. 3.48-3.52 in Section 3.4.2 outlines this procedure.

The Newton-Raphson method is used to incrementally evaluate the nonlinear system

4.3.1 Numerical integration

The numerical integration of enriched elements differs for various element types depending on the configuration of the inclusions that lie within them.

The domain consists of four different element types as illustrated in Fig. 4.2: (1) Far field elements with no enrichment; (2) elements with partial enrichment from one or multiple fibers; (3) fully enriched elements crossed by one or multiple fibers; and (4) fully enriched elements crossed by fibers and partially enriched by additional fibers.

The integration rules are updated from Section 2.4.3 to include multiple fiber inclusions in each element. The rules for various element types are as follows:

1. Far field elements: Elements have no enrichment. Since no additional functions are employed, the element integration is performed using the standard quadrature rules.

2. Partially enriched elements: Some nodes include enrichment from one or multiple fiber inclusions but no intra-element strain or displacement discontinuity exists. Standard integration is employed. Higher order integration rules could increase the accuracy, but are not employed for efficiency.

3. Fully enriched elements that contain one or multiple fiber inclusions: The elements take into consideration the amount and location of the fiber inclusions rather than integrating the elements for each inclusion separately. The elements are either split by the fibers or contain fiber tips (see Fig. 4.3). For the split fiber, Delaunay triangulation is used to decompose each split part into triangular sub-elements. For fiber tip elements, the elements are split along the normal direction at the fiber tip and along the fiber direction and Delaunay triangulation is used to decompose each split part into triangular sub-elements. The element splitting at the fiber normal ensures that the components of the enrichment function that pertain to the fiber tip and fiber level sets are integrated separately. For both cases, high order integration rules are used in each sub-element.

4. Fully enriched elements that contain a fiber inclusion and are partially enriched by additional fibers: The elements use the same element splitting rules as in the full enriched element type, and use higher order integration rules for each sub element. The element is treated for the full enrichment of the inclusions in the element as well as for the partial enrichments of the element.

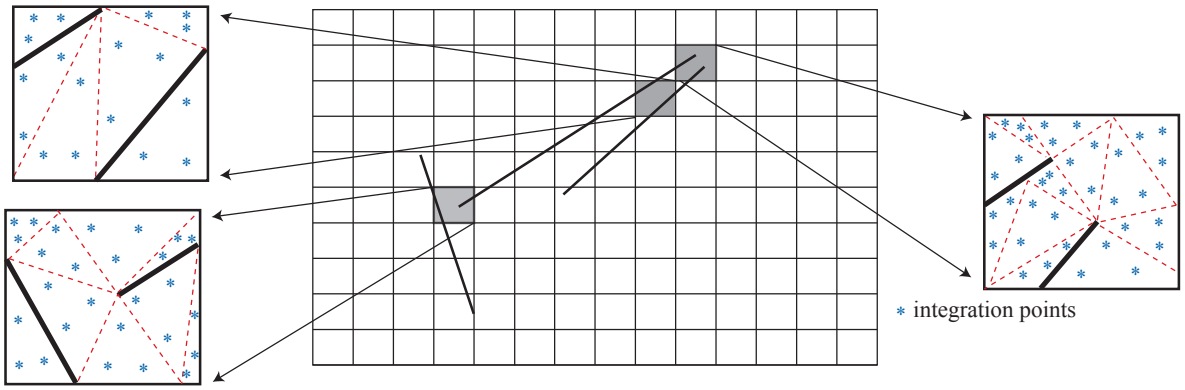

Figure 4.3: Integration of elements with multiple fibers.

4.3.2 Effect of mesh refinement on numerical integration

When modeling multiple fibers in close proximity, mesh refinement has a significant effect on numerical integration. The change in numerical integration in turn effects the mesh convergence studies as described below and lead to non-monotone convergence.

Figure 4.4 illustrates two neighboring fibers in a domain discretized using three meshes with increasing mesh density. In Fig. 4.4a, a single element encompasses both fibers. When the element size is reduced as in Fig. 4.4b, two elements are intersected by both fibers, whereas the two other elements are intersected by a single fiber. Figure 4.4c displays the same fibers when the element size is further decreased. In this case, there are no elements intersected by more than a single fiber. The integration rules for the three cases are quite different from each other and potentially leads to non-monotone convergence.

4.3.3 Treatment of partially enriched elements

In elements that are partially enriched (i.e. elements that have some nodes that are enriched but not all of the nodes), the approach in Section 3.4.4 is revised to account for multiple fiber inclusions that lie in the same element.

For each fiber, α, the modified enrichment functions, $\hat{\psi}_\alpha(\mathbf{x})$ and $\hat{\Upsilon}_\alpha(\mathbf{x})$, in the partially enriched finite element are denoted as:

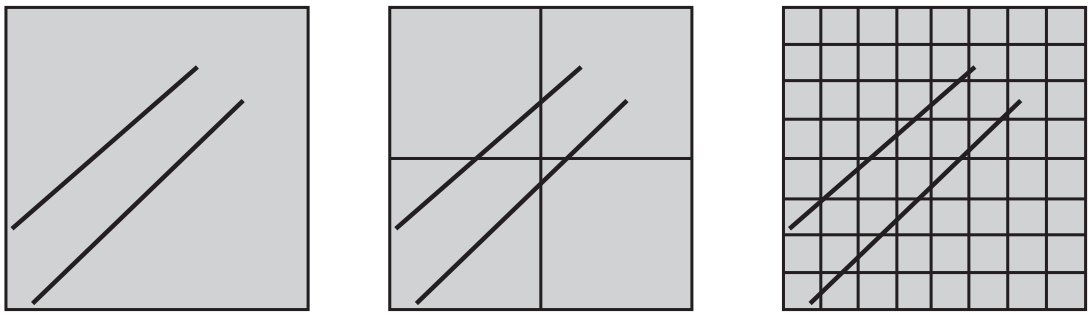

Figure 4.4: Change in the integration rules as a function of mesh density: (a) coarse discretization; (b) medium discretization; and (c) fine discretization.

$$\hat{\psi}_\alpha(\mathbf{x}) = \sum_{b \in \mathcal{I}_e^\alpha} N_b(\mathbf{x}) \psi_\alpha(\mathbf{x}); \quad \mathbf{x} \in \Omega_e \tag{4.4}$$

$$\hat{\Upsilon}_\alpha(\mathbf{x}) = \sum_{c \in \mathcal{I}_e^\alpha} N_c(\mathbf{x}) \Upsilon_\alpha(\mathbf{x}); \quad \mathbf{x} \in \Omega_e \tag{4.5}$$

where, $\mathcal{I}_e$ are the nodes in the partially enriched element, Ω_e, that are connected to fully enriched elements. The modified enrichment function is active at all nodes of the partially enriched element:

$$\mathbf{u}^e(\mathbf{x}) = \sum_{a=1}^{n_n^e} N_a^e(\mathbf{x}) \hat{\mathbf{u}}_a^e + \sum_{\alpha=1}^{n} \left[\sum_{b=1}^{n_{n\alpha}^e} N_b^e(\mathbf{x}) \hat{\psi}_\alpha(\mathbf{x}) \hat{\mathbf{c}}_{b\alpha}^e \right] + \sum_{\alpha=1}^{n} \left[\sum_{c=1}^{n_{n\alpha}^e} N_c^e(\mathbf{x}) \hat{\Upsilon}_\alpha(\mathbf{x}) \hat{\mathbf{d}}_{c\alpha}^e \right] \tag{4.6}$$

4.4 Numerical Examples

In this section, the performance of the XFEM model in evaluating the response of short fiber reinforced composites with emphasis on the interactions between fibers that lie in the same element is presented with numerical examples. The first example assesses the accuracy characteristics of two fiber inclusion domains embedded in an elastic matrix with perfect interfacial cohesion. The second example illustrates the accuracy characteristics

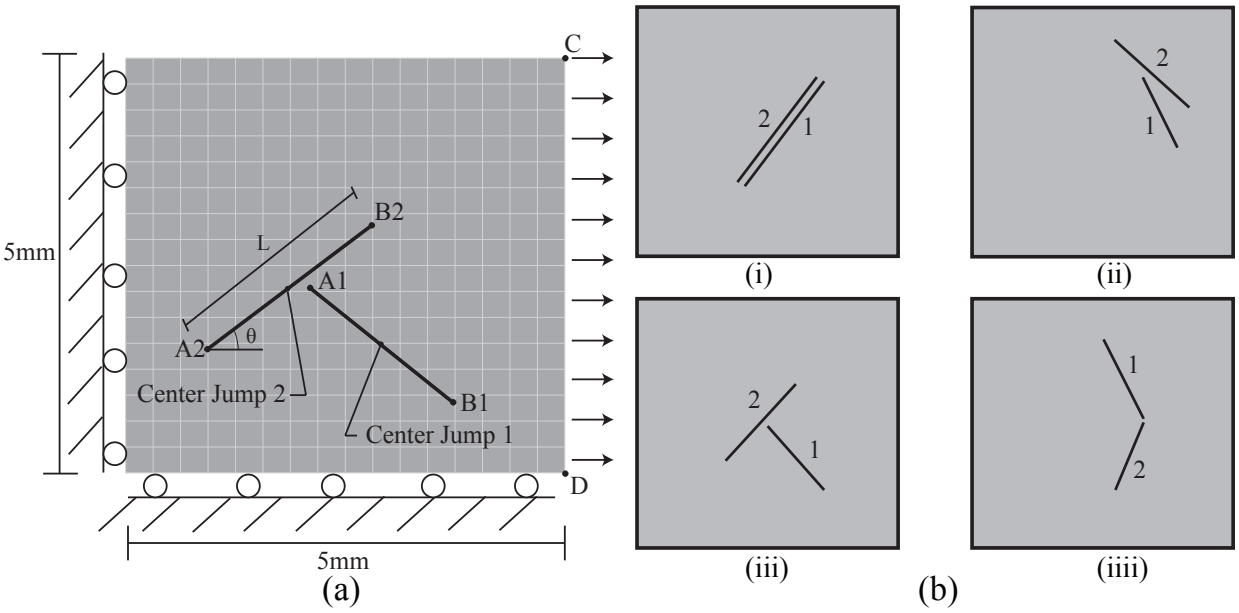

Figure 4.5: (a) Geometry and boundary conditions of a two fiber inclusion example; and (b) fiber configurations of the four cases studied in the numerical verification: (i) case 1; (ii) case 2; (iii) case 3; and (iiii) case 4.

when progressive fiber-matrix debonding is incorporated, including capturing the debonding interaction behavior. The third example investigates the debonding interaction behavior when four fibers are in close proximity of each other and have fibers that lie in the same element. The fourth example displays the case of a domain with a dense population of fibers.

4.4.1 Elastic response of multiple fiber inclusions

The XFEM formulation is verified against the finite element method for an elastic response using a series of simulations of a matrix enriched with two fibers. Four fiber configuration cases were investigated. Each case consists of a domain with two fiber inclusions that have portions of each fiber in close proximity to each other, but they do not touch or overlap. In all cases, the fibers were placed such that there were elements that contained both fibers, for all mesh sizes studied.

The schematic representation of the model problem is shown in Fig. 4.5a. The size of the domain is 5 mm by 5 mm and the fiber length varies between 0.83-2.65 mm. The domain is subjected to uniform displacement controlled tensile loading at the right edge and symmetry

boundary conditions are imposed on the left and bottom edges. The matrix material is taken to be concrete with the Young's modulus and Poisson's ratio of the matrix being 14 GPa and 0.3, respectively. The fibers are taken to be high strength carbon fibers with the Young's modulus and thickness of 207 GPa and 7 μm, respectively. This example investigates the response of two-dimensional short fiber composites in which the fibers are fully bonded to the matrix. No fiber-matrix debonding occurs and the constituents are taken to deform elastically.

Figure 4.5b illustrates the configurations considered in the verification study. Case 1 consists of two fibers that are parallel to each other with both fibers having a length of 2.65 mm and angles of 70 degrees measured counterclockwise from the horizontal. They are placed so that fiber 1 is horizontally offset slightly to the right of fiber 2, and the majority of the enriched elements contain enrichments from both fibers. Case 2 contains fibers with lengths of 1.65 mm and 1.4 mm, with position angles of -20 degrees and -60 degrees, for fiber 1 and fiber 2, respectively. Fiber 2 is placed such that its center is approximately at the left tip of fiber 1. For case 3, fiber 1 has a length of 1.37 mm and a position angle of -45 degrees. Fiber 2 is positioned directly above fiber 1 with a length of 1 mm and a position angle of 15 degrees. Cases 2 and 3 fiber orientations are placed accordingly to investigate the response of fibers that are randomly oriented but contain elements that have enrichments from multiple fibers. In case 4, the right tip of fiber 1 and left tip of fiber 2 are placed close to each other. The fibers lengths are 1 mm and 0.83 mm and position angles are -23 degrees and 79 degrees for fiber 1 and fiber 2, respectively. The fibers in case 4 are placed so that the fiber tips from each fiber lie in the same element. All fibers are placed such that there are always elements that contain multiple fiber enrichments at each mesh discretization.

Uniform grids of 1,600 elements up to approximately 62,500 elements with corresponding element sizes of h=0.125 mm and 0.02 mm, respectively, were used in the discretization of the domain. The reference model consists of a very fine and non-uniform (to conform to the fiber domains) discretization, in which the fibers are explicitly modeled as two-dimensional solids.

The fiber domains are modeled using a very fine grid with an element size of approximately 1 μm. The reference model discretizations result in approximately 150,000 - 700,000 elements.

Figure 4.6 shows the absolute point-wise displacement errors of this model with respect to the reference simulation. Point-wise error was computed using the L2-norm for each case and plotted with respect to element size in the domain. Points A1 and A2 correspond to the left tips of fiber 1 and fiber 2, respectively. Points B1 and B2 are the right fiber tips of fiber 1 and fiber 2. Point C is the upper right corner of the matrix, and point D is the bottom right corner of the matrix. The six different point locations of interest are illustrated in Fig. 4.5a.

Figure 4.6a corresponds to case 1, when two fibers are parallel to each other. The errors showed monotonic convergence from the largest mesh size to the smallest mesh size. The largest error occurred in the left tip of fiber 2, while the lowest errors were in points C and D on the domain edge. All errors converged to less than 1% at the smallest mesh size of 0.02 mm. Case 2 errors are shown in Fig. 4.6b. Similar to case 1, there is monotonic convergence, with the largest error of the left fiber tip of fiber 2 and the smallest errors at points C and D. Case 3, shown in Fig. 4.6c, shows the same trend as in case 1 and case 2 errors. Point A2 however, has a larger error at the largest mesh size than the other cases, but converged to an error of approximately 1.5% at the smallest mesh size. Fig. 4.6d, displays monotonic convergence as well, with a slight variation in point B2 at the smallest mesh size. In all cases, the XFEM model for cases when elements are enriched by multiple fibers is in reasonable agreement with the reference simulation models which used the direct finite element method. As shown in Fig. 4.6, in all cases observed, the slope indicates approximately an order of magnitude decrease in error with order of magnitude reduction in element size.

4.4.2 Response of multiple fiber inclusions with progressive debonding

In this section, the four cases discussed in Section 4.4.1 for the elastic response are modeled with progressive debonding to capture the effect of the fiber-matrix interfacial separations.

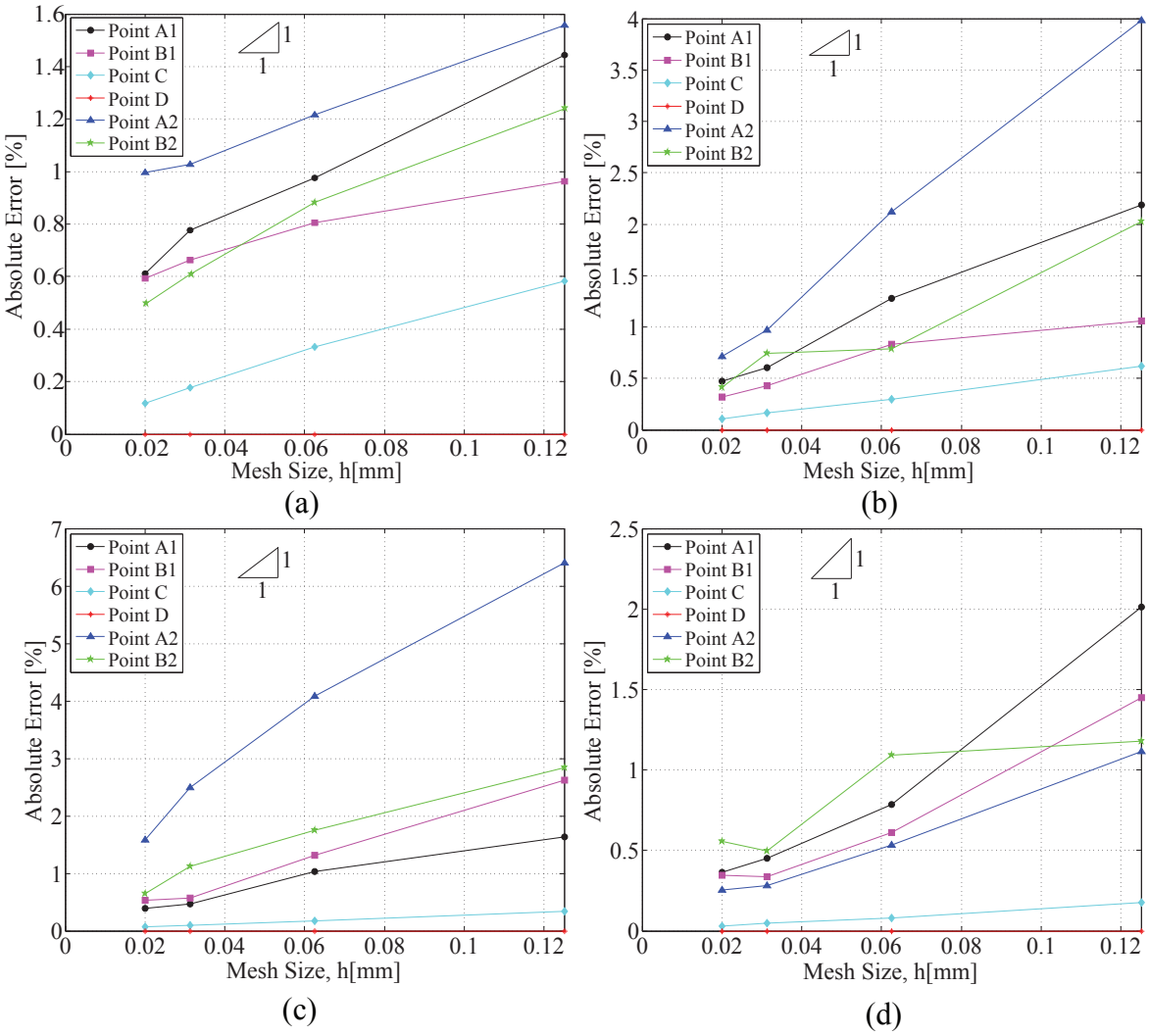

Figure 4.6: Point-wise error as function of mesh size for an elastic matrix; (a) case 1; (b) case 2; (c) case 3; and (d) case 4. A typical slope of order of magnitude error reduction with order of magnitude decrease of mesh size for the finite element method, is displayed by the legend for comparison.

The XFEM model is verified against the direct finite element method. The model domain, boundary conditions, matrix properties and fiber properties are taken to be the same as in Section 4.4.1.

To model the progressive debonding at the fiber-matrix interfaces, a bilinear cohesive zone law (defined in Eq. 3.24 and Eq. 3.25) is employed for both the XFEM and the reference simulations. The peak normal traction and normal cohesive characteristic separation length are set to 8 MPa and 0.01591 mm, respectively. The peak shear traction and shear cohesive characteristic separation length are 1.8 MPa and 0.01141 mm, respectively. The maximum cohesive separation length is taken as 0.08 mm under pure normal and pure shear loading [109, 115]. The reference model utilizes 1 μm wide cohesive zone elements that lay along the interface between the fiber and the matrix.

The absolute point-wise displacement error of this model with respect to the reference simulations is shown in Fig. 4.7. The displacement errors are computed for the same locations of interest in the previous section (points A1, A2, B1, B2, C and D), as well as the displacement jump between the matrix and fiber at each fiber center point.

In Figure 4.7a, case 1 is shown when the fiber-matrix interfaces have initiated the progressive debonding process but have not reached peak cohesive traction. There is a general trend toward convergence but with some variation at the smallest mesh sizes. The largest error occurred at the right tip of the first fiber, but was approximately 2.5% at the smallest mesh size. Points C and D have the lowest error, with both being under 0.1% for all mesh sizes. The errors of the displacement jumps at the center of both fibers were under 0.5% for all mesh sizes. Case 2 is shown in Fig. 4.7b, at the point of full fiber-matrix separation. At the point of full separation, the fiber and the matrix are completely debonded from each other at one side of the fiber and the interfacial tractions vanish. Similar to case 1, there is a trend of towards convergence with a slight variation at the smallest mesh sizes. All errors were at or below 2%. The center jump of fiber 1 produced the highest error at all mesh sizes, but monotonically converged.

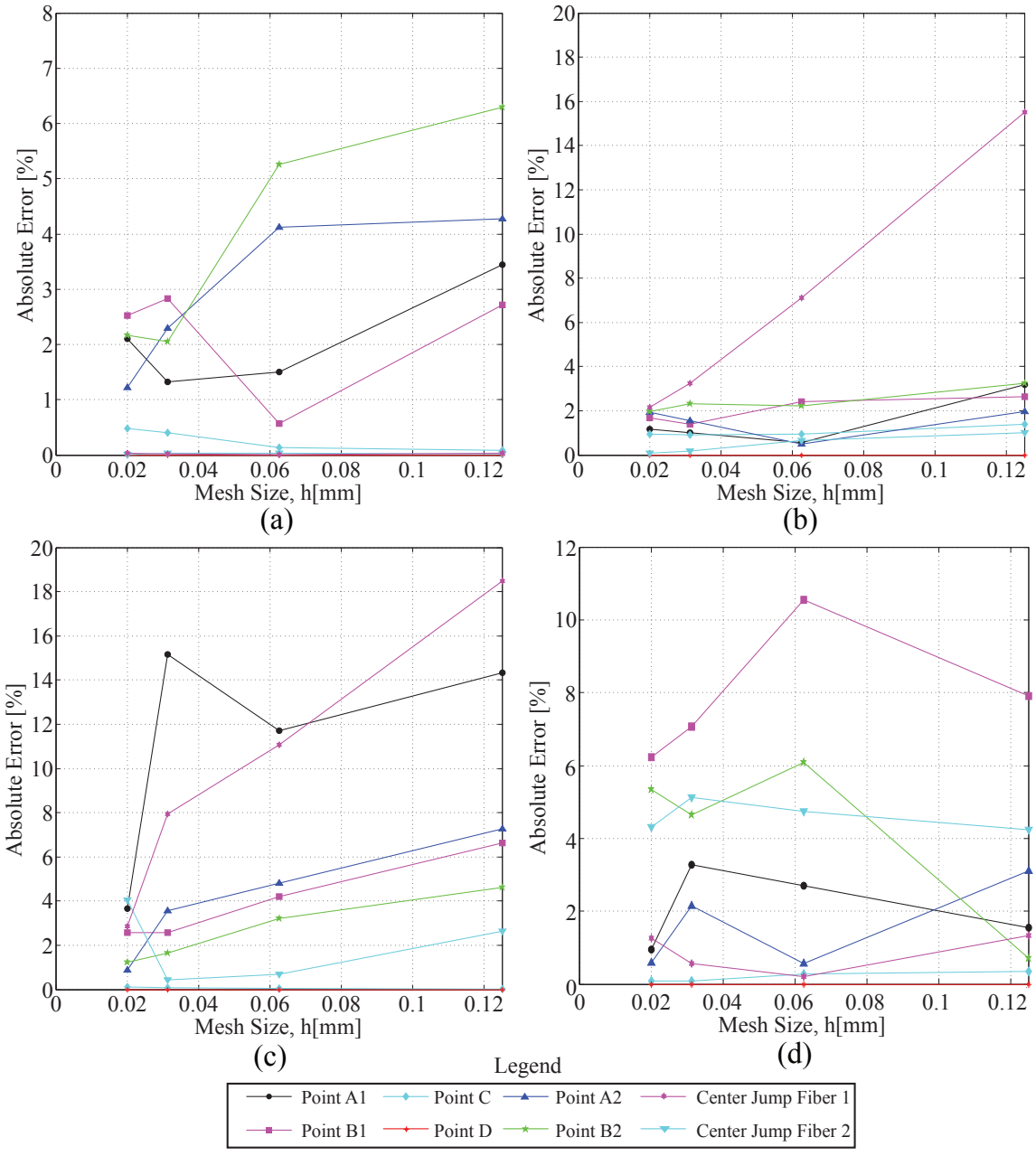

Figure 4.7: Point-wise error as function of mesh size for a matrix with progressive debonding; (a) case 1; (b) case 2; (c) case 3; and (d) case 4.

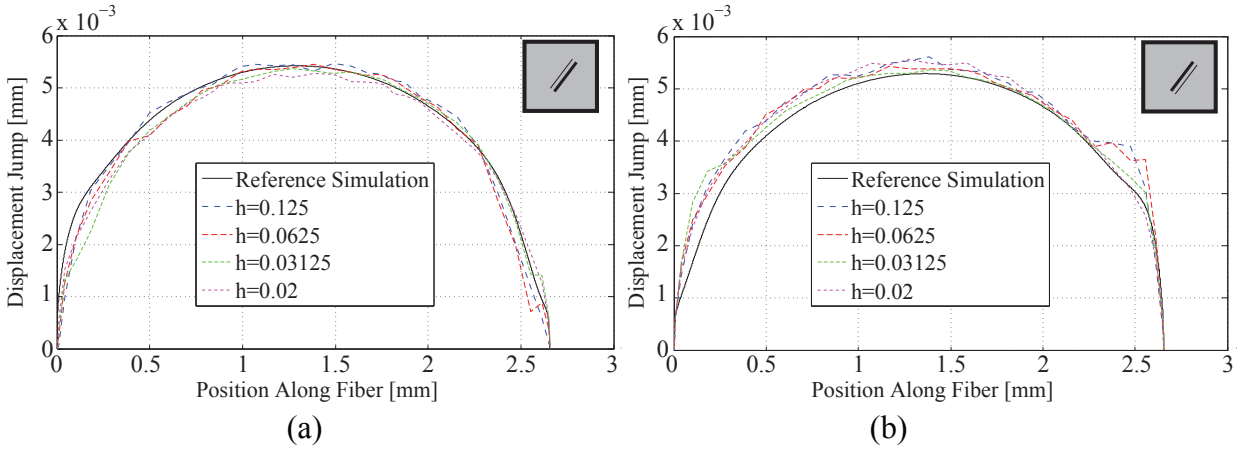

Figure 4.8: Displacement jump across the interface along the fiber length (h is the mesh size) for case 1: (a) fiber 1; and (b) fiber 2 .

The absolute point-wise errors are shown for case 3 and 4 in Fig. 4.7c and Fig. 4.7d, respectively. In case 3, the progressive debonding process has been initiated but has not reached peak cohesive traction. The left fiber tip and center jump of fiber 1 have larger errors than the rest of the points studied, but both have reasonable errors at the smallest mesh size. In case 4, the progressive debonding is past the point of peak cohesive traction but has not fully separated. In this case, there is variation in the monotonic convergence, but the point-wise error remained below 6% at each point for all mesh sizes, except for the right tip of fiber 1. The largest errors occurred in the right tips of fiber 1 and fiber 2, which both lie in the same doubly-enriched element. In all four cases studied with multiple fibers, there was not smooth monotonic convergence as observed in the purely elastic models, but general convergence with variation and mesh stability were observed for many of the cases. For all cases, reasonable errors were obtained at the smallest element size.

The magnitude of the displacement jumps associated with the fiber-matrix interfacial debonding along each fiber length for each case is plotted in Figs. 4.8-4.12. The XFEM model results are plotted for the four mesh sizes studied, ranging from 0.125 mm to 0.02 mm, along with the reference simulation. For each case, the XFEM model accurately capture the shape and magnitude of the reference curve, generally showing improved convergence as the element size decreases. While the general form of the debonding enrichment function

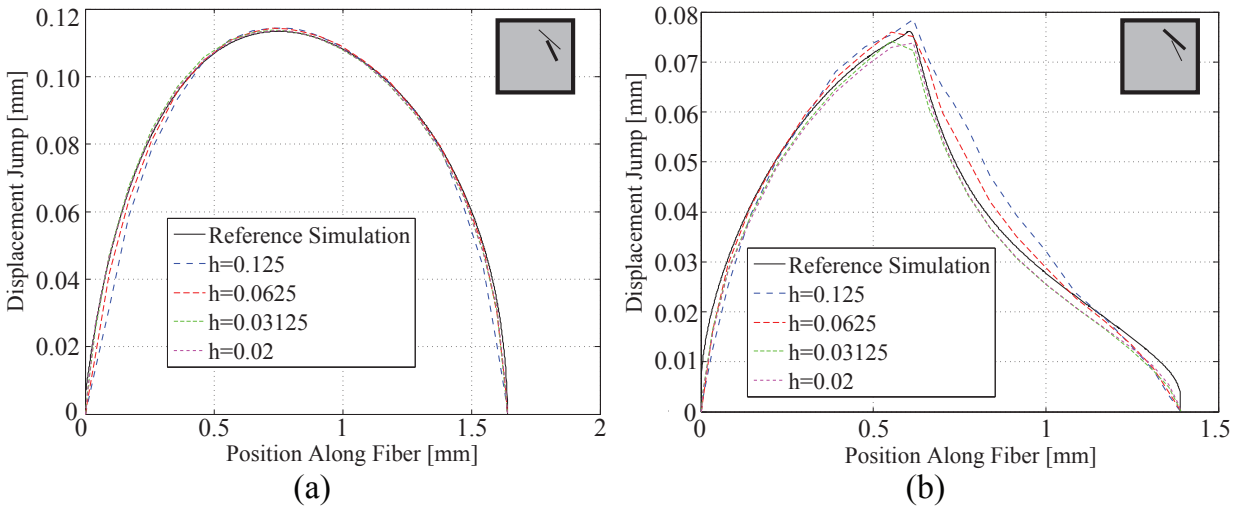

Figure 4.9: Displacement jump across the interface along the fiber length (h is the mesh size) for case 2: (a) fiber 1; and (b) fiber 2 .

is parabolic, asymmetry in the curve as inclusions in close proximity to each other begin to interact is well captured. In all cases, the normal displacement jump is larger than the tangential displacement jump and therefore governs the magnitude of the jump. Fiber tips are assumed to have no debonding in the XFEM and the reference simulations

In case 1 (Fig. 4.8), fiber 1 and fiber 2 exhibit approximately the same displacement jump curve in both shape and magnitude. All mesh sizes for case 1 show a reasonably accurate displacement jump profile with mesh stability. A slight kink is observed in the fiber 2 curve near the right end of the fiber, which becomes smoother and converges to the reference simulation as the mesh is refined. The deviation may be attributed to fiber 1 being located between fiber 2 and the applied load. When one fiber "blocks" another fiber from the applied load, the fiber may exhibit an irregular pattern of debonding. This phenomenon is more prominent in case 2 and case 3, in which each fiber is of different length and has a unique embedment angle. Figure 4.9 displays the displacement jumps for case 2. Fiber 1, which is above fiber 2, shows a parabolic displacement jump profile, with all four XFEM mesh sizes displaying high accuracy. Fiber 2, which is below fiber 1, shows an irregular displacement jump profile, which is due to having part of fiber 1 directly in front of it. The XFEM model accurately captures the irregular displacement jump profile along the fiber length for

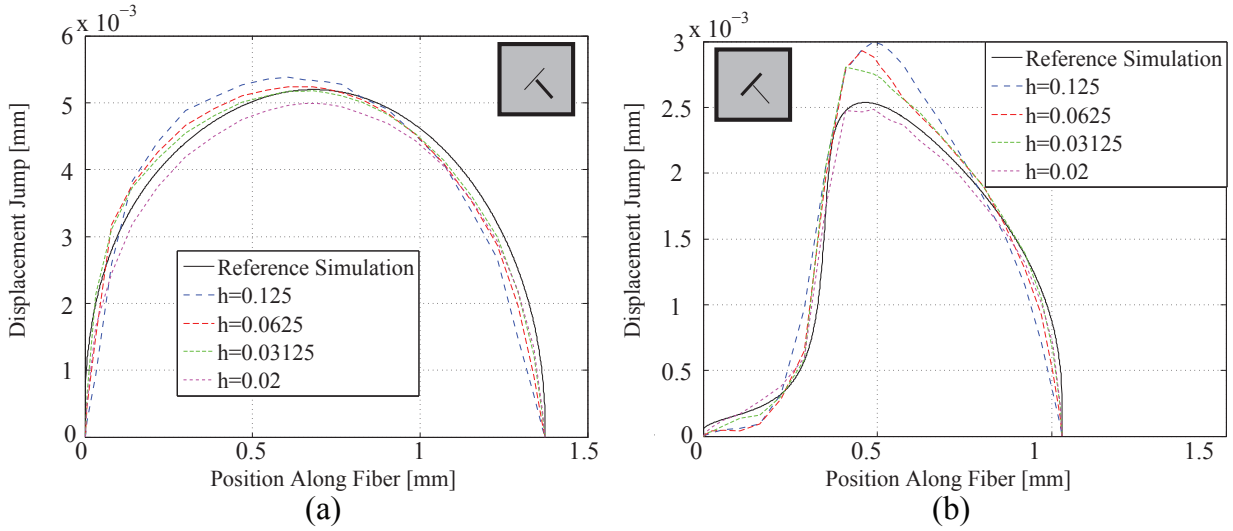

Figure 4.10: Displacement jump across the interface along the fiber length (h is the mesh size) for case 3: (a) fiber 1; and (b) fiber 2 .

all mesh sizes, with the smallest mesh most accurately representing the displacement jump. Figure 4.10 displays the displacement jumps for case 3. Similar to case 2, fiber 1 shows a parabolic displacement jump profile and fiber 2 shows an irregular displacement jump profile, which the XFEM model accurately represents. There is a reduction of the maximum displacement jump and convergence with the increase of mesh density observed in this case. Fig. 4.11 shows the deformed shape of the cohesive zone elements in the respective reference simulation for case 3, from which the displacement jump profile was obtained (deformation is significantly amplified for visualization purposes). Case 4 is shown in Fig. 4.12, with both fiber 1 and fiber 2 having roughly parabolic curves, with a slight asymmetry at the right end of each fiber, where the tips meet. Both displacement jump profile curves converged to the shape of the reference simulation as the mesh size was refined.

The lack of monotonic error convergence observed in Fig. 4.7 merits further discussion. Convergence issues in XFEM can be attributed to a variety of reasons including, but not limited to, the choice of enrichment functions, numerical integration, and partially enriched blending elements [48]. In this chapter, the lack of monotonic error convergence can be attributed to the limitation of the fiber-matrix debonding enrichment function in representing

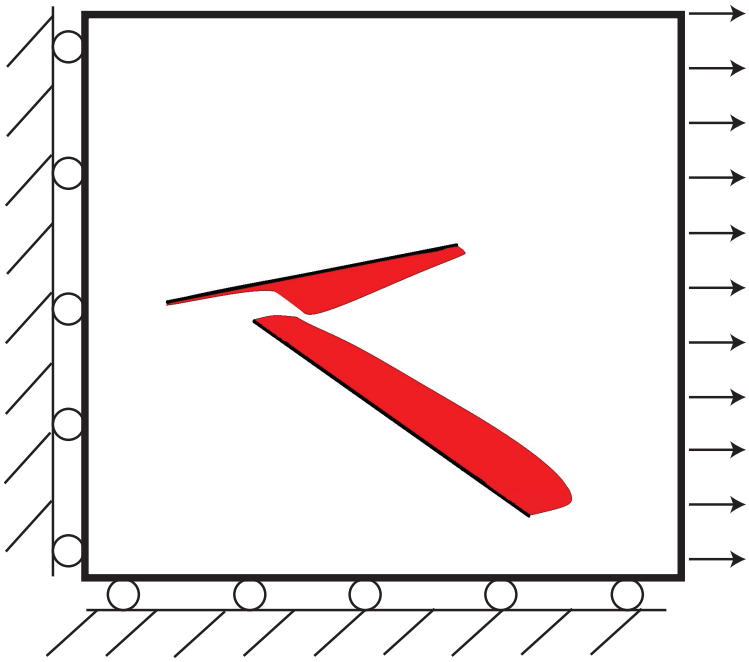

Figure 4.11: Case 3 reference simulation for progressive debonding between fibers and matrix. Shaded area denotes the displacement jump measured from the cohesive elements, plotted in Fig. 4.10. Deformation is amplified for visualization purposes.

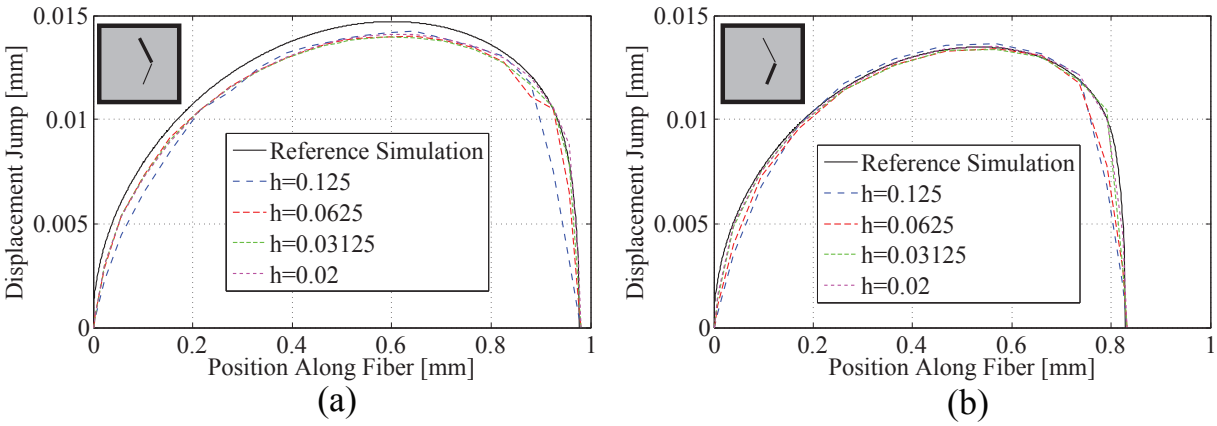

Figure 4.12: Displacement jump across the interface along the fiber length (h is the mesh size) for case 4: (a) fiber 1; and (b) fiber 2 .

true debonding profile, as well as the way the enriched element domains (and hence the integration accuracy as discussed above) change as the mesh is refined. In case 1, the right tips of fiber 1 and fiber 2 are in the same element at element lengths of h=0.125 and 0.0625 mm, but in different elements at meshes of higher resolution. Thus with a coarse mesh, fiber tip error is computed from a doubly enriched fiber tip element, whereas at fine meshes, the fiber tip error is computed from a tip-enriched element that is partially enriched by the other fiber. In each case, as the mesh is refined, the location of the inclusion with respect to the element edges changes. The spatial alignment of inclusions within an element influences the Delaunay triangulation of the element, which can introduce inconsistencies in the element integration as the size of the element domain changes. 3 Gauss points were used for the integration of each triangular sub domain for the results shown here for the proposed XFEM models. Several simulations were conducted using 6 Gauss points per sub domain but computational cost increased significantly while the measured errors did not improve significantly. Overall, the XFEM model with progressive fiber-matrix interfacial debonding provided an accurate representation of the displacement jump curves obtained from the reference simulations and was capable of predicting the displacement jumps for a variety of scenarios in which fibers were arbitrarily placed in close proximity to each other and contained elements with multiple enrichments. Absolute point-wise error was higher than the purely elastic case, but reasonable mesh stability was observed and errors remain within an acceptable range for each case at a sufficiently fine mesh.

Table 4.1 compares the model size of the reference simulation of progressive debonding of case 1 (Fig. 4.5b (i)) with the XFEM simulations for the same case. The number of elements, standard nodes, total nodes and total degree of freedoms (DOFs) associated with each model are displayed. The largest number of elements and DOFs are 62,500 and 130,194, respectively for the finest mesh. The total DOFs of the finest XFEM mesh are smaller by approximately an order of magnitude compared to the reference simulation.

	Reference Model	XFEM			
		h=0.125	h=0.0625	h=0.03125	h=0.02
Number of Elements	601,236	400	6,400	25,600	62,500
Number of Standard Nodes	601,427	1,681	6,561	25,921	63,001
Number of Total Nodes	601,427	2,051	7,255	27,269	65,097
Number of Total DOFs	1,202,854	4,102	14,510	54,538	130,194

Table 4.1: Problem size comparison for debonding case 1.

4.4.3 Progressive debonding interactions of four fiber inclusions

The performance of the XFEM model for the progressive debonding response is investigated for a four fiber inclusion case when the inclusions are in close proximity of each other, but not touch or overlap. The fibers are placed, such that various elements in the domain may contain up to three fiber inclusions, for all mesh sizes studied. The model domain, boundary conditions, matrix properties and fiber properties are taken to be the same as in Section 4.4.1. The cohesive law used for the progressive debonding at the fiber-matrix interfaces is the same used in Section 4.4.2.

The case consisting of four fiber inclusions, contains fibers which are in close proximity to each other as illustrated in Fig. 4.13. Fiber 1 is located in the center of the domain between three other fibers, with a length of 2.34 mm and an angle of 38 degrees measured counterclockwise from the horizontal. Fiber 2 is measured at a length of 0.9 mm and an angle of -54 degrees. Fiber 3 is placed so that the right tip of fiber 3 lies in the same element at the left tip of fiber 2 and the domain of fiber 1. The lengths and angles of fibers 3 and 4 are 1.25mm, -27 degrees and 1.62 mm, 58 degrees, respectively.

The fiber-matrix interfacial progressive debonding displacement jumps are illustrated in Fig. 4.14. The interaction responses between the fibers are captured with the displacement jump of each fiber, along the fiber length. Mesh sizes ranging from 0.125 mm to 0.02 mm are considered. For fiber 1 and fiber 4, the progressive debonding is past the point of peak cohesive traction but has not fully separated. In fiber 2 and fiber 3, the progressive debonding process has been initiated but has not reached peak cohesive traction. Figure 4.14 displays

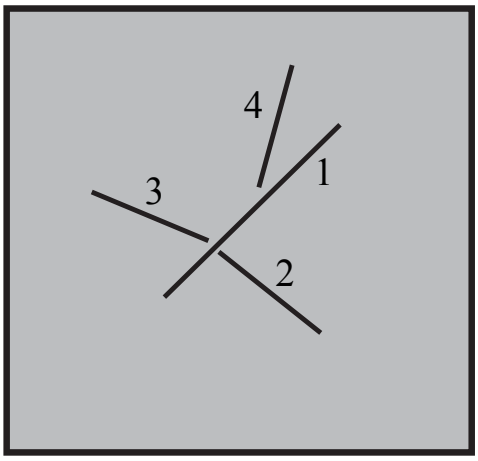

Figure 4.13: Fiber configuration of four fiber inclusions interaction case.

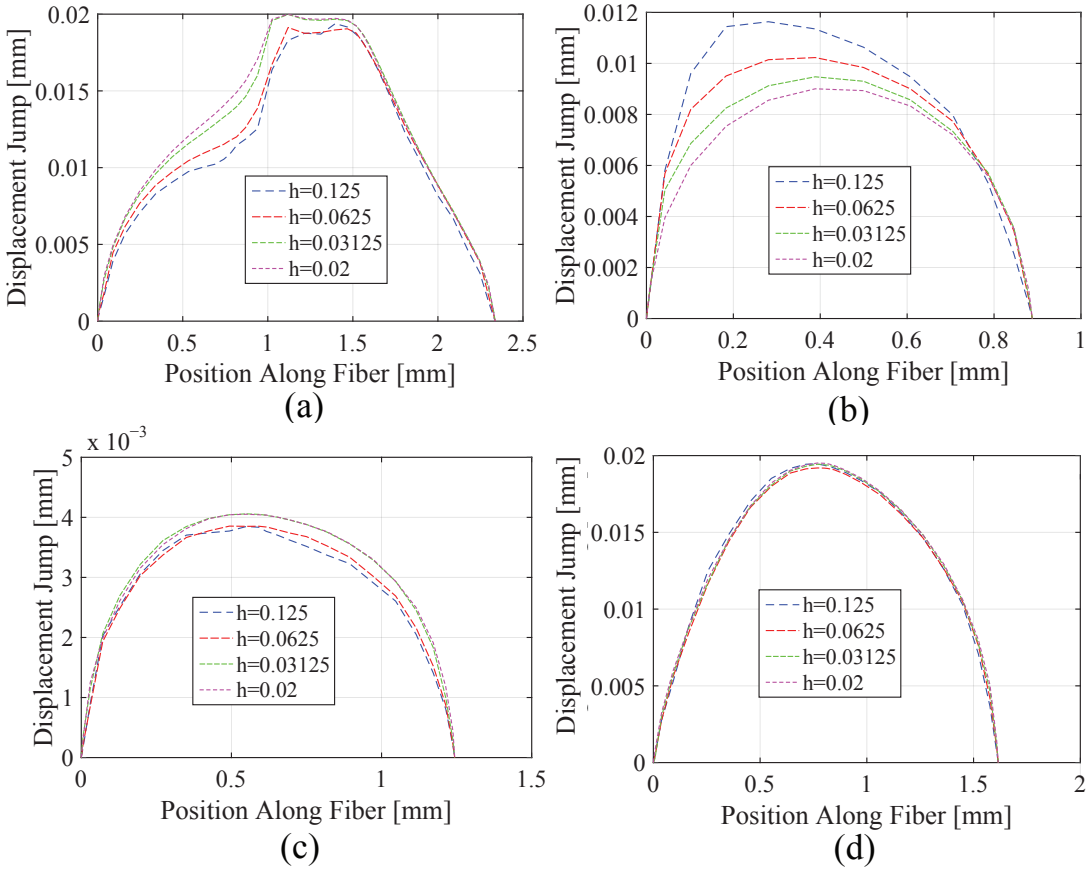

Figure 4.14: Displacement jump across the interface along the fiber length (h is the mesh size) for the four fiber configuration case: (a) fiber 1; (b) fiber 2; (c) fiber 3; and (d) fiber 4.

the shape and magnitude of the displacement jumps for each of the four fibers, showing convergence as the element size decreases. Each of the fiber displacement jumps do not exhibit a perfect parabola, but show an asymmetric displacement jump profile due to the interactions from the close proximity of each of the fibers.

The displacement jump profile for fiber 1, illustrated in Fig. 4.14a, exhibits an irregular jump profile. The irregular displacement jump profile is due to the having part of fiber 2 in front of it, as well as the tips from fibers 3 and 4 on the left side of the fiber domain. The peak displacement jump occurs at the midpoint of the fiber. Figure 4.14b displays an asymmetric displacement jump profile jump of fiber 2, with the peak occurring left of the fiber midpoint. Fibers 3 and 4 display a parabolic shaped displacement jump profile represented in Fig. 4.14c and Fig. 4.14d, respectively. Each of the fiber displacement jump profiles exhibited mesh convergence with the decrease in mesh size.

4.4.4 Progressive debonding of a dense fiber domain

In this section, investigation of a dense fiber domain is performed with the proposed XFEM model for the progressive debonding response. 50 fibers are randomly placed in a 10 mm by 10 mm domain with the fibers having a mean length of 1.3 mm ($\pm$ 0.2 mm), as displayed in Fig. 4.15. With the random dispersion of fibers, multiple elements have multiple fiber enrichments in them. The mesh size is h=1 mm in this example. The boundary conditions, matrix properties and fiber properties are taken to be the same as in Section 4.4.1. The cohesive law used for the progressive debonding at the fiber-matrix interfaces is the same used in Section 4.4.2.

The displacement jumps between the fiber and the matrix for each of the fibers are summarized in Fig. 4.16. Fig. 4.16a displays the number of fibers for their respective maximum magnitude of separation of the displacement jumps. 2 fibers resulted in a maximum interface separation of less than 0.01 mm while there were 19 fibers for a maximum separation between 0.01-0.25 mm as well as 0.025-.05 mm. 9 fibers showed maximum separation be-

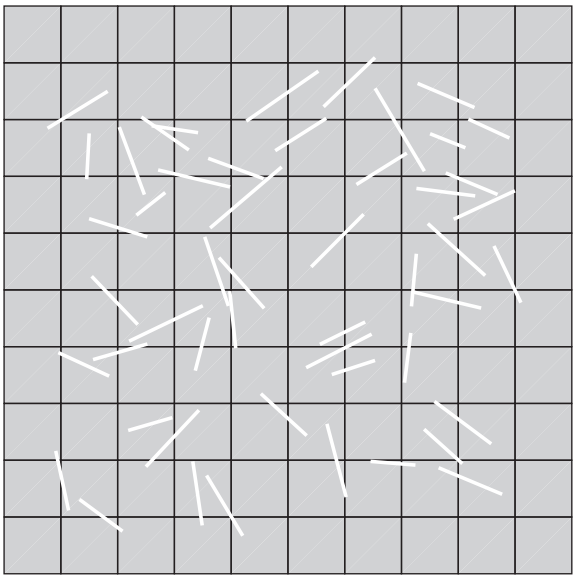

Figure 4.15: Dense fiber domain case.

tween 0.05-.075 mm, and a single fiber showed an interface separation greater than 0.075 mm with complete loss of interfacial cohesion. For the 50 total fibers in the domain, 5 did not separate (i.e. maximum separation less than the characteristic separation length), 44 fiber matrix interfaces were partially debonded and only 1 fiber matrix interface had a maximum separation that resulted in complete separation. Fig. 4.16b displays the severity of debonding.

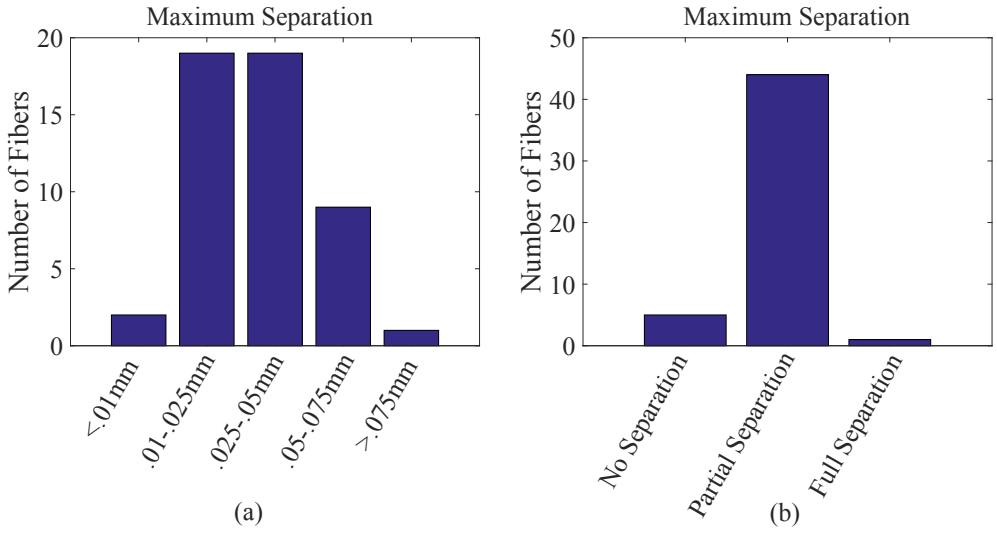

Figure 4.16: Summary of displacement jumps for the fibers in the dense fiber domain: (a) total number of fibers with their respective maximum separation of each displacement jump; (b) total number of fibers with no separation, partial separation and full separation.

CHAPTER 5

3D XFEM MODELING OF SHORT FIBER REINFORCED COMPOSITES

5.1 Introduction

This chapter presents an XFEM approach to model short fiber composites in three dimensions. The ideas and formulations from the XFEM approach in the previous chapters for two dimensions, are built upon to address short fiber composites in three dimensions. Fibers are represented as two dimensional elastic deformable planar rectangles with progressive debonding on the fiber matrix interface and investigated for single and multiple fiber domains. The work in this chapter will be reflected in a paper currently in preparation.

The approach in three dimensions for XFEM creates additional challenges and difficulty as compared to two dimensions. The work in three dimensions is not as prevalent as work in two dimensions, but a brief review of literature for XFEM in three dimensions is provided for reference.

XFEM modeling in three dimensions has been used to model crack propagation in the domain. Sukumar et al. [102] presented a methodology using discontinuous functions to add a two dimensional asymptotic crack-tip displacement field in the finite element approximation, and built upon their work in [103] for a fast marching method for fatigue crack propagation. Work on three dimensional dynamic crack propagation in a GFEM setting was proposed by Duarte et al. [33]. Additional work for three dimensional cracks within the GFEM/XFEM method has been presented, [49, 55, 70, 73, 119], amongst others. XFEM application using commercial software in 3-D for damage modeling of fiber reinforced composites has also been investigated [108].

To account for internal geometries in a three dimensional domain, Duarte et al. [32], developed an approach using the GFEM method for modeling complex geometries. Additional approaches for modeling internal geometries in three dimensions have also been presented.

Modeling of three dimensional woven fibers using the XFEM method was developed by Moës et al. [71]. The modeling of cylindrical fibers using the GFEM method has been proposed by Soghrati and Geubelle [100]. Oswald et al. [79] developed an approach to model carbon nanotube and thin films based on the XFEM method.

In this chapter, a three dimensional XFEM model is presented for short fibers in composites. In a three dimensional setting, high aspect ratio fibers are modeled as two dimensional planar rectangular inclusions. The fibers are taken to be elastic and deformable in the axial direction which is the dominant deformation mechanism for short fibers embedded in a matrix domain. Fiber and debonding enrichment functions are presented to account for the presence of the fibers within the composite domain and to idealize the progressive debonding on the fiber-matrix interfaces The capabilities of the XFEM model is verified against the direct finite element method and the performance of the model predictions is assessed. The computational strategy investigates the influence of the rotation of the fiber interface and evaluation of a problem with a significant amount of fiber inclusions.

The remainder of this chapter is organized as follows. In Section 5.2, the XFEM method for a three dimensional domain is presented. Section 5.3 provides the governing equations and model formulation. Section 5.4 reviews the computational formulation and numerical integration. Numerical verification studies to assess the performance of this approach are presented in Section 5.5.

5.2 Three Dimensional XFEM

Short fibers in a three dimensional XFEM domain are modeled as two dimensional objects in this chapter. Fibers are taken to have high aspect ratios with $l >> w >> t$, where l, w, and t denote length, width and thickness of the fiber respectively (Fig. 5.1). Fibers of such geometry are employed in [5, 83, 84]. Other work utilizing rectangular short fibers has also been performed in Refs. [1, 47, 61, 78, 117]. Considering no twisting, the fibers are defined by four corner points and edges of the thin rectangle, which forms the plane of the fiber.

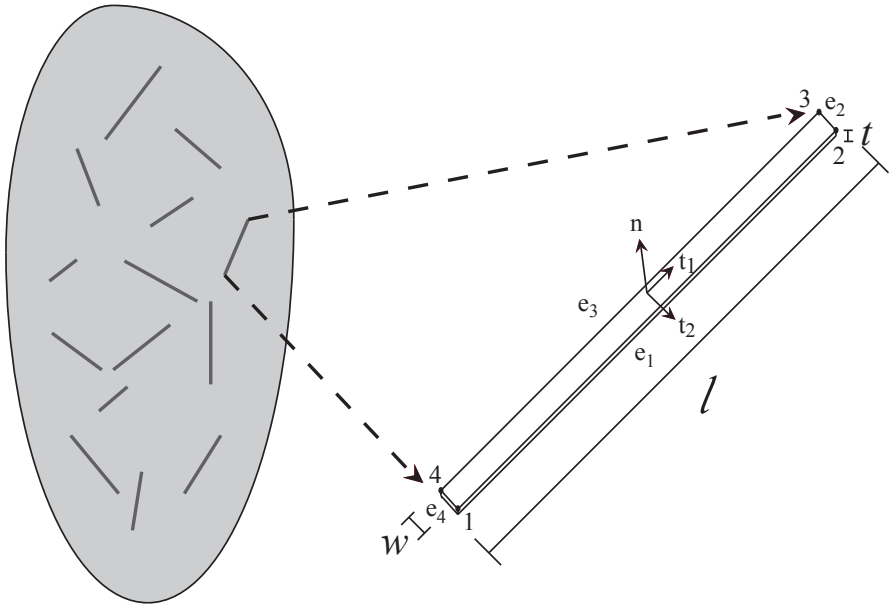

Figure 5.1: Two dimensional fiber domain represented in a three dimensional domain.

Fibers are modeled as two dimensional inclusions due to the fibers having a high aspect ratio and the need to have an interface for progressive debonding to occur on, rather than modeling the fibers with a high computational cost as 3-D inclusions.

The three dimensional XFEM discretization is modified from a two dimensional discretization (Eq. 4.1), to account for two dimensional fibers for the displacement field for a domain reinforced by one or multiple short fiber inclusions:

$$\mathbf{u}(\mathbf{x},t) = \sum_{a=1}^{n_n} N_a(\mathbf{x})\hat{\mathbf{u}}_a + \sum_{\alpha=1}^{n}\left[\sum_{b=1}^{n_{\text{en}}^{\alpha}} N_{\mathcal{I}_b^{\alpha}}(\mathbf{x})\psi_{\alpha}^{p}(\mathbf{x})\hat{\mathbf{c}}_{b\alpha}\right] + \sum_{\alpha=1}^{n}\left[\sum_{c=1}^{n_{\text{en}}^{\alpha}} N_{\mathcal{I}_c^{\alpha}}(\mathbf{x})\Upsilon_{\alpha}^{p}(\mathbf{x})\hat{\mathbf{d}}_{c\alpha}\right] \tag{5.1}$$

similarly as in 2-D, the displacement field is denoted as $\mathbf{u}$; the space and time coordinates are $\mathbf{x}$ and t, respectively; n_n the total number of mesh nodes in the finite element discretization; n is the number of fibers, n_{en}^{α} is the number of enriched nodes for fiber α; N_a, the standard finite element shape function associated with node a; $\hat{\mathbf{u}}_a$, $\hat{\mathbf{c}}_{b\alpha}$ and $\hat{\mathbf{d}}_{c\alpha}$ the nodal coefficients of the standard, fiber enrichment and debonding enrichments for each fiber α, respectively; $\mathcal{I}^{\alpha}$ is the index set of enriched nodes for fiber α; $\mathcal{I}_a^{\alpha} \in \mathcal{I}^{\alpha}$ the index of an enriched node, a; the fiber enrichment function and the debonding enrichment function are different for each

2-D fiber, α, denoted as ψ_{α}^{p} and Υ_{α}^{p}, respectively.

The first right hand side term in Eq. 5.1 represents the standard finite element approximation of the response field. The second term represents the presence of the 2-D planar fiber within the domain, in which the strain discontinuity in the approximation space is a function of the fiber enrichment function, ψ_{α}^{p}. The third term corresponds to the separation between the fiber face and the matrix due to the progressive loss of the cohesive bond, which is a function of the debonding enrichment function,Υ_{α}^{p}

5.2.1 Fiber enrichment function

The enrichment function in two dimensions for short fiber inclusions was developed to represent fibers as 1-D line segments, and was previously discussed in early chapters. In this chapter, the high aspect ratio fibers are modeled as 2-D planar rectangles. The enrichment function to approximate this type of fiber is addressed in this section, which is expressed in terms of level set functions associated with fibers edges and body.

The reinforcing fiber is taken to be entirely embedded in the open bounded domain of the three dimensional composite body, Ω, where $\Omega \subset \mathbb{R}^3$. The level set associated with the plane of the fiber α, $\phi_f(\mathbf{x})$, is expressed as:

$$\phi_f(\mathbf{x}) = \hat{\mathbf{n}}_{\alpha} \cdot (\mathbf{x} - \mathbf{x}_c) \tag{5.2}$$

where $\hat{\mathbf{n}}_{\alpha}$ is the normal vector to the fiber and $\mathbf{x}_c$ is a reference point on the plane of the fiber, set to the center of the fiber. ϕ_f divides the domain along the plane of the fiber and is defined as the signed distance function, with zero value on the fiber plane. The level set functions for the fiber edges, e, are expressed as:

$$\phi_e(\mathbf{x}) = (\mathbf{x} - \mathbf{x}_{p_{e1}}) \cdot \mathbf{t}_e; \quad e = e_1, e_1, e_2, e_3, e_4 \tag{5.3}$$

in which, e represents the fiber edge, $\mathbf{t}_e$ denotes the tangent at the fiber edge, $\mathbf{x}_{p_{e1}}$ is a end

point on the fiber edge, e (i.e. fiber corner point). ϕ_e provides the zero level set along the plane normal to the fiber edge, e, with positive values on one side of the domain cut by ϕ_e and negative elsewhere in the domain.

The level set functions from Eqs. 5.2 and 5.3 are used to expressed the enrichment function for the fiber:

$$\psi_\alpha^p(\mathbf{x}) = \left[\prod_{e=1}^{4} H(-\phi_e)\right] |\phi_f|(\mathbf{x}) + \sum_{\lambda=1}^{4}\left[\sum_{e=1}^{4} H(\phi_e)H(\phi_{e_{+1}})\right] d_\lambda(\mathbf{x}) + \sum_{e=1}^{4}\left[H(\phi_e)\prod_{e_s=1}^{3} H(-\phi_{e_s})\right] d_e(\mathbf{x}) \quad (5.4)$$

where, $d_\lambda(\mathbf{x}) = \|\mathbf{x} - \mathbf{x}_\lambda\|$ denotes the distance to the fiber corner, λ; e_{+1} is the subsequent adjacent fiber edge to edge e (i.e. $e_{+1} = e_2, e_3, e_4, e_1$); e_s denotes edges that are not edge e ($e_s = e_t | e_t \neq e$ and $e_t = \{e_1 : e_4\}$ is the set of all edges). The level set function associated with edges e_{+1} and e_s are described with the same fiber edge level set function ϕ_e , where for associated edge i the function is taken as: $\phi_i(\mathbf{x}) = (\mathbf{x} - \mathbf{x}_{p_{e1}}) \cdot \mathbf{t}_i$

The distance to the fiber edge is expressed as:

$$d_e = \frac{\|(\mathbf{x}_{p_{e2}} - \mathbf{x}_{p_{e1}}) \times (\mathbf{x}_{p_{e1}} - \mathbf{x})\|}{\|\mathbf{x}_{p_{e2}} - \mathbf{x}_{p_{e1}}\|} \quad (5.5)$$

in which, $\mathbf{x}_{p_{e1}}$ and $\mathbf{x}_{p_{e2}}$ are the end points on fiber edge, e.

The enrichment function is displayed in Fig. 5.2a for a randomly placed short fiber in a three dimensional domain, where the value of the enrichment function increases from blue (zero) to red (highest). Cross sectional contours of the enrichment function are shown in Figs. 5.2b-c. Similarly to the fiber enrichment function, ψ_α, the 3-D enrichment function, ψ_α^p, incorporates a strain discontinuity mode along the fiber position and the displacements around the fiber can therefore be accurately captured without explicitly discretizing the fiber domain. The form of Eq. 5.4 for the enrichment function ensures that the approximation basis captures the strain discontinuity but stays smooth otherwise around the sides and

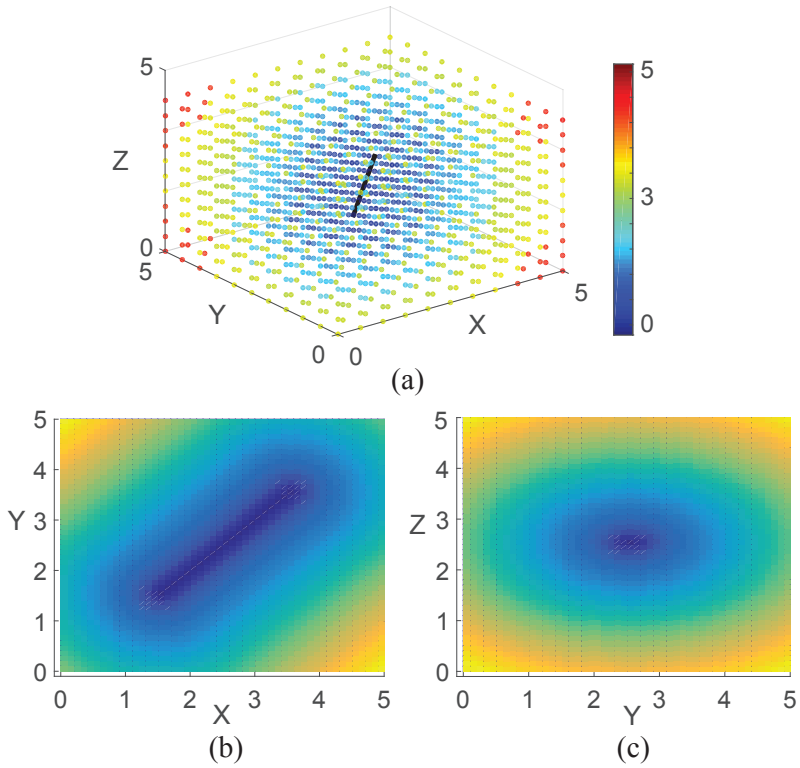

Figure 5.2: Short fiber inclusion enrichment function for three dimensions. Blue represents values close to 0 and red represented the highest value: (a) three dimensional view with the black line representing the fiber; (b) fiber enrichment values in the X-Y plane; (c) fiber enrichment values in the Y-Z plane.

face of the fiber. Except for the domain of the fiber, the enrichment function is nonzero everywhere in the composite domain.

5.2.2 Debonding enrichment function

The level set functions for the fiber body and edges described in the previous section are used to define the debonding enrichment function, Υ_α^p. The debonding enrichment function describes the debonding between the fiber and the matrix and introduces a strong discontinuity in the displacement field.

To model the shape of the debonding at the fiber and matrix interface in three dimensions, a Heaviside function is used to represent the physical separation in the normal direction and both tangential directions. Unlike, the previously developed debonding enrichment function (3.5) for two dimensions, the ends of the fibers allow debond in all directions. Progressive

deonding occurs on the interface between the fiber and matrix, which is represented as a 2-D thin rectangular. The debonding enrichment function for the fiber is then expressed in terms of discontinuity functions as:

$$\Upsilon_{\alpha}^{p}(\mathbf{x}) = H(\phi_f)\left(\prod_{e=1}^{4} H(-\phi_e)\right) \tag{5.6}$$

5.3 Governing Equations and Computational Formulation

The governing equations and model formulation in 3-D follows similarly to the governing equations and model formulation outlined in the previous chapters for a 2-D domain, with minor differences. In this section, governing equations and model formulation are presented for three dimensional domain for short fiber composites.

The mechanical equilibrium and exterior boundary conditions within the 3-D domain are the same as in 2-D and are expressed in Section 2.4 in Eq. 2.10-2.13, respectively. All fibers, as well as the matrix, are assumed to remain elastic under the applied loading and only quasi-static response is considered. The matrix is not taken to progressively damage under applied loading and therefore continuum damage mechanics are not utilized in this chapter.

The fiber-matrix interface traction continuity for the two dimensional interface can be expressed in Eq. 3.6. The continuity follows the same form, but it is a function of the normal and both tangential tractions ($\boldsymbol{T} = \boldsymbol{T}(T_n, T_{t_1}, T_{t_2})$). A cohesive law describing the relationship between surface traction and separation represents the physical deterioration occurring at the fiber-matrix interface. A bilinear cohesive law is considered in all three directions(n, t_1, t_2) and follow the same form in three dimensions in two dimensional the equations expressed in Eq. 3.24 and Eq. 3.25.

Within a three dimensional domain, a matrix is reinforced by n, two dimensional planar fibers, with length, width and thickness of a fiber, α, denoted as l_α, w_α and t_α, respectively, where the fibers are randomly distributed within the domain. The aspect ratios are taken

to be small (i.e., $t_\alpha/l_\alpha \ll 1$ and $t_\alpha/w_\alpha \ll 1$). To develop the weak form of the model from Eqs. 2.10-2.13 and Eq. 3.6, standard procedures are used and the weak form can be found in Eq. 3.8.

Due to the assumption that the fibers are embedded in the domain, have high aspect ratios and are assumed to have uniform tractions along the fiber, the stress that develops in the fiber is axial. This assumption is verified using direct finite element simulations where the fiber is resolved with highly resolved meshes. No significant shear stress or bending moment develops within the domain of the fiber. Assuming that the fiber aspect ratio between the width and the length is high, the axial stress is uniform across the width of the fiber and can be approximated at the center of the fiber. The axial stress is expressed as:

$$\boldsymbol{\sigma} = \sigma_f^\alpha(s)\boldsymbol{t}_{\alpha c} \otimes \boldsymbol{t}_{\alpha c} \tag{5.7}$$

where $\boldsymbol{t}_{\alpha c}$ is the tangent vector along the length of the fiber at the two center points of the width. The second term in Eq. 3.8 becomes:

$$\int_{\Omega_\alpha} \boldsymbol{\sigma} : \delta\boldsymbol{\epsilon}\, d\Omega \;\simeq\; A_{f\alpha} \int_{\Omega_\alpha} \sigma_f^\alpha \delta\epsilon_f^\alpha \, d\Omega \tag{5.8}$$

where, $\delta\epsilon_f^\alpha = \delta\boldsymbol{\epsilon} : \boldsymbol{t}_{\alpha c} \otimes \boldsymbol{t}_{\alpha c}$ and $A_{f\alpha}$ is the cross sectional area of the fiber. The axial stress in fiber α, is taken to be proportional to the axial strain (i.e., $\sigma_f^\alpha = E_f\epsilon_f^\alpha$), where E_f is the elastic modulus of the fiber. Bending deformation is not accounted for in this chapter, due to numerous simulations using the standard finite element for randomly oriented high aspect ratio short fibers in a three dimensional domain, subject tensile loading resulting in insignificant bending deformation along its length.

Under the condition that aspect ratios of the fibers are very high, we assume that tractions

along the two opposing faces of a fiber in the thickness direction are uniform:

$$\boldsymbol{T}^{+}(s)\cdot\boldsymbol{n}^{+}\Big|_{\Gamma_\alpha^{+}}-\boldsymbol{T}^{-}(s)\cdot\boldsymbol{n}^{-}\Big|_{\Gamma_\alpha^{-}}=0;\quad \boldsymbol{T}^{+}(s)\cdot\boldsymbol{t}_1^{+}\Big|_{\Gamma_\alpha^{+}}-\boldsymbol{T}^{-}(s)\cdot\boldsymbol{t}_1^{-}\Big|_{\Gamma_\alpha^{-}}=0;$$
$$\boldsymbol{T}^{+}(s)\cdot\boldsymbol{t}_2^{+}\Big|_{\Gamma_\alpha^{+}}-\boldsymbol{T}^{-}(s)\cdot\boldsymbol{t}_2^{-}\Big|_{\Gamma_\alpha^{-}}=0 \quad (5.9)$$

The fiber domain is Ω_α, s is a position along the fiber face, fiber normal $\boldsymbol{n}_\alpha$, and fiber tangent vectors, $\boldsymbol{t}_{1\alpha}$ and $\boldsymbol{t}_{2\alpha}$, respectively. Similarly in two dimensions, debonding along the two faces of a fiber would typically occur concurrently for a short fiber embedded in a matrix under the traction conditions. However, the fiber-matrix debonding is likely to initiate at a weak spot at one face of the fiber. Upon complete debonding at the weak face, the tractions along the opposing (unbonded) face relax. The third term in the weak form (Eq. 3.8) models the progressive debonding process between the fiber and the matrix.

The weak form of the governing equation for high aspect ratio fiber composites can be express as:

$$\int_\Omega \boldsymbol{\sigma} : \delta\boldsymbol{\epsilon}\, d\Omega + \sum_{\alpha=1}^{n} A_{f\alpha}E_f \int_{\Omega_\alpha} \epsilon_f^\alpha \delta\epsilon_f^\alpha \, d\Omega + \sum_{\alpha=1}^{n}\int_{\Gamma_\alpha} \boldsymbol{T}\cdot\delta[\![\mathbf{u}]\!]\, d\Gamma - \int_{\Gamma_t}\tilde{\mathbf{t}}\cdot\delta\mathbf{u}\, d\Gamma = 0 \quad (5.10)$$

The domain of the matrix is taken to occupy the entire domain, since the domains of the fibers are computed are vanishingly small. Therefore, the limits of the integral of the first term in the weak form is set to Ω.

5.4 Computational Formulation and Implementation

To discretize and evaluate the governing equations, XFEM is employed. The computational formulation is updated from previous chapters for a 3-D formulation. Much of the formulation is unmodified from 2-D to 3-D, but it is referenced for completeness. The weak form of

the governing equation (Eq. 5.10) is written in the matrix form as:

$$\int_{\Omega} \delta\boldsymbol{\epsilon}^T \boldsymbol{\sigma}\, d\Omega - \int_{\Gamma_t} \delta\mathbf{u}^T \tilde{\mathbf{t}}\, d\Gamma + \sum_{\alpha=1}^{n} A_{f\alpha} E_f \int_{\Omega_\alpha} \epsilon_f^\alpha \delta\epsilon_f^\alpha\, d\Omega + \sum_{\alpha=1}^{n} \int_{\Gamma_\alpha} \delta[\![\mathbf{u}]\!]^T \boldsymbol{T}\, d\Gamma = 0 \tag{5.11}$$

The Bubnov-Galerkin approach is used to discretize displacement field of Eq. 5.1 and the discretization of the test function uses the same shape functions as the trial function. The first term in Eq. 5.11 follows the same approach in two dimensions and is outlined Section 3.4.

The gradient terms for the gradient vector $\mathbf{B}^e$, outlined Section 3.4 are expressed in 3-D as:

$$\hat{\mathbf{B}}_a^e = \begin{bmatrix} N_{a,x}^e & 0 & 0 \\ 0 & N_{a,y}^e & 0 \\ 0 & 0 & N_{a,z}^e \\ N_{a,y}^e & N_{a,x}^e & 0 \\ 0 & N_{a,z}^e & N_{a,y}^e \\ N_{a,z}^e & 0 & N_{a,x}^e \end{bmatrix}; \; \bar{\mathbf{B}}_a^e = \begin{bmatrix} (N_a^e \psi_\alpha^p)_{,x} & 0 & 0 \\ 0 & (N_a^e \psi_\alpha^p)_{,y} & 0 \\ 0 & 0 & (N_a^e \psi_\alpha^p)_{,z} \\ (N_a^e \psi_\alpha^p)_{,y} & (N_a^e \psi_\alpha^p)_{,x} & 0 \\ 0 & (N_a^e \psi_\alpha^p)_{,z} & (N_a^e \psi_\alpha^p)_{,y} \\ (N_a^e \psi_\alpha^p)_{,z} & 0 & (N_a^e \psi_\alpha^p)_{,x} \end{bmatrix}; \tag{5.12}$$

$$\tilde{\mathbf{B}}_a^e = \begin{bmatrix} (N_a^e \Upsilon_\alpha^p)_{,x} & 0 & 0 \\ 0 & (N_a^e \Upsilon_\alpha^p)_{,y} & 0 \\ 0 & 0 & (N_a^e \Upsilon_\alpha^p)_{,z} \\ (N_a^e \Upsilon_\alpha^p)_{,y} & (N_a^e \Upsilon_\alpha^p)_{,x} & 0 \\ 0 & (N_a^e \Upsilon_\alpha^p)_{,z} & (N_a^e \Upsilon_\alpha^p)_{,y} \\ (N_a^e \Upsilon_\alpha^p)_{,z} & 0 & (N_a^e \Upsilon_\alpha^p)_{,x} \end{bmatrix} \tag{5.13}$$

The three dimensional external force contribution follows the same procedure as the two dimensional case, therefore the formulation from Eq. 5.11 is outlined in Section 3.4 and is presented in Eqs. 3.36-3.39.

The elastic deformation of the fibers are accounted for in the third term in Eq. 5.11. The

elastic deformation of the two dimensional fiber can be approximated at the center of the fiber due to the uniform stress across the width of the fiber.

The fiber components that lie in enriched elements are expressed in the integral term as:

$$\int_{\Omega_\alpha} \epsilon_f^\alpha \delta\epsilon_f^\alpha \, d\Omega = \sum_{e=1}^{n_e^\alpha} \int_{\Omega_\alpha^e} \epsilon_f^\alpha \delta\epsilon_f^\alpha \, d\Omega \tag{5.14}$$

in which, n_e^α denotes the number of fully enriched elements that contains a part of the fiber, α. The fiber is assumed to deform uniformly within each element. The axial strain of fiber, α, can be defined as:

$$\epsilon_f^\alpha = \frac{[\mathbf{u}(\mathbf{x}_{2c}^{\alpha e}) - \mathbf{u}(\mathbf{x}_{1c}^{\alpha e})] \cdot \boldsymbol{t}_{\alpha c}}{l_{\alpha ce}}; \quad \mathbf{x} \in \Omega_\alpha^e \tag{5.15}$$

where, the entry and exit positions of the center of the fiber on the enrichment element are $\mathbf{x}_{1c}^{\alpha e}$ and $\mathbf{x}_{2c}^{\alpha e}$; the length of the fiber segment that lies within the element is denoted as $l_{\alpha ce} = ||\mathbf{x}_{2c}^{\alpha e} - \mathbf{x}_{1c}^{\alpha e}||$; and $\boldsymbol{t}_{\alpha c}$ is the tangent vector on the fiber domain between $\mathbf{x}_{1c}$ and $\mathbf{x}_{2c}$. When the fiber crosses the domain of the element, the fiber entry and exit positions are on the element faces. If the domain of the fiber ends within the element, the end position of the fiber segment coincides with the fiber end edge center.

Substituting Eq. 5.15 in the third term in Eq. 5.11 leads to:

$$\begin{aligned} A_{f\alpha}E_f \int_{\Omega_\alpha^e} \epsilon_f^\alpha \delta\epsilon_f^\alpha \, d\Omega &= \frac{A_{f\alpha}E_f}{l_{\alpha ce}} \left[(\mathbf{u}(\mathbf{x}_{2c}^{\alpha e}) - \mathbf{u}(\mathbf{x}_{1c}^{\alpha e})) \cdot \boldsymbol{t}_{c\alpha}\right] \left[(\delta\mathbf{u}(\mathbf{x}_{2c}^{\alpha e}) - \delta\mathbf{u}(\mathbf{x}_{1c}^{\alpha e})) \cdot \boldsymbol{t}_{c\alpha}\right] \\ &= \left(\delta\hat{\mathbf{u}}^e\right)^T \breve{\mathbf{K}}_e^{\alpha s} \hat{\mathbf{u}}^e \end{aligned} \tag{5.16}$$

The enrichment functions vanish on the domain of the fiber and therefore the stiffness matrix is nonzero only for the standard degrees of freedom:

$$\breve{\mathbf{K}}_e^\alpha = \begin{bmatrix} \breve{\mathbf{K}}_e^{\alpha s} & \mathbf{0} \\ \mathbf{0} & \mathbf{0} \end{bmatrix} \tag{5.17}$$

where,

$$\breve{\mathbf{K}}_e^{\alpha s} = \frac{A_{f\alpha} E_f}{l_{\alpha ce}} \begin{bmatrix} \breve{\mathbf{K}}_{e,11}^{\alpha s} & \breve{\mathbf{K}}_{e,12}^{\alpha s} & \dots & \breve{\mathbf{K}}_{e,1n_n^e}^{\alpha s} \\ \breve{\mathbf{K}}_{e,21}^{\alpha s} & \breve{\mathbf{K}}_{e,22}^{\alpha s} & & \vdots \\ \vdots & & \ddots & \vdots \\ \breve{\mathbf{K}}_{e,n_n^e 1}^{\alpha s} & \dots & \dots & \breve{\mathbf{K}}_{e,n_n^e n_n^e}^{\alpha s} \end{bmatrix} \tag{5.18}$$

The individual component of the stiffness matrix is written as:

$$\breve{\mathbf{K}}_{e,ab}^{\alpha s} = \left[N_b^e(\mathbf{x}_{2c}^{\alpha e}) - N_b^e(\mathbf{x}_{1c}^{\alpha e})\right] \left[N_a^e(\mathbf{x}_{2c}^{\alpha e}) - N_a^e(\mathbf{x}_{1c}^{\alpha e})\right] (\boldsymbol{t}_{\alpha c} \otimes \boldsymbol{t}_{\alpha c}) \tag{5.19}$$

The contribution can be computed using the standard assembly operation:

$$\breve{\mathbf{K}}^{\alpha} = \underset{e=1}{\overset{n_e^{\alpha}}{\mathbf{A}}} \breve{\mathbf{K}}_e^{\alpha} \tag{5.20}$$

The internal contribution from the second term in Eq. 5.11 then becomes:

$$\mathbf{f}_{\text{int},2}^{\alpha}(\mathbf{U}) = \breve{\mathbf{K}}^{\alpha}\mathbf{U} \tag{5.21}$$

The progressive debonding between the fiber and the matrix is accounted for in the fourth component of Eq. 5.11. The progressive debonding is expressed in terms of the jump enrichment degrees of freedom. For an arbitrary fiber, α:

$$\int_{\Gamma_\alpha} (\delta[\![\mathbf{u}]\!])^T \, \boldsymbol{T}([\![\mathbf{u}]\!]) \, d\Gamma = (\delta\hat{\mathbf{d}})^T \int_{\Gamma_\alpha} (\mathbf{P}^{\alpha})^T \boldsymbol{T}(\hat{\mathbf{d}}) \, d\Gamma = (\delta\hat{\mathbf{d}})^T \mathbf{f}_{\text{int},3}^{d\alpha}(\hat{\mathbf{d}}) \tag{5.22}$$

in which, shape functions for the jump enrichments are included in $\mathbf{P}^{\alpha}$.:

$$\mathbf{P}^{\alpha} = \left\{\mathbf{P}_1^{\alpha}, \mathbf{P}_2^{\alpha}, \dots, \mathbf{P}_{n_{\text{en}}^{\alpha}}^{\alpha}\right\}; \quad \mathbf{P}_a^{\alpha} = N_{\mathcal{I}_a^{\alpha}}(\mathbf{x}) \, \Upsilon_{\alpha}^{p}(\mathbf{x}) \begin{bmatrix} 1 & 0 & 0 \\ 0 & 1 & 0 \\ 0 & 0 & 1 \end{bmatrix} \tag{5.23}$$

A force vector contribution is assembled from the debonding enrichment terms (i.e., $\mathbf{V}^T\mathbf{f}^{\alpha}_{\text{int},3}(\mathbf{U})$):

$$\mathbf{f}^{\alpha}_{\text{int},3} = \left\{\mathbf{0};\, \mathbf{0};\, \mathbf{f}^{d\alpha}_{\text{int},3}\right\} \tag{5.24}$$

where the internal force contribution is only due to the jump degrees of freedom. A system of nonlinear equations from equilibrium of the three internal force and external force contributions is expressed in the form of:

$$\phi\left(\mathbf{U}\right) = \mathbf{f}_{\text{int}}\left(\mathbf{U}\right) - \mathbf{f}_{\text{ext}} = 0 \tag{5.25}$$

where,

$$\mathbf{f}_{\text{int}}\left(\mathbf{U}\right) = \mathbf{f}_{\text{int},1} + \sum_{\alpha=1}^{n}\left(\mathbf{f}^{\alpha}_{\text{int},2} + \mathbf{f}^{\alpha}_{\text{int},3}\right) \tag{5.26}$$

The Newton-Raphson method is used to incrementally evaluate the nonlinear system in Eq. 5.26.

5.4.1 Numerical integration and partially enriched elements

The 3-D numerical integration for elements vary for each type of element. Methods to integrate enrichment functions in 3-D were investigated in Refs. [8, 59, 82]. In this chapter, the domain is comprised of hexagonal elements with four different element types: (1) far field elements; (2) partial enriched elements; (3) fully enriched elements; and (4) fully enriched elements that also have partial enrichment.

The integration rules for the element types are as follows:

1. Far field elements: Elements that have no enrichment and use standard quadrature rules with eight integration points in the hexagonal element.

2. Partially enriched elements: Element that includes some nodal enrichment from one or multiple fiber inclusions but is not fully enriched (i.e. fiber lies in adjacent element). Since no displacement discontinuity exists, standard integration is employed with eight

integration points in the hexagonal element. The modified enrichment functions in Eq. 4.4 and Eq. 4.5 are updated for the new enrichment functions and are used in the partially enriched elements.

3. Fully enriched elements: Elements that are crossed by one or multiple fibers. The element takes into consideration position of each of the fibers and the hexagonal domain is split up into tetrahedral sub domains (see Fig. 5.3) using Delaunay triangulation. The tetrahedral sub domains are placed such that no sub domain cross the domain of the fiber and line up with the fiber interface, to ensure that the components of the enrichment function for the fiber edges and domain level sets, are integrated separately. For both cases, the tetrahedral sub elements contains 11 integration points and use the standard Gauss quadrature rules.

4. Fully enriched elements that also have partial enrichment: The elements use the same element splitting rules as in the full enriched element type, and use higher order integration rules for each sub element. The element is treated for the full enrichment of the inclusions in the element as well as for the partial enrichments of the element.

The cohesive interface integration (Eq. 5.22) is performed using two dimensional Gauss quadrature, independent of the domain discretization. The fiber-matrix interface Γ_α is split into smaller planar rectangles along the length l_α. Each rectangular segment uses a 4-point quadrature rule.

5.5 Numerical Examples

In this section, the performance of the XFEM model in evaluating the response of short fiber reinforced composites in three dimensions is presented with numerical examples. The first example assesses the accuracy characteristics of a randomly oriented single fiber embedded for both an elastic matrix with perfect interface cohesion and for a matrix with progressive

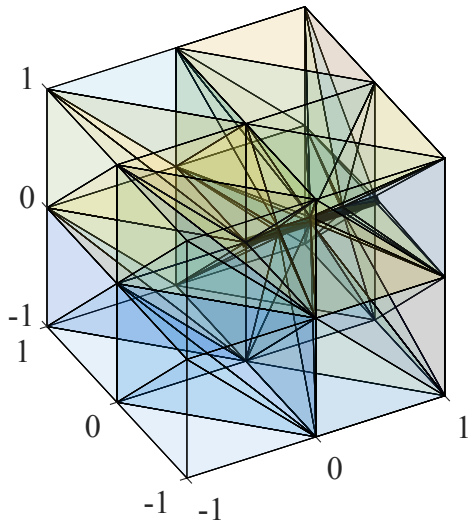

Figure 5.3: Three dimensional visualization of tetrahedral sub elements in an enrichment element. Thick black line represents the fiber inclusion. Integration points are not shown for clarity.

debonding on the fiber-matrix interface. The second example investigates the fiber-matrix debonding and composite stress for a case with two randomly oriented fibers neighboring each other. The third example illustrates the effect of the rotation of the fiber interface within the domain in relation to the applied loading. The fourth example evaluates a dense population of fibers within a domain.

5.5.1 Single fiber inclusion example

The XFEM formulation is verified against the finite element method for a single fiber composite in this section. The schematic representation of the model problem is shown in Fig. 5.4. The size of the domain is 4 mm by 4 mm by 4 mm and the length of the fiber is 1mm. The domain is subjected to uniform displacement controlled tensile loading at the right Y-Z face and symmetry boundary conditions are imposed on the left, bottom and back faces. The matrix material is taken to be concrete with the Young's modulus and Poisson's ratio of the matrix being 14 GPa and 0.3, respectively. The fiber is taken to be a high strength carbon fiber with the Young's modulus of 207 GPa and width and thickness of 20 μm and 1 μm, respectively. In this example, the fiber face is placed parallel to the direction of the loading

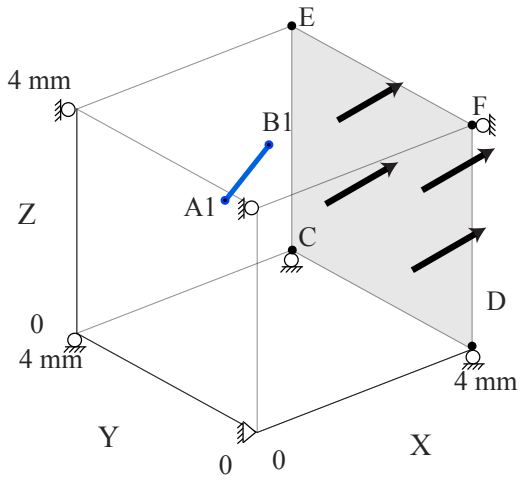

Figure 5.4: Geometry and boundary conditions of the single fiber inclusion example. Tensile loading occurs at the right Y-Z face (shaded area).

in the x direction with the fiber body positioned with angles of 63°, 106° and 32°, with respect to the x, y and z axes. In the elastic example, the fiber is fully bonded to the matrix. No fiber-matrix debonding occurs and the constituents are taken to deform elastically. In the progressive debonding example, the fiber-matrix debonding can occur.

The progressive debonding at the fiber-matrix interfaces is modeled with a bilinear cohesive zone law (outlined in Section 5.3) is employed for both the XFEM and the reference simulations. The cohesive zone law parameters for this example are based on work from Nicholas et al. [74]. The peak normal traction and normal cohesive characteristic separation length are set as 10 MPa and 1 nm respectively. The peak shear traction and shear cohesive characteristic separation lengths are set to the same as their normal counterparts for both shear directions. The maximum cohesive separation length is taken as 8 nm both for normal and shear directions.

The domain is discretized with uniform grids (hexagonal cubes) consisting of 64 elements up to 32,768 elements with corresponding element sizes of h=1 mm and h=0.125 mm, respectively. The reference model consists of a explicitly modeled fully resolved 3-D solid fiber and a very fine non-uniform discretization. The fiber domain is modeled using a very fine grid with the thickness using 3 elements per 1 μm. The reference model discretization resulted

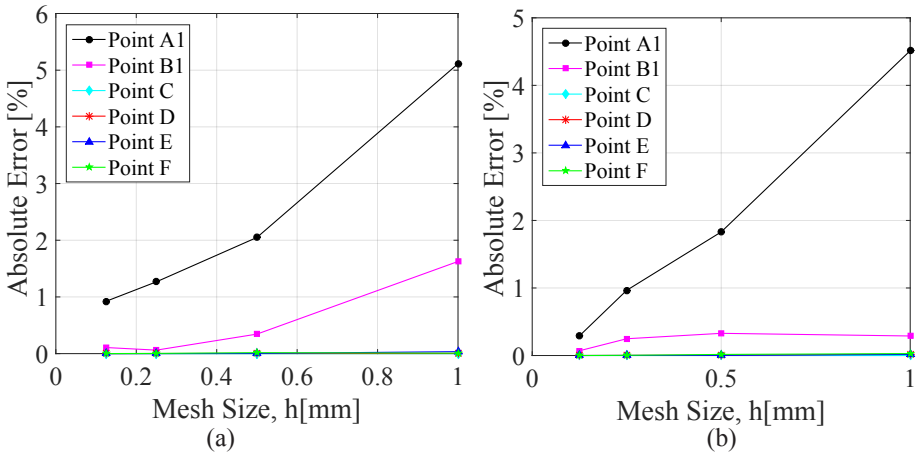

Figure 5.5: Pointwise error as a function of mesh density for a single fiber inclusion example: (a) elastic domain; and (b) domain with progressive debonding on the fiber-matrix interface.

in approximately 550,000 elements.

Figure 5.5 shows the point-wise displacement errors of the XFEM model with respect to the reference simulation. The point-wise error was computed using the L2-norm for each case and plotted with respect to element size in the domain. Points A1 and B1 correspond to the center of the fiber at the left and right edges, respectively. Point C is the upper right corner on the X-Y plane when Z=0 mm, Point D is the bottom right corner on the X-Y plane when Z=0 mm, Point E is the upper right corner on the X-Y plane when Z=4 mm, and Point F is the upper right corner on the X-Y plane when Z=4 mm. The six different point locations of interest are illustrated in Fig. 5.4.

The errors from the elastic example are shown in Fig. 5.5a. The errors showed monotonic convergence from the largest mesh size to the smallest mesh size. The left fiber end (A1) resulted in the largest error in all cases, but was below 1% for the smallest mesh size. Points C, D, E, and F all had minimal error for all mesh sizes. Figure 5.5b illustrates the point wise errors corresponding to the single fiber progressive debonding case. Similar to the errors in the elastic case, the errors showed monotonic convergence from the largest mesh size to the smallest mesh size, with all errors below 0.25% at the smallest mesh. The largest error occurred at point A1 for all mesh sizes and the errors at the edge of the domain (C, D, E,

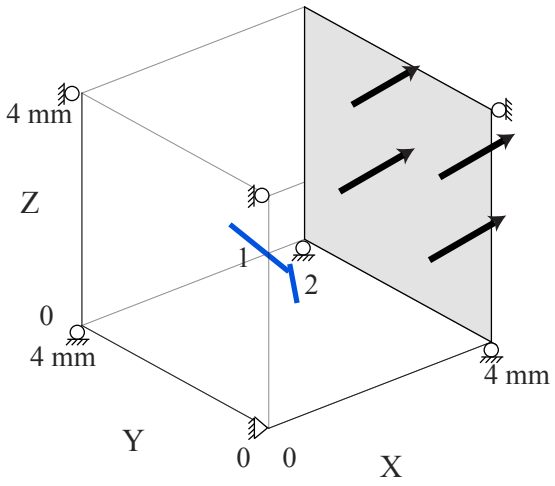

Figure 5.6: Geometry and boundary conditions of the two fiber inclusion example. Tensile loading occurs at the right Y-Z face (shaded area).

F) were negligible.

5.5.2 Two fiber inclusion example

In this section, a two fiber inclusion example is studied and compared against the direct finite element method for interfacial debonding and composite stress. Two fibers are placed neighboring each other in a composite domain subjected to uniform displacement controlled tensile loading. Fig. 5.6 displays the schematic representation of the two fiber domain. The domain is modeled as a 4 mm by 4 mm by 4 mm and subject to same loading and boundary conditions as in the single fiber example in Section 5.5.1. Both of the fibers in the domain are 1 mm in length and placed at angles of 55°, 35° and 89°, with respect to the x, y and z axes for fiber 1 and at angles of 70°, 140° and 123°, with respect to the x, y and z axes for fiber 2. In this example, the fibers are modeled with progressive debonding along the fiber-matrix interfaces. The matrix material properties, fiber material properties and the cohesive zone law are taken to be the same as in Section 5.5.1. The faces of both of the fibers lie parallel to the direction of the load.

The two fiber composite domain with the XFEM model is discretized using a mesh size of h=0.125 mm, resulting in 32,768 elements. The reference simulation, using the direct

finite element method, consists of approximately 740,000 elements. Similar to the example Section 5.5.1, the fiber domains are completely resolved with a fine grid of solid elements, with a thickness using 3 elements per 1 μm and the matrix uses a fine and non-uniform mesh.

Figure 5.7 displays the magnitude of the displacement jump of the length of both of the fibers as compared with the reference simulation. For both fibers, the XFEM models the general shape and magnitude of the displacement jump. The displacement jump for fiber 1 (Fig. 5.7a), displays approximately the same maximum magnitude over the length of fiber for the XFEM model as compared to the reference simulation. In both simulations, the ends of the fiber display a displacement jump. This value is due to the ability for the debonding at all edges of the fiber. The debonding at each of the fiber tips was slightly greater than that of the reference simulation. Fig. 5.7b shows the displacement jump across the fiber length with respect to fiber 2. The shape of the debonding in the XFEM model does not match exactly to the reference simulation, but does display similar magnitude and shape. As in the debonding in fiber 1, the ends of the fiber display debonding, in which the XFEM model was greater than that of the reference simulation. In both cases of fiber 1 and fiber 2, the magnitude of the displacement jump is controlled by the normal displacement jump, since in these examples, the face of the fiber is parallel with the direction of loading. The displacement jump in both fiber 1 and fiber 2 displays partial separation across their respective lengths. A three dimensional representation of the progressive debonding in the x, y, and z directions is illustrated in Fig. 5.8, for (a) a planar view in the X-Y plane, (b) a three dimensional view of the debonding in the domain and (c) a magnified view of the three dimensional debonding. The debonding is amplified significantly to show the magnitude and shape of displacement jumps.

An occurrence of error between the XFEM model and the reference simulation observed in Fig. 5.7 may be attributed to various reasons. In particular, the choice of the debonding enrichment function was taken as a Heaviside function, which does not represent the value

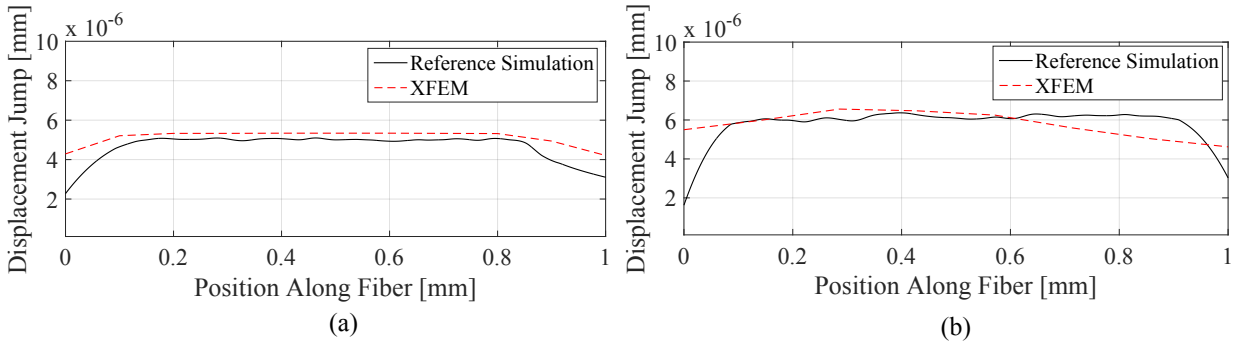

Figure 5.7: Magnitude of displacement jump along the fiber length for the two fiber case: (a) fiber 1; and (b) fiber 2 .

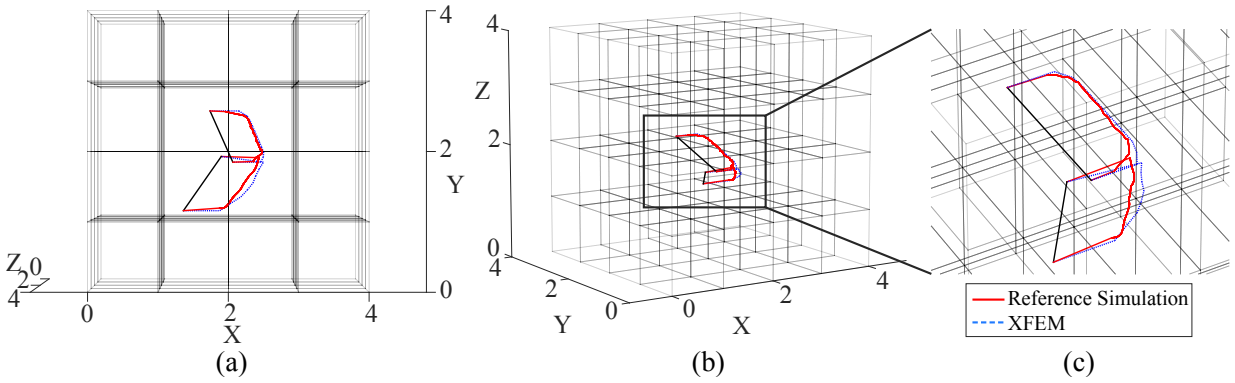

Figure 5.8: Debonding plots in a 3-D domain for the two fiber case: (a) perspective view; (b) 3-D view for debonding (magnitude is amplified for visualization purposes); and (c) magnified view of the 3-D debonding. (Solid straight black line represents each fiber, solid red line displays the reference model displacement jump and the blue dotted line is the XFEM model displacement jump.

of the displacement jump with precision, since as shown in the reference simulations, the magnitude of the displacement jump drops significantly at the fiber ends. The numerical integration of the sub domain may also be a contributing issue. Since the fiber face is significantly smaller than the elements that it lies in, the numerical integration may not be able to approximate the response accordingly.

The stress in the composite domain is investigated for the two fiber case. Since the fibers are modeled with high aspect ratios, they do not occupy a significant portion of the domain and the stress response will be local around the fibers. The stress plots below are taken as two dimensional view of a plane in the composite domain. The stress shown in all plots are the normal stresses in the x direction. The color in the plots represents the magnitude of the stress, with 6 MPa corresponding to red and 0 MPa corresponding to blue.

Fig. 5.9a displays the reference model simulation with a magnified view of the stress around the fiber. Fig. 5.9b displays the same view for the XFEM model including the magnified view of the stress around the fiber. The plot is taken at plane when Z=1.75 mm and depicts the X-Y plane of the composite body. It can be seen in both the reference model and XFEM model that the majority of the domain does not have much stress deviation and is approximately 4.2 MPa throughout. When looking at the magnified view of the stress around the fiber, the XFEM model similarly represents the reference simulation. Higher stress concentration is depicted in both models at each of the fiber edges (red marks at each end of the fiber width. Lower stress is shown for both models, near the center of the fiber (approximately 3 MPa). Stress slightly under 4 MPa is displayed on either side of the fiber face between the locations of higher stress concentration. There is some difference between the reference model and the XFEM model for the representation of the stress, but the XFEM model's stress approximation is in an acceptable range of deviation.

Fig. 5.10a and Fig. 5.10b display the normal stress in x direction on the X-Y plane when Z=1.55 mm, for the reference model and XFEM model, respectively. The figure is shown for a plane across the length of fiber 2. The fiber is depicted as the long black line. As in

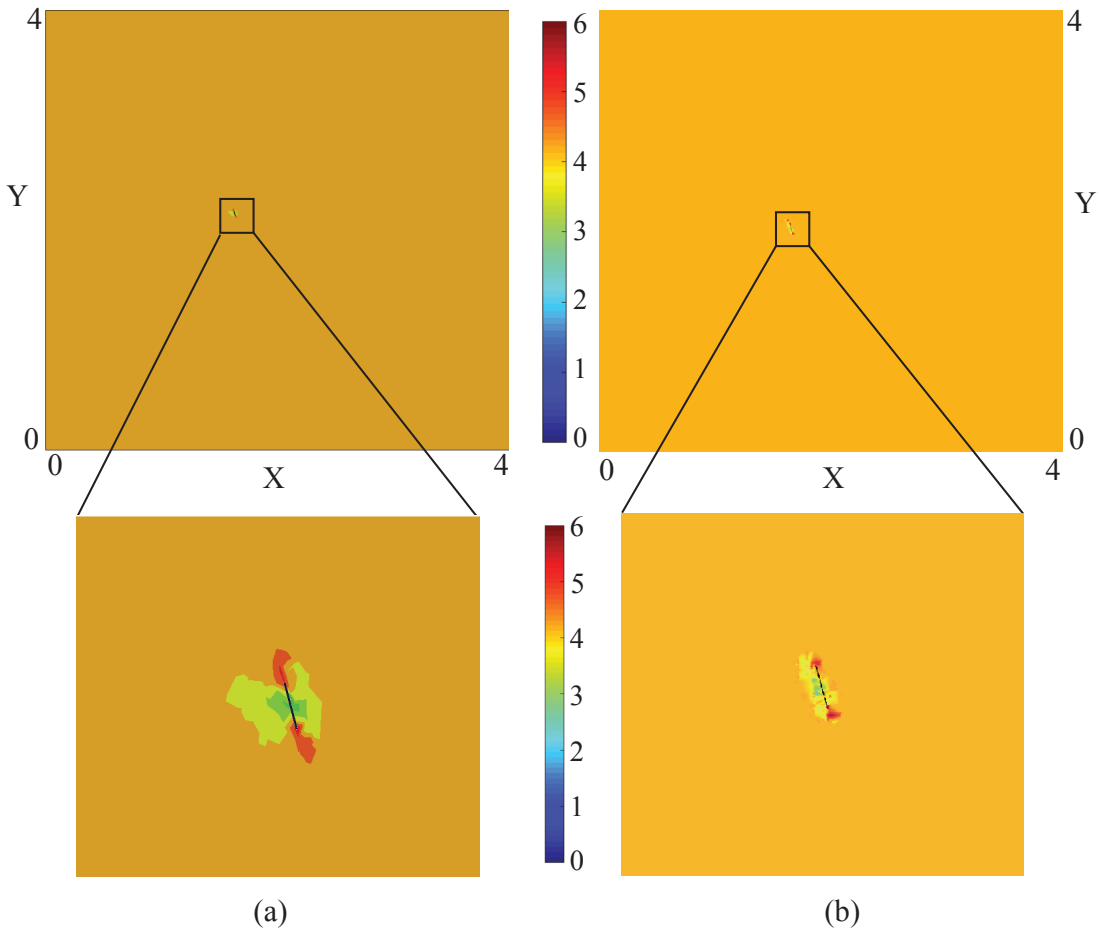

Figure 5.9: Cross sectional plot of the normal stress in the x direction in the composites over the width of fiber 1. Plot taken in the X-Y plane.: (a) reference simulation with magnified view of the stress around fiber 1; and (b) XFEM model with magnified view of the stress around fiber 1.

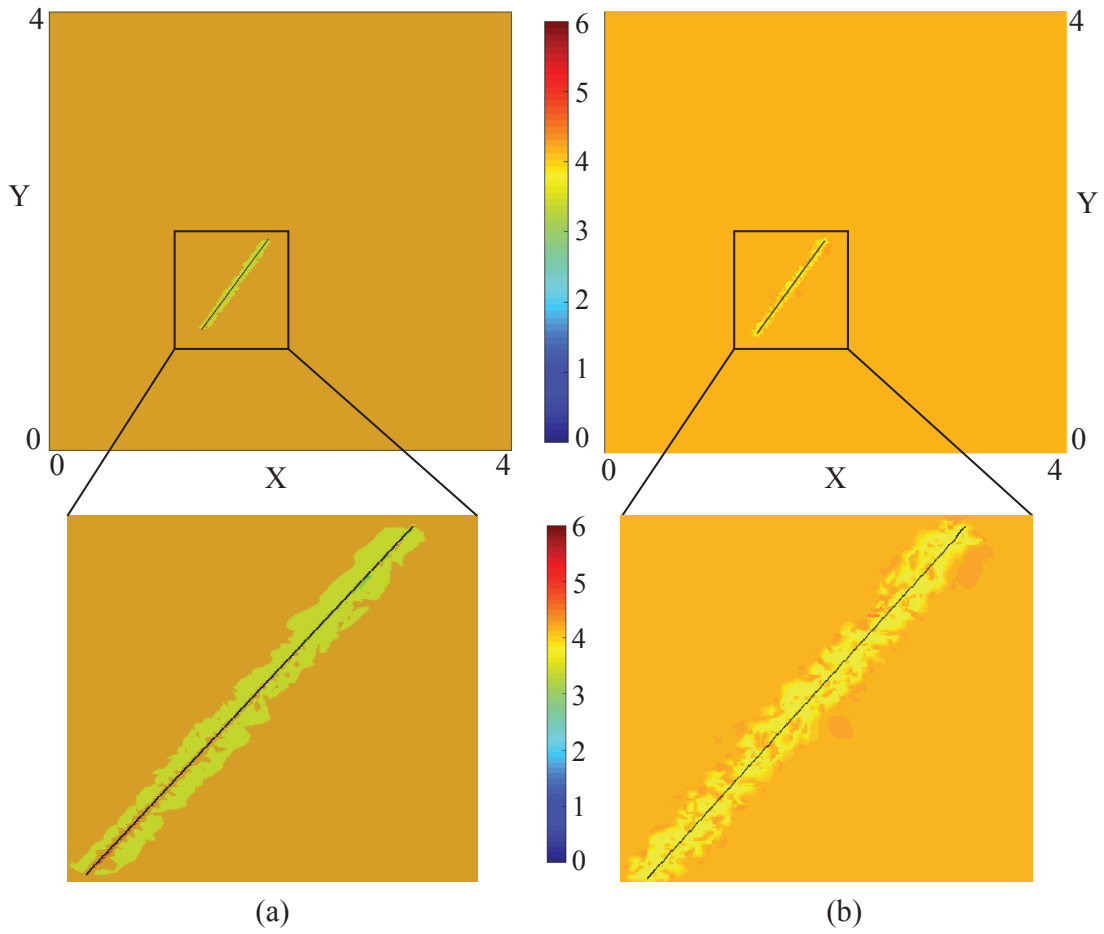

Figure 5.10: Cross sectional plot of the normal stress in the x direction in the composites over the length of fiber 2. Plot taken in the X-Y plane.: (a) reference simulation with magnified view of the stress around fiber 2; and (b) XFEM model with magnified view of the stress around fiber 2.

the stress shown for fiber 1 in Fig. 5.9, the stress deviation around the fiber is local. The magnified view of both the reference model and XFEM model show slightly lower stress (yellow in the figure, approximately 4 Mpa) than the remain domain (approximately 4.2 MPa). In both models, the stress is not uniformly distributed around the fiber with perfect stress contours, but both show the same magnitude of stress and radius of lower stress away from the fiber body.

The normal stress in the x direction was illustrated in Fig. 5.9 and Fig. 5.10 for two different cross sections in the composite domain accounting for the response from fiber 1 and fiber 2. There is some discrepancy between the reference model and the XFEM model. The error can be attributed to the plotting of the stress in the XFEM model. The stresses are calculated at each integration point within the domain and plotted. Since the XFEM model consists of much fewer integration points, particularly around the domain of the fiber, the stresses may not be able to have as uniform contours as the reference simulations. However, the stresses are still represented with accuracy around the high aspect ratio fibers within the domain.

5.5.3 Fiber rotation

In the single fiber example in section 5.5.1, the face of the fiber is parallel to the direction of the load. The rotation of the fiber face will alter the response of the composite. In this example, the rotation of the fiber face with respect to the direction of the load is investigated.

The single fiber case discussed in section 5.5.1 is modeled with progressive debonding for a variety of fiber face angles to evaluate the effect of fiber face angle in the composite. The same materials parameters, cohesive law and boundary conditions are used in this example as in the single fiber example. For this example, the XFEM mesh size is set at h=0.125 mm for all simulations. The fiber is rotated about its center axis for 13 different angles. The angle is measured at θ_f=0° for fiber face completely parallel to the direction of the load in the X direction (Fig. 5.11b). θ_f is rotated every 15° until the fiber face is perpendicular to

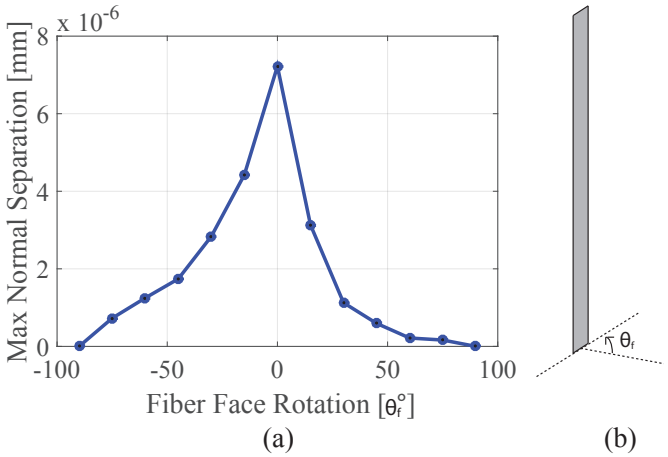

Figure 5.11: Fiber rotation response: (a) maximum normal separation as a function of the fiber face rotation; and (b) fiber face rotation with respect to the center of the fiber.

the direction of the load in both directions.

The maximum normal separation across the fiber interface is reported in Fig. 5.11a, for angles ranging from -90° to 90°. The maximum normal displacement jump occurred when the fiber face is parallel to the direction of the load. When the fiber is rotated 15° in either direction, there is a steep drop in maximum normal separation. The maximum normal separation decreases when the fiber face continues to rotate toward being perpendicular to the load. When the fiber face is completely perpendicular to the load, there is negligible normal separation. It can be seen that the direction of the fiber face influences the response of the fiber-matrix debonding.

5.5.4 Dense fiber domain

This section investigates a three dimensional dense fiber domain with the XFEM approach for the progressive debonding response. A domain of 4mm by 4mm by 4mm is taken to have 50 randomly oriented fibers in its domain with a mean length of 1 mm (± 0.1 mm), with a fixed width, as displayed in Fig. 5.12. All 50 fibers are randomly oriented in the domain as well as their faces being randomly oriented. The random dispersion of fibers results in multiple elements having mutliple fiber enrichments in them. Fibers do not touch and do not intersect each other. The mesh size used in this example is h=0.25 mm. It should be

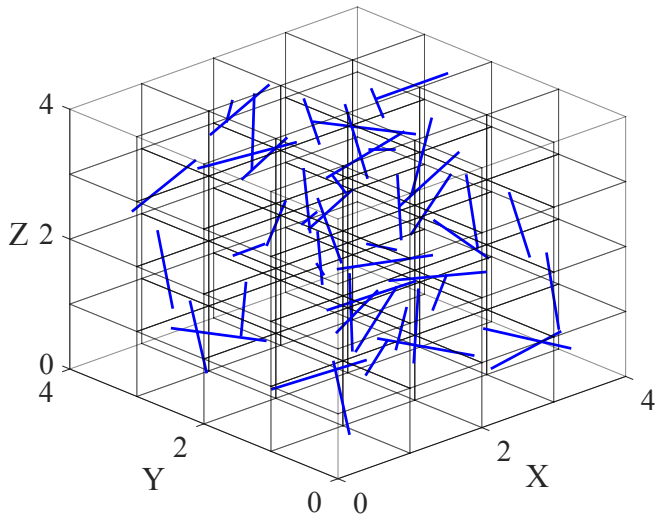

Figure 5.12: Three dimensional dense fiber domain.

noted that Fig. 5.12 does not display the mesh size used in this example, but uses a much larger element size for visualization purposes. The boundary conditions, matrix properties, fiber properties and cohesive law are taken to be the same as in Section 5.5.1

Fig. 5.13 summarizes the maximum separation at the fiber-matrix interface for each of the fibers. The magnitude range of the maximum separation are categorized in Fig. 5.13a. There were three fibers that resulted in in a maximum interface separation of less than 2.5e-6 mm. 33 fibers had a maximum separation between 2.5e-6 mm and 5e-6 mm, nine fibers had a maximum separation between 5e-6 mm and 7.5e-6 mm and 5 fibers resulted in a maximum separation over 7.5e-6 mm. Fig. 5.13b displays the severity of debonding. The majority of the fibers in the domain displayed partial separation at their fiber-matrix interface (44 of the 50 fibers). Only two fibers showed no separation and four fibers had complete separation at the fiber matrix interface.

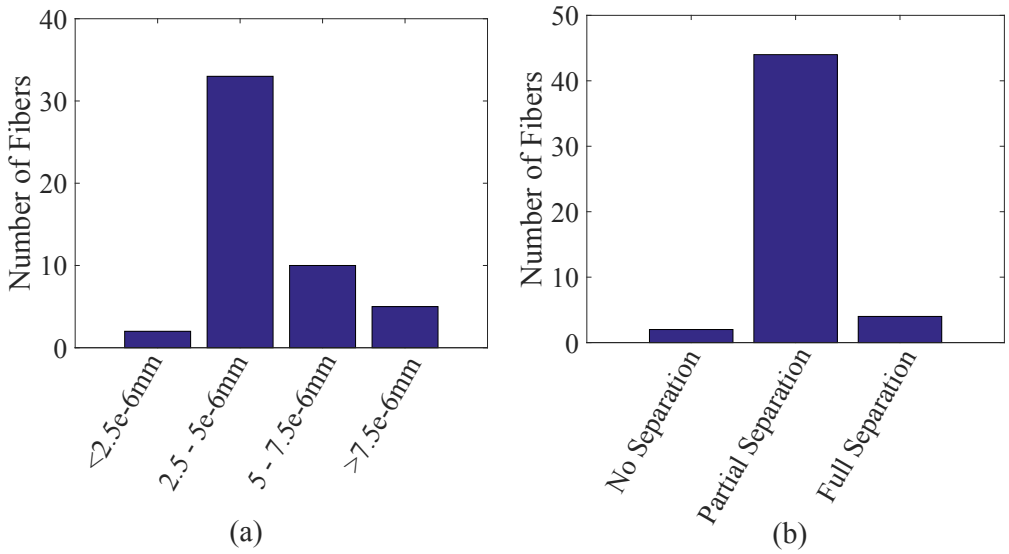

Figure 5.13: Summary of displacement jumps for the fibers in the dense fiber domain: (a) total number of fibers with their respective maximum separation of each displacement jump; (b) total number of fibers with no separation, partial separation and full separation.

CHAPTER 6

SUMMARY AND FUTURE WORK

6.1 Conclusions

This dissertation provided a computational framework for the formulation and implementation of an extended finite element method for random short fiber reinforced composites. Numerical testing verified and assessed the performance characteristics of the proposed model against the direct finite element method. The principal achievements of this dissertation are summarized below.

Chapter 2 provided the formulation and implementation of XFEM for random rigid short fiber reinforced composite materials. An enrichment function was developed to incorporate the effect of random fiber inclusions within the XFEM framework and eliminated the need of using finite element meshes compliant with fiber inclusions. The motion of the fiber inclusions were modeled by constraining the deformation field along the domain of the fiber inclusions. Numerical integration procedures were provided for accurate evaluation of the system response for fiber tips that lay on arbitrary positions within the problem domain and for the rigid constraint of the fibers. The coupling of the XFEM method along with the enrichment function and constraint equations formulated the elastic response of short fiber reinforced composites. The numerical examples verified the performance characteristics of the XFEM model against the direct finite element method. The XFEM approach accurately characterizes the elastic response of short fiber reinforced composites without the need for mesh compliance.

Chapter 3 presented the formulation and implementation of XFEM modeling of progressive failure for random short fiber reinforced composites with material cohesive interfaces. The fiber inclusions were modeled as elastic objects of zero measure using the XFEM approach. A debonding enrichment function was developed to idealize the progressive debond-

ing between the fiber-matrix interfaces with the XFEM framework, to eliminate the need of using finite element meshes compliant with fiber inclusions. The axial fiber deformation was modeled through inclusion of stretching strain energy explicitly into the Lagrangian. With the extension to 3-D in mind, an integral-type nonlocal damage model was used to describe the progressive cracking in the matrix. Numerical integration procedures were provided for accurate evaluation of the system response for fibers at random positions within the problem domain. The performance of the XFEM model was assessed against the direct finite element method for various fiber configurations in two dimensions. The numerical assessment indicated that the XFEM approach accurately demonstrated the response of short fiber reinforced composites and the interfacial properties significantly effect the response of the composite.

Chapter 4 introduced the formulation and implementation of an XFEM model to capture the interactions between fibers in short fiber reinforced composites. The fiber inclusions were modeled as elastic objects of zero measure. Inclusion and debonding enrichment functions were included to model the fibers and the progressive fiber-matrix debonding within the XFEM framework. Numerical integration procedures were provided for accurate evaluation of the system response for randomly positioned nearby fibers. The performance of the XFEM model was assessed against the direct finite element method for various multiple fiber domain configurations in two dimensions. The approach accurately captures the elastic and progressive debonding interaction behavior between multiple short fibers in reinforced composites. The ability to include multiple enrichments in the same element provides the capability to increase fiber density in the composite microstructure without significantly increasing the base finite element grid density, allowing the capability to simulate microstructures with a large number of fibers.

Chapter 5 introduced a three dimensional XFEM formulation and implementation for short fiber reinforced composites. Short fibers were modeled as elastic deformable two dimensional planar rectangular inclusions in the XFEM framework. Fiber and debonding

enrichment functions were presented to approximate the presence of the 2-D fibers in the 3-D domain and to account for the progressive debonding on the fiber-matrix interface. This chapter provided a modeling approach for high aspect ratio inclusions. The performance of the XFEM approach was assessed against the direct finite element method for single and two fibers domain configurations. The XFEM model investigated the influence of the direction of the fiber face as well as a domain with a dense fiber population.

The present XFEM approach is significantly more computational efficient compared to a finite element analysis, in which the microstructure is fully resolved as demonstrated in the numerical examples. The computational efficiency of the present approach remains too high to be included in a concurrently coupled multiscale simulation, yet presents an efficient approach for sequential multiscale algorithms, as well as investigations of failure mechanisms within composite microstructures.

6.2 Future Work

While the XFEM models used in this dissertation work well for the problems analyzed, several challenges remain in more realistic and complicated applications. As seen in chapter 3 of this dissertation, the interfacial properties between the fibers and the matrix significantly affects the behavior of the composite. The interfacial properties can alter various mechanical properties of the composites, including flexural strength and ductility. In this work, the interface properties were considered along the entire length of the fiber-matrix interface, in reality there the bond may differ at different locations along the length. Therefore, spatial variability should be considered to accurately access the interfacial response. These interfacial properties will be investigated to gain a better understanding on how they can be optimized for various applications and how they can enhance the behavior of the composite. The development of problems when fibers come in contact with each other also needs to be addressed. However, this is a computationally demanding process, since there will be a significant amount of fibers present in the domain.

A key feature that needs to be addressed is the modeling of realistic fiber volume fractions (e.g. 0.5%, 1%, 2%, etc.) of high aspect ratio fibers in a domain in three dimensions in order to compare and reproduce with experiments. Using high aspect ratio fibers to achieve the realistic fiber volume fractions produces a significant amount of fibers in the RVE that results in numerous fibers in close proximity of each other, which may affect the approximation of the composite. Various approximations and assumptions will need to be addressed in order to model realistic volume fractions using high aspect ratio fibers with XFEM.

In this work, the material properties were taken as high strength carbon fibers with a cement matrix and the mechanical response were investigated. The XFEM method and approach does not have to be limited to this type of material. The approach can be applied to a variety of different types of composites over a wide range of materials. The response using different type of composites may have different behavior and should be investigated.

[1] J. Aboudi. The effective moduli of short-fiber composites. *Int. J. Solids and Struct.*, 19:693–707, 1983.

[2] A. Aimi, M. Diligenti, and F. Freddi. Numerical aspects in the SGBEM solution of softening cohesive interface problems. *J. of Comp. and Appl. Math.*, 210:22–33, 2007.

[3] J.L. Asferg, P.N. Poulsen, and L.O. Nielsen. A consistent partly cracked XFEM element for cohesive crack growth. *Int. J. Numer. Meth. Engng.*, 72:464–485, 2007.

[4] I. Babuska and J. M. Melenk. The partition of unity method. *Int. J. Numer. Meth. Engng.*, 40:727–758, 1997.

[5] N. Banthia. Uniaxial tensile response of microfibre reinforced cement composites. *Mater. Str.*, 28:507–517, 1995.

[6] F. Barzegar and S. Maddipudi. Three dimensional modelling of conrete structures. ii: Reinforced concrete. *J. Struct. Engng.*, 123:1347–1356, 1997.

[7] Z. Bazant and M. Jirasek. Nonlocal integral formulations of plasticity and damage: Survey of progress. *J. of Engng. Mech.*, 128:1119– 1149, 2002.

[8] E. Bechet, H. Minnebo, N. Moes, and B. Burgardt. Improved implementation and robustness study of the X-FEM for stress analysis around cracks. *Int. J. Numer. Meth. Engng.*, 64:1033–1056, 2005.

[9] T. Belytschko and T. Black. Elastic crack growth in finite elements with mimal remeshing. *Int. J. Numer. Meth. Engng.*, 45:601–620, 1999.

[10] T. Belytschko, N. Moes, S. Usui, and C. Parimi. Arbitrary discontinuities in finite elements. *Int. J. Numer. Meth. Engng.*, 50:993–1013, 2001.

[11] T. Belytschko, R. Gracie, and G. Ventura. A review of extended/generalized finite element methods for material modeling. *Modelling Simul. Mater. Sci. Engng.*, 17: 043001, 2009.

[12] B. Benowitz and H. Waisman. A spline-based enrichment function for arbitrary inclusions in extended finite element method with applications to finite deformations. *Int. J. Numer. Meth. Engng.*, 956:361–386, 2013.

[13] E. Benvenuti. A regularized XFEM framework for embedded cohesive interfaces. *Comput. Meth. Appl. Mech. Engng.*, 197:4367–4378, 2008.

[14] M. Bogdanor, C. Oskay, and S. Clay. Multiscale modeling of failure in composites under model parameter uncertainty. *Comput. Mech.*, 56:389–404, 2015.

[15] H. J. Bohm, A. Eckschlager, and W. Han. Multi-inclusion unit cell models for metal matrix composites with randomly oriented discontinuous reinforcements. *Comp. Mater. Sci.*, 25:42–53, 2002.

[16] S. P. A. Bordas, T. Rabczuk, N. X. Hung, V.P. Nguyen, S. Natarajan, T. Bog, D. M Quan, and N. V. Hiep. Strain smoothing in FEM and XFEM. *Comp. Struct.*, 88: 1419–1443, 2010.

[17] A. Bouaziz, M. Nait-Abdelaziz, J.M. Gloaguen, and J.M. Lefebvre. Micromechanical modelling and experimental investigation of random discontinuous glass fiber polymer–matrix composites. *Compos. Sci. Technol.*, 67:3278–3285, 2007.

[18] L. Bouhala, A. Makradi, S. Belouettar, H. Kiefer-Kamal, and P. Freres. Modelling of failure in long fibres reinforced composites by X-FEM and cohesive zone model. *Compos. : Part B*, 55:353–361, 2013.

[19] L. Bouhala, Q. Shao, Y. Koutsawa, A. Younes, P. Nunez, A. Makradi, and S. Belouettar. An XFEM crack-tip enrichment for a crack terminating at a bi-material interface. *Engng. Fract. Mech.*, 102:51–64, 2013.

[20] E. Budyn, G. Zi, N. Moes, and T. Belytschko. A method for multiple crack growth in brittle materials without remeshing. *Int. J. Numer. Meth. Engng.*, 61:1741–1770, 2004.

[21] A. Carpinteri. Softening and snap-back instability in cohesive solids. *Int. J. Numer. Meth. Engng.*, 28:1521–1537, 1989.

[22] L. Chen, T. Rabczuk, S. P. A. Bordas, G.R. Liu, K.Y. Zeng, and P. Kerfriden. Extended finite element method with edge-based strain smoothing (ESm-XFEM) for linear elastic crack growth. *Comput. Meth. Appl. Mech. Engng.*, 209:250–265, 2012.

[23] J. Chessa, H. Wang, and T. Belytschko. On the construction of blending elements for local partition of unity enriched finite elements. *Int. J. Numer. Meth. Engng.*, 57: 1015–1038, 2003.

[24] D.D.L. Chung. Cement reinforced with short carbon fibers: a multifunctional material. *Compos. Part B: Engng.*, 31:511–526, 2000.

[25] D.D.L. Chung. Composites get smart. *Materials Today*, 5:30–35, 2002.

[26] D. Coronelli and M.G. Mulas. Local global approach in the seismic analysis of R/C frames including bond slip effects. *Engng. Struct.*, 23:911–925, 2001.

[27] R. D. Crouch and C. Oskay. Accelerated time integrator for multiple time scale homogenization. *Int. J. Numer. Meth. Engng.*, 101:1019–1042, 2015.

[28] R. D. Crouch, S. B. Clay, and C. Oskay. Experimental and computational investigation of progressive damage accumulation in cfrp composites. *Compos. Part B: Engng.*, 48: 59.–67, 2013.

[29] R. D. Crouch, C. Oskay, and S. Clay. Multiple spatio-temporal scale modeling of composites subjected to cyclic loading. *Comput. Mech.*, 51:93–107, 2013.

[30] C. Daux, N. Moes, J. Doblow, N. Sukumar, and T. Belytschko. Arbitrary branched and intersecting cracks with the extended finite element method. *Int. J. Numer. Meth. Engng.*, 48:1741–1760, 2000.

[31] J. Doblow, S. Mosso, J. Robbins, and T. Voth. Coupling volume-of-fluid based interface reconstructions with the extended finite element method. *Comp. Meth. Appl. Mech. Engng.*, 197:439–447, 2008.

[32] C. A. Duarte, I. Babuska., and J. Oden. Generalized finite element methods for three-dimensional structural mechanics problems. *Comp. Struct.*, 77:215–232, 2000.

[33] C.A. Duarte, O.N. Hamzeh, T.J. Liszka, and W.W. Tworzydlo. A generalized finite element method for the simulation of three dimensional dynamic crack propagation. *Comput. Meth. Appl. Mech. Engng.*, 190:2227–2262, 2001.

[34] A.E. Elwi and T.M Hrudey. Finite element model for curved embedded reinforcement. *J. Engng. Mech.*, 115:740–754, 1989.

[35] A.G. Evans and F.W. Zok. The physics and mechanics of fibre-reinforced brittle matrix composites. *J. of Mat. Sci.*, 29:3857–3896, 1994.

[36] J. Fish. Hierarchical modeling of discontinuous fields. *Comm. Appl. Num. Meth.*, 8: 443–453, 1992.

[37] J. Fish and C. Oskay. A nonlocal multiscale fatigue model. *Mech. of Adv. Mat. and Struct.*, 12:485–500, 2005.

[38] J. Fish and A. Wagiman. Multiscale finite element method for heterogeneous medium. *Comp. Mech.: Int. J.*, 12:1–17, 1993.

[39] J. Fish, Q. Yu, and K. Shek. Computational damage mechanics for composite materials based on mathematical homogenization. *Int. J. Numer. Meth. Engng.*, 45:1657–1679, 1999.

[40] T. Fries and T. Belytschko. The intrinsic XFEM: a method for arbitrary discontinuities without additional unknowns. *Int. J. Numer. Meth. Engng.*, 68:1358–1385, 2006.

[41] T.P. Fries. A corrected XFEM approximation without problems in blending elements. *Int. J. Numer. Meth. Engng.*, 75:503–532, 2008.

[42] T.P. Fries, A. Byfut, A. Alizada, K. Chen, and A. Schroder. Hanging nodes and xfem. *Int. J. Numer. Meth. Engng.*, 86:404–430, 2011.

[43] X. Fu and D. D. L. Chung. Submicron carbon filament cement-matrix composites for electromagnetic interference shielding. *Cement and Concrete Research*, 26:1467–1472, 1996.

[44] I.G. Garcia, M. Paggi, and V. Mantic. Fiber-size effects on the onset of fiber-matrix debonding under transverse tension: A comparison between cohesive zone and finite fracture mechanics models. *Engng. Fract. Mech.*, 115:96–110, 2014.

[45] K. Garikipati and T.J.R. Hughes. A variational multiscale approach to strain localization formulation for multidimensional problem. *Comp. Meth. Appl. Mech. Engng.*, 188:39–60, 2000.

[46] M. G. D. Geers, W. A. M. Brekelmans, and R. de Borst. Viscous regularization of strain-localisation for damaging materials. In *DIANA Computational Mechanics*. Springer Netherlands, 1994.

[47] V. Gopalaratnam and S. Shah. Tensile failure of steel fiber reinforced mortar. *J. Engng. Mech.*, 113:635–652, 1987.

[48] E. Gordeliy and A. Peirce. Enrichment strategies and convergence properties of the XFEM for hydraulic fracture problems. *Comput. Meth. Appl. Mech. Engng.*, 283: 474–502, 2015.

[49] A Gravouil, N. Moes, and T. Belytschko. Non-planar 3D crack growth by the extended finite element and level sets Part II: Level set update. *Int. J. Numer. Meth. Engng.*, 53:2569–2586, 2002.

[50] A. Hansbo and P. Hansbo. A finite element method for the simulation of strong and weak discontinuities in solid mechanics. *Comput. Meth. Appl. Mech. Engng.*, 193: 3523–3540, 2004.

[51] H. Hartl. *Development of a continuum mechanics based tool for 3D FEA of RC Structures and application to problems of soil structure interaction*. PhD thesis, Graz Univ. of Technology, 2002.

[52] T. Hettich and E. Ramm. Modeling of failure in composites by X-FEM and level sets within a multiscale framework. *Comput. Meth. Appl. Mech. Engng.*, 197:414–424, 2008.

[53] B. Hiriyur, H. Waisman, and G. Deodatis. Uncertainty quantification in homogenization of heterogeneous microstructures modeled by XFEM. *Int. J. Numer. Meth. Engng.*, 88:257–278, 2011.

[54] J. H. Huang. Some closed-form solutions for effective moduli of composites containing randomly oriented short fibers. *Mater. Sci. Engng. A*, 315:11–20, 2001.

[55] P. Jager, P. Steinnmann, and E. Kuhl. Modeling three-dimensional crack propagation - a comparison of crack path tracking strategies. *Int. J. Numer. Meth. Engng.*, 76: 1328–1352, 2008.

[56] M. Jirasek. Nonlocal models for damage and fracture: comparison of approaches. *Int. J. of Solids and Struct.*, 35:4133–4145, 1998.

[57] M. Jirasek. Comparative study on finite elements with embedded discontinuities. *Comput. Meth. Appl. Mech. Engng.*, 188:307–330, 2000.

[58] M. Jirasek. Non-local damage mechanics with application to concrete. *Revue Franaise de Gnie Civil*, 8:683–707, 2004.

[59] P. Laborde, J. Pommier, Y. Renard, and M. Salaun. High-order extended finite element method for cracked domains. *Int. J. Numer. Meth. Engng.*, 64:354–381, 2005.

[60] M. Lan, H. Waisman, and I. Harari. A high-order extended finite element method for extraction of mixed-mode strain energy release rates in arbitrary crack settings based on Irwins integral. *Int. J. Numer. Meth. Engng.*, 96:787–812, 2013.

[61] D. Lange, C. Ouyang, and S. Shah. Behavior of cement based matrices reinforced by randomly dispered microfibers. *Adv. Cement Based Mat.*, 3:20–30, 1996.

[62] A. Legay, H. W. Wang, and T. Belytschko. Strong and weak arbitrary discontinuities in spectral finite elements. *Int. J. Numer. Meth. Engng.*, 64:991–1008, 2005.

[63] S. Li, M.D. Thouless, A.M. Waas, J.A. Schroeder, and P.D. Zavattieri. Mixed-mode cohesive-zone models for fracture of an adhesively bonded polymermatrix composite. *Engng. Fract. Mech.*, 73:64–78, 2006.

[64] V.C. Li. On engineered cementitious composites (ECC) - a review of the material and its applications. *J. of Advanced Concrete Technol.*, 1:215–230, 2003.

[65] H. R. Lusti, P.J. Hine, and A.A. Gusev. Direct numerical predictions for the elastic and thermoelastic properties of short fibre composites. *Compos. Sci. Technol.*, 62: 1927–1934, 2002.

[66] G.C. Lykidis and K.V. Spiliopoulus. 3D solid finite element analysis of cylically loaded RC structures allowing embedded reinforcment slippage. *J. Struct. Engng.*, 134:629–638, 2008.

[67] L. Mishnaevsky Jr. and P. Brndsted. Three-dimensional numerical modelling of damage initiation in unidirectional fiber-reinforced composites with ductile matrix. *Mater. Sci. and Engng. A*, 498:81–86, 2008.

[68] N. Moës and T. Belytschko. Extended finite element method for cohesive crack growth. *Engng. Fract. Mech.*, 69:813–833, 2002.

[69] N. Moës, J. Dolbow, and T. Belytschko. A finite element method for crack growth without remeshing. *Int. J. Numer. Meth. Engng.*, 46:131–150, 1999.

[70] N. Moes, A. Gravouil, and T. Belytschko. Non-planar 3D crack growth by the extended finite element and level sets Part I: Mechanical model. *Int. J. Numer. Meth. Engng.*, 53:2549–2568, 2002.

[71] N. Moës, M. Cloirec, P. Cartraud, and J.-F. Remacle. A computational approach to handle complex microstructure geometries. *Comput. Meth. Appl. Mech. Engng.*, 192: 3163–3177, 2003.

[72] S. Mohammadi. *Extended Finite Element Method for Fracture Analysis of Structures*. Blackwell, Oxford, UK, 2008.

[73] D. Motamedi and A. S. Milani. 3D nonlinear XFEM simulation of delamination in unidirectional composite laminates: A sensitivity analysis of modeling parameters. *Open J. of Comp. Mater.*, 3:113–126, 2013.

[74] T. Nicholas, D. Boyajian, S.E. Chen, and A. Zhou. Finite element modeling of mode I failure of the single contoured cantilever CFRP-reinforced concrete beam. *J. of Struct.*, 2013:1–8, 2013.

[75] Y. T. Obaidat, S. Heyden, and O. Dahlblom. The effect of CFRP and CFRP/concrete interface models when modelling retrofitted RC beams with FEM. *Comp. Struct.*, 92: 1391–1398, 2010.

[76] C. Oskay. Two-level multiscale enrichment methodology for modeling of heterogeneous plates. *Int. J. Numer. Meth. Engng.*, 80:1143–1170, 2009.

[77] C. Oskay and J. Fish. Eigendeformation-based reduced order homogenization for failure analysis of heterogeneous materials. *Comput. Meth. Appl. Mech. Engrg.*, 196:1216–1243, 2007.

[78] C. Ostertag and CK. Yi. Crack-fiber interaction and crack growth resistance behavior in microfiber reinforced mortar specimens. *Mat. and Structures.*, 40:679–691, 2007.

[79] J. Oswald, R. Gracie, R. Khare, and T. Belytschko. An extended finite element method for dislocations in complex geometries: thin films and nanotubes. *Comput. Meth. Appl. Mech. Engng.*, 198:1872–7886, 2009.

[80] J. Pan and C. K. Y. Leung. Debonding along the FRP - concrete interface under combined pulling/peeling effects. *Engng. Fract. Mech.*, 74:132–150, 2007.

[81] N. Pan. The elastic constants of randomly oriented fiber compsotes: A new approach to prediction. *Sci. and Engrg. of Compos. Mater.*, 5:63–72, 1996.

[82] K Park, J. Pereira, C. A. Duarte, and G. Paulino. Integration of singular enrichment functions in the generalized/extended finite element method for three-dimensional problems. *Int. J. Numer. Meth. Engng.*, 78:1220–1257, 2009.

[83] P. Pierre, R. Pleau, and M. Pigeon. Mechanical properties of steel microfiber reinforced cement pastes and motars. *J. Mat. Civil Engng.*, 11:317–324, 1999.

[84] M. Pigeon, R. PleR. Pleau. Azzabi, and N. Banthia. Durability of microfier-reinfroced motars. *Cement and Concrete Research*, 26:601–609, 1996.

[85] G. Pijaudier-Cabot and Z. P. Bazant. Nonlocal damage theory. *J. of Engng. Mech.*, 113:1512–1533, 1987.

[86] M. Pike and C. Oskay. Modeling random short nanofiber- and microfiber-reinforced composites using the extended finite-element method. *J. Nanomech. Micromech.*, 5: 1–11, 2015.

[87] M. Pike and C. Oskay. XFEM modeling of short microfiber reinforced composites with cohesive interfaces. *Finite Elements in Analysis and Design*, 106:16–31, 2015.

[88] M. Pike, M. Hickman, and C. Oskay. Interactions between multiple enrichments in extended finite element analysis of short fiber reinforced composites. *Int. J. Mult. Comput. Engng.*, 2015.

[89] P. Ponte-Castaneda and J.R. Willis. The effect of spatial distribution on the effective behavior of composite materials and cracked media. *J. Mech. Phys. Solids*, 43:1919–1951, 1995.

[90] M. di Prisco and J. Mazars. "Crush-crack": a non -local damage model for concrete. *Mech. of Cohesive-Frictional Mater.*, 1:312–347, 1996.

[91] T. Rabczuk, J. Akkermann, and J. Eibl. A numerical model for reinforced concrete structures. *Int. J. Solids and Struct.*, 42:1327–1354, 2005.

[92] F.K.F. Radtke, A. Simone, and L.J. Sluys. A partition of unity finite element method for obtaining elastic properties of continua with embedded thin fibres. *Int. J. Numer. Meth. Engng.*, 84:708–732, 2010.

[93] F.K.F. Radtke, A. Simone, and L.J. Sluys. A partition of unity finite element method for simulating non-linear debonding and matrix failure in thin fibre composites. *Int. J. Numer. Meth. Engng.*, 86:453–476, 2011.

[94] R. Ravichandran, J.R. Venugopal, S. Sundarrajan, S. Mukherjee, R. Sridhar, and S. Ramakrishna. Minimally invasive injectable short nanofibers of poly(glycerol sebacate) for cardiac tissue engineering. *Nanotechnology*, 23(385102):1–14, 2012.

[95] F. Reza, J. A. Yamamuro, and G. B. Batson. Electrical resistance change in compact tension specimens of carbon fiber cement composites. *Cement and Concrete Compos.*, 26:873–881, 2004.

[96] C. Richardson, J. Hegemann, E. Sifakis, J. Hellrung, and J. Teran. An XFEM method for modeling geometrically elaborate crack propagation in brittle materials. *Int. J. Numer. Meth. Engng.*, 88:1042–1065, 2011.

[97] W. B. Russel. On the effective moduli of composite materials: effect of fiber length and geometry at dilute concentrations. *Z. Angew. Math. Phys.*, 24, 1973.

[98] F. Sanchez and C. Ince. Microstructure and macroscopic properties of hybrid carbon nanofiber/silica fume cement composites. *Compos. Sci. Technol.*, 69:1310–1318, 2009.

[99] J.C. Simo, J. Oliver, and F. Armero. An analysis of strong discontinuities induced by strain-softening in rate-independent inelastic solids. *Comp. Mech.*, 12:277–296, 1993.

[100] S. Soghrati and P. H. Geubelle. A 3D interface-enriched generalized finite element method for weakly discontinuous problems with complex internal geometries. *Comput. Meth. Appl. Mech. Engng.*, 217-220:46–57, 2012.

[101] N. Sukumar and J-H. Prevost. Modeling quasi-static crack growth with the extended finite element method part 1: Computer implementation. *Int. J. Solids and Struct.*, 40:7513–7537, 2003.

[102] N. Sukumar, N. Moes, B. Moran, and T. Belytschko. Extended finite element method for three-dimensional crack modelling. *Int. J. Numer. Meth. Engng.*, 48:1549–1570, 2000.

[103] N. Sukumar, D.L. Chopp, and B. Moran. Extended finite element method and fast marching method for three-dimensional fatigue crack propagation. *Engng. Fract. Mech.*, 70:29–48, 2003.

[104] G. P. Tandon and G. J. Weng. Average stress in the matrix and effective moduli of randomly oriented composites. *Compos. Sci. Technol.*, 27:111–132, 1986.

[105] G. Thiagarajan, K. Hsia, and Y. Huang. Finite element implementation of virtual internal bond model for simulating crack behavior. *Engng. Fract. Mech.*, 71:401–432, 2004.

[106] J. Unger, S. Eckardt, and C. Konke. Modelling of cohesive crack growth in concrete structures with the extended finite element method. *Comput. Meth. Appl. Mech. Engng.*, 196:4087–4100, 2007.

[107] G. Ventura, E. Budyn, and T. Belytschko. Vector level sets for description of propagating cracks in finite elements. *Int. J. Numer. Meth. Engng.*, 58:1571–1592, 2003.

[108] H.W. Wang, H.W. Zhoe, H.W. Ji, and X.C. Zhang. Application of extended finite element method in damage progress simulation of fiber reinforced composites. *Mater. and Design*, 55:191–196, 2014.

[109] J. Wang. Cohesive zone model of intermediate crack-induced debonding of FRP-plated concrete beam. *Int. J. Solids and Struct.*, 43:6630–6648, 2006.

[110] J. Wang. Cohesive zone model of frp-concrete interface debonding under mixed-mode loading. *Int. J. of Solids and Struct.*, 44:6551–6568, 2007.

[111] H. Wendland. Piecewise polynomial, positive definite and compactly supported radial functions of minimal degree. *Advances in Comp. Math.*, 4:389–396, 1995.

[112] J.L. Winds, S. Steffensen, and H.M. Jensen. Comparison of a composite model and an individually fiber and matrix discretized model for kink band formation. *Int. J. Non-Lin. Mech.*, 67:319–325, 2014.

[113] J. Won, B. Hong, T. Choi, S. Lee, and J. Kang. Flexural behaviour of amorphous micro-steel fibre-reinforced cement composites. *Compos. Struct.*, 94:1443–1449, 2012.

[114] X.-P. Xu and A. Needleman. Void nucleation by inclusion debonding in a crystal matrix. *Modelling Simul. Mater. Sci. Engng.*, 1:111–132, 1993.

[115] X.-P. Xu and A. Needleman. Numerical simulations of fast crack growth in brittle solids. *J. Mech. Phys. Solids*, 42:1397–1434, 1994.

[116] H. Yan, C. Oskay, A. Krishnan, and L. R. Xu. Compression-after-impact response of woven fiber-reinforced composites. *Compos. Sci. Technol.*, 70:2128–2136, 2010.

[117] CK. Yi and C. Ostertag. Strengthening and toughening mechanisms in microfiber reinforced cementitious composites. *J. Mat. Sci.*, 36:1513–1522, 2001.

[118] D. Yoo, J. Lee, and Y. Yoon. Effect of fiber content on mechanical and fracture properties of ultra high performance fiber reinforced cementitious composites. *Compos. Struct.*, 106:742–753, 2013.

[119] X. Zhuang, C.E. Augarde, and K.M. Mathisen. Fracture modeling using meshless methods and level sets in 3D: Framework and modeling. *Int. J. Numer. Meth. Engng.*, 92:969–998, 2012.

[120] G. Zi and T. Belytschko. New crack-tip elements for XFEM and applications to cohesive cracks. *Int. J. Numer. Meth. Engng.*, 57:2221–2240, 2003.

[121] G. Zi, J. Song, E. Budyn, S. Lee., and T. Belytschko. A method for growing multiple cracks without remeshing and its application to fatigue crack growth. *Modelling Simul. Mater. Sci. Engng.*, 12:901–915, 2004.